UNIVERSITÉ DE STRASBOURG

ÉCOLE DOCTORALE des Sciences Chimiques

ISIS (UMR 7006)

Laboratoire des Nanostructures

THÈSE présentée par :

Shaojun WANG

soutenue le : **11 Septembre 2015**

pour obtenir le grade de : **Docteur de l'université de Strasbourg**

Discipline/ Spécialité : Chimie Physique

Strong Light-Molecule Coupling: Routes to New Hybrid Materials

THÈSE dirigée par :

Prof. EBBESEN Thomas Professeur, Université de Strasbourg

RAPPORTEURS :

Prof. KÄLL Mikael Professeur, Chalmers University of Technology

Prof. NORRIS David Professeur, ETH

AUTRES MEMBRES DU JURY :

Prof. HAACKE Stefan Professeur, Université de Strasbourg

Shaojun WANG

Strong Light-Molecule Coupling: Routes to New Hybrid Materials

Résumé

Quand l'interaction entre deux oscillateurs physiques est assez fortement, ils peuvent développer deux nouveaux modes normaux et affichent un comportement dispersif anticroisement, ce système est appelé dans le régime de couplage fort. Un couplage fort peut également être réalisé entre une résonance de la matière et un mode optique, ce qui a été observé pour la première fois en physique atomique en 1980, ensuite dans les semi-conducteurs en 1990 et récemment avec des matériaux moléculaires. Le couplage fort en lumière-matière est d'un grand intérêt pour les études fondamentales, et il aussi présente le potentiel technologique parce qu'il peut générer la condensation de Bose-Einstein (BEC) à la température ambiante et l'effet laser de seuil moins entre autres.

Au cours des 15 dernières années, la recherche sur le couplage fort en lumière-matière avec des matières organiques prête de plus en plus attention en raison de la très grande fractionnement de l'énergie générant dans ces systèmes entre les deux états hybrides en lumière-matière qui sont aussi connu comme les états polaritoniques , généralement notés P + et P- . La grande division d'énergie, s'appelle Rabi division, est provoqué par une transition efficace de dipôle moments entre des molécules et aussi par des cavités ou des plasmons en surface de petits volumes en mode de micro-Fabry-Pérot métalliques (FP) qui sont utilisés dans ces études. Rabi-splittings ~ 1

eV représente souvent une fraction importante de l'énergie de transition électronique, dans ce cas, le système est appelé dans le régime de couplage ultra-forte.

Dans ce régime, la physico-chimie des molécules ou des propriétés des matériaux du système couplé peuvent être modifié. En effet, d'effet a déjà été montré sur les voies de relaxation dans le système couplé, les taux de réactions photochimiques, le travail d'extraction et de la conductivité des semi-conducteurs organiques dans l'obscurité, entre autres choses. Une étude récente a pu montrer que l'énergie de l'état non-excité dans une étude thermodynamique peut également être décalée dans le régime de couplage ultra-fort. De plus, le couplage fort ne se limite pas à des transitions électroniques, mais peut aussi être utilisé pour perturber les vibrations de l'état non-excité de molécules dans la région infrarouge. Tous ces résultats montrent que le couplage fort en lumière-molécule a beaucoup de potentiel pour le matériel et la science moléculaire et mérite donc une étude plus approfondie. Le sujet de ma thèse est dans ce contexte.

Dans le chapitre 2, les concepts de base de l'interaction lumière-matière, y compris les couplages faibles et un couplage fort, le fractionnement de l'énergie, et des effets collectifs, seront présentés et discutés. Par la suite, le développement historique de recherche sur le couplage fort en lumière-matière sera examiné. Des exemples sur des expériences en couplage fort de la physique atomique, semi-conducteurs et de la science moléculaire seront présentés. Dans la dernière section, nous allons nous concentrer sur les conséquences et les applications de couplage fort avec des molécules organiques. Dans le chapitre 3 une description théorique plus détaillé qui prédit avec succès les observations expérimentales de systèmes fortement couplés sera fourni, par exemple le comportement de dispersion anti-franchissement. Spectres optique statique du système couplé sera dérivée et simulé dans le cas classique en traitant la susceptibilité macroscopique linéaire. De plus, le vide-Rabi fractionnement, le changement d'état non-excité, et de la nature délocalisée de la fonction d'onde seront démontré quantitativement en dérivant

l'hamiltonien pour le système. Le simple Lorentzienne classique, le quantum de Jaynes-Cummings et aussi le modèle Tavis-Cummings donnent un aperçu de la physique de couplage fort. Basé sur ces fondamentaux, quatre études expérimentales ont été effectuées:

La première partie des expériences dans cette thèse (chapitres 4 et 5) est consacré à l'ingénierie des paramètres de structures optiques pour régler l'efficacité du couplage fort en lumière-matière (Rabi-splitting), qui joue le rôle principal dans les changements fondamentaux de propriétés moléculaires. De plus, plus fractionné du Rabi, la plus grande fraction de molécules est couplée. Nous allons commencer par une étude du couplage fort de porphyrine agrégats J à nanostructures plasmoniques de symétrie différente (chapitre 4). Des études montrent que les nanostructures optiques de symétrie ultérieure afficher l'interaction la plus forte avec la couche moléculaire, ce qui indique que le mode de plasmon de surface dégénérescence joue un rôle important dans l'efficacité de couplage. Avec la force de couplage élevée, un nouveau, faiblement dispersif mode a été observé qui a été récemment prédit théoriquement qu'il a été provoqué par un transfert d'énergie à long terme entre les molécules induites par plasmons de surface. Ces résultats mènent à de nouveaux moyens permettant d'optimiser le couplage fort plasmoniques sur des substrats, en jouant non seulement sur la densité moléculaire, mais aussi sur le mode de densité photonique.

Dans une étude ultérieure (chapitre 5), le Rabi-fractionnement a été réglée précisément par la variation de la position spatiale d'une mince couche de colorant cyanine J-agrégats FP micro-cavités. Les propriétés photophysiques de deux échantillons de la cavité demi-pension et pleine longueur d'onde ont été testés. L'étendue de la division Rabi observé reproduit la répartition spatiale de l'amplitude du mode de la cavité dans chaque cas. Le placement maximum de la couche moléculaire dans le champ de la cavité augmente l'énergie d'interaction (Rabi de fendage) par ~ 60% par rapport à celle observée dans le cas que les agrégats sont simplement répartis

uniformément à travers la cavité, et le système est mis dans le régime de couplage ultra-fort. D'autres aspects de couplage fort en lumière molécule dans ces systèmes, par exemple, le rendement quantique de la fluorescence de polaritons émission, et ses implications pour le mécanisme de désintégration de l'état couplé, ont été étudiés. Les résultats indiquent que la désintégration de polaritons est dominée par des processus non radiatifs contrairement à ce qu'on pourrait attendre de la petite masse effective des polaritons. En d'autres termes, malgré le fait que les quasi-polaritons sont des bosons, les systèmes moléculaires fortement couplés sont dans la plupart des cas sans intérêt pour la fabrication des diodes électroluminescentes sauf que le système est conçu soigneusement, par example, dans la démonstration de l'effet laser polariton.

Dans le chapitre 6, les propriétés et la dynamique du système fortement couplé impliquant trois molécules avec très différentes propriétés en photo-physique ont été systématiquement étudiées. En particulier, nous analysons leurs propriétés de photoluminescence et montrons que les spectres d'excitation sont très différents de l'absorption statique des systèmes couplés. Le pic d'absorption en raison d'P- statique ne conduit pas facilement à la production de l'émission P- ou encore l'une absorption transitoire observable. L'excitation directe de P est donc un moyen très inefficace de alimenter l'état, malgré le photon 50:50 - excitation moléculaire mélangeant à la fois P + et P- dans nos expériences. De plus, les rendements quantiques d'émission et la durée de vie à l'état excité dans le régime de ps, sont auto-cohérent. La durée de vie de la population de P est beaucoup plus longue que la durée de vie du photon dans le mode de la cavité, ce qui est contraire à l'intuition dans l'image conventionnelle où les propriétés dynamiques des états couplés sont directement déterminées à partir de celles de ceux nues, par conséquent, il reste encore beaucoup à être compris.

Bien que le couplage fort en lumière-molécule soit généralement associé au fractionnement des états excités, le niveau d'énergie de l'état fondamental doit également être poussé vers le bas

en raison de la perturbation de second ordre. Cette prédiction a été confirmée dans une étude thermodynamique de couplage fort. Inspiré par ce résultat, nous avons examiné si une transition de phase thermique d'un matériau peut être modifiée par couplage fort. Dans le chapitre 7, la transition de phase du sel de type perovskite [$Pb(II)I_4^{2-}(C_{12}H_{25}NH_3^+)_2$] est analysé sous le couplage fort avec le mode de cavité, et montrent que l'hystérésis et de la dynamique sont modifiées de manière significative. Les modifications sont attribuées à l'abaissement des états fondamentaux des deux phases par l'interaction avec le terrain. En conséquence, la barrière de transition est augmentée et la boucle d'hystérésis est agrandie, ce qui démontre le potentiel de commande de la environnement électromagnétique (EM) d'un matériau, par exemple, d'un composé à transition de spin.

L'ensemble de la thèse a principalement travaillé sur l'optimisation de la force de couplage fort, comprendre les conséquences fondamentales, ainsi que l'application de la modification des propriétés moléculaires. Les principales conclusions sont donnés dans le contexte et essayer de répondre aux questions soulevées dans le chapitre 2.

Dans le chapitre 4, nous avons utilisé une combinaison de LBL et techniques de dépôt élastomères pour adsorber un agrégat J en couche mince directement à la surface des tableaux plasmoniques de maximiser le couplage fort. Il a été montré que la lumière hybride / indique matière avec une plus grande séparation Rabi pourrait être réalisé lors de l'utilisation de nanostructures plasmoniques de symétrie plus élevée, ce qui indique que le mode SP dégénérescence est important pour un couplage efficace. Ces résultats mettent en évidence de nouveaux moyens permettant d'optimiser le couplage fort plasmoniques sur des substrats, en jouant non seulement sur la densité moléculaire, mais également de la densité de mode photonique, par exemple, plaçant la question à la "hot-spot" de structures plasmoniques comme indiqué dans les références.[53, 110] Dans la dernière partie de ce chapitre nous avons étudié le

couplage fort d'un plasmoniques tableaux de fossette avec les deux bandes de transition d'un colorant cyanine par la réflexion et la spectroscopie d'émission. Les deux bandes d'émission observables à la température ambiante sont liés aux groupes moléculaires et P- polaritons non couplés. L'anti-franchissement dans la dispersion des modes polaritoniques était clair à la fois dans la réflexion et l'émission.

Dans le chapitre 5, l'efficacité de la lumière molécule couplage fort a été réglée précisément par la variation de la position spatiale d'une mince couche de colorant cyanine J-agrégats FP micro-cavités. Le vide-Rabi fractionnement suit la forme de la distribution champ d'amplitude dans les cavités. Il indique que la force de l'interaction de couplage varie de façon linéaire avec l'amplitude du champ de vide défini par la cavité, comme prévu à partir de la théorie de Jaynes-Cummings. La durée de vie mesurée de la plus faible polaritoniques P- d'état (aussi longtemps que ps) et les rendements émission quantiques sont cohérentes entre elles. L'observation de P- durée de vie supérieure de ses Etats constituants est en dehors de la compréhension conventionnelle de la durée de vie de polaritons. En outre, le faible rendement quantique mesurée ($\sim 10^{-2}$) montre que la décroissance de polaritons est dominé par des procédés non radiatifs contrairement à ce qu'on pourrait attendre de la petite masse effective des polaritons.

Dans le chapitre 6, nous avons montré, à travers des expériences, certaines des questions ouvertes liées à la lumière-matière couplage fort impliquant matériaux moléculaires. Il est clair que les files d'largeurs des spectres d'absorption statique associés à P + et P- représentent la durée de vie du système cohérent fortement couplé. Toutefois, dans le cas de fractionnement du Rabi beaucoup plus grande que kBT, la durée de vie de la population de P est dominée par la dissipation des états excités moléculaires autres que celui du mode de la cavité. En outre, l'excitation directe de P est efficace faible, ce qui soulève la question de savoir si les règles des Etats polaritoniques de sélection de transition pourraient être différents de molécules nues.

Nettement plus d'expériences et la théorie qui peut gérer ces matériaux complexes et les particularités des structures moléculaires individuels doivent être développés pour élucider ces systèmes à forte interaction. alors seulement que le plein potentiel de l'aide d'un environnement électromagnétique confiné à contrôler les matières et moléculaire propriétés être réalisés.

Dans le chapitre 7, la transition de phase d'une perovskite a été étudiée pendant sa transition d'absorption a été fortement couplé au domaine de la micro-cavité un vide. L'hystérésis et la dynamique de la transition de phase ont été modifiées de façon significative en raison de l'abaissement des états fondamentaux des deux phases par l'interaction de la cavité. En conséquence, la barrière de transition a été augmentée et la boucle d'hystérésis est agrandie, ce qui démontre la possibilité d'utiliser l'environnement électromagnétique d'un matériau à contrôler ses propriétés. Ces résultats enrichissent le diagramme d'énergie d'un système fortement couplé.

Plus généralement, ces résultats fournissent une compréhension plus profonde des états lumière-molécule hybrides et illustrent les conséquences de la modification des propriétés moléculaires et matérielles par couplage fort.

Résumé en anglais

When two physical oscillators couple so strongly that they develop two new normal modes and display an anticrossing dispersive behavior, the system is said to be in the strong coupling regime. Strong coupling can also be achieved between a matter resonance and an optical mode and this was observed first in atomic physics in 1980s, subsequently in semiconductors in 1990s and recently with molecular materials. This light-matter strong coupling is of much interest from a fundamental point of view but it also has technological potential since it can lead to room temperature Bose-Einstein condensation (BEC) and threshold-less lasing among other things.

Over the past 15 years, light-matter strong coupling involving organic materials has been of increasing interest due to the very large energy splitting such systems exhibit between the two hybrid light-matter states, also known as the polaritonic states typically denoted P+ and P-. The large energy splitting, so-called Rabi splitting, is the result of the high transition dipole moments of the molecules and the small mode volumes of micro-metallic Fabry-Pérot (FP) cavities or surface plasmons used in these studies. Rabi-splittings ~1 eV have been observed, often representing a significant fraction of the electronic transition energy in which case the system is said to be in the ultra-strong coupling regime. In this regime the physical chemistry of molecules or the properties of materials of the coupled system should be modified. Indeed, it has already been shown to affect the relaxation pathways in the coupled system, the rates of photochemical reactions, the work-function and conductivity of organic-semiconductors in the dark, among other things. A recent thermodynamic study demonstrated that the ground state energy can also be shifted in the ultra-strong coupling regime. Moreover, the strong coupling is not limited to electronic transitions, but also can be used to perturb the ground-state vibrations of molecules in the infrared region. All these results suggest that light-molecule strong coupling has much

potential for material and molecular science and therefore merits further study. The subject of my thesis is placed in this context.

In Chapter 2, the basic concepts of light-matter interaction, including weak and strong coupling, energy splitting, and collective effects, will be introduced and discussed. Subsequently, the historical development of light-matter strong coupling research will be reviewed. Examples of strong coupling experiments from atomic physics, semiconductors and molecular science will be presented. In the last section, we will focus on the fundamental consequences and applications of strong coupling with organic molecules. In Chapter 3 a more detailed theoretical description will be provided which successfully predicts experimental observations of strongly coupled systems, for instance the anti-crossing dispersive behavior. Static optical spectra of the coupled system will be derived and simulated in the classical case by treating the linear macroscopic susceptibility. Furthermore, vacuum Rabi-splitting, the ground state shift, and the delocalized nature of the wavefunction will be quantitatively demonstrated by deriving the Hamiltonian for the system. Both the simple classical Lorentzian, the quantum Jaynes-Cummings and Tavis-Cummings model give insights into the physics of strong coupling. Based on these fundamentals, four experimental studies have been carried out:

The first part of the experiments in this thesis (Chapters 4 and 5) is devoted to engineering the parameters of optical structures to tune the efficiency of light-matter strong coupling (Rabi-splitting), which plays the main role in the fundamental changes of molecular properties. In addition, the stronger the Rabi-splitting the larger is the fraction of coupled molecules. We will start with an investigation of the strong coupling of porphyrin J-aggregates to plasmonic nanostructures of different symmetry (Chapter 4). Optical studies show that nanostructures of higher symmetry display the strongest interaction with the molecular layer, suggesting that

surface plasmon mode degeneracy plays an important role in the coupling efficiency. At high coupling strengths a new, weakly dispersive mode was observed which has recently been predicted theoretically to be due to long-range energy transfer between molecules mediated by surface plasmons. These findings point to new ways for optimizing strong coupling on plasmonic substrates, not only playing on molecular density, but also on photonic mode density.

In a subsequent study (Chapter 5), the Rabi-splitting was tuned by precisely varying the spatial position of a thin layer of cyanine dye J-aggregates in FP micro-cavities. The photophysical properties of both half- and full-wavelength cavity samples were tested. The extent of the observed Rabi splitting reproduces the spatial distribution of the cavity mode amplitude in each case. Placing the molecular layer at the cavity field maximum increases the interaction energy (Rabi splitting) by ~ 60% over that observed if the aggregates are simply spread evenly through the cavity, placing the system in the ultra-strong coupling regime. Further aspects of light-molecule strong coupling in these systems, such as the fluorescence quantum yield of polariton emission, and its implications for the decay mechanism of the coupled state, were investigated. The results indicate that the polariton decay is dominated by non-radiative processes in contrast to what might be expected from the small effective mass of the polaritons. In other words, despite the fact that polaritons are quasi-bosons, strongly coupled molecular systems are in most cases uninteresting for making light-emitting devices unless the system is carefully designed such as in the demonstration of polariton lasing.

In Chapter 6 the properties and dynamics of the strongly coupled system involving three molecules with very different photo-physical properties were systematically studied. In particular we analyze their photoluminescence properties and show that the excitation spectra are very different from the static absorption of the coupled systems. The static absorption peak due to P- does not readily lead to the generation of P- emission or even to any observable transient

absorption. The direct excitation of P- is thus a very inefficient way of populating the state, despite the 50:50 photon - molecular excitation mixing for both P+ and P- in our experiments. Furthermore, the emission quantum yields and excited state lifetimes in the ps regime, are self-consistent. The population lifetime of P- is much longer than the lifetime of the photon in the cavity mode, which is counter-intuitive in the conventional picture where the dynamic properties of the coupled states are directly determined from those of the bare ones, therefore much remains to be understood.

Although light-molecule strong coupling is usually associated with splitting of excited states, the ground state energy level should also be pushed down due to second order perturbation. This prediction was confirmed in a thermodynamical study of strong coupling. Inspired by this result, we investigated whether a thermal phase transition of a material could be modified by strong coupling. In Chapter 7, the phase transition of the perovskite type salt $[Pb(II)I_4^{2-}(C_{12}H_{25}NH_3^+)_2]$ is analyzed under strongly coupling with a cavity mode, and show that its hysteresis and dynamics are modified significantly. The modifications are attributed to the lowering of the ground states of the two phases by the interaction with the field. As a consequence, the transition barrier is increased and the hysteresis loop is enlarged, demonstrating the potential of controlling the electromagnetic (EM) environment of a material, e.g. of a spin transition compound.

The whole thesis mainly worked on the optimization of strong coupling strength, understanding fundamental consequences, and application to modifying molecular properties. The main conclusions are given in the context and try to answer the questions raised in Chapter 2.

In Chapter 4 we used a combination of LBL and elastomeric deposition techniques to adsorb a J-aggregate in thin layer directly at the surface of plasmonic arrays to maximize strong coupling. It was shown that hybrid light/matter states with larger Rabi splitting could be achieved

when using plasmonic nanostructures of higher symmetry, indicating that SP mode degeneracy is important for efficient coupling. These findings point to new ways for optimizing strong coupling on plasmonic substrates, not only playing on molecular density, but also on photonic mode density, e.g. placing the matter at the "hot-spot" of plasmonic structures as shown in the references.[53, 110] In the last section of this chapter we investigated the strong coupling of a plasmonic dimple arrays with the two transition bands of a cyanine dye by reflection and emission spectroscopy. The two observable emission bands at room temperature are related to the uncoupled molecular and P- polariton bands. The anti-crossing in the dispersion of the polaritonic modes was clear both in reflection and emission.

In Chapter 5, the efficiency of light-molecule strong coupling was tuned by precisely varying the spatial position of a thin layer of cyanine dye J-aggregates in FP micro-cavities. The vacuum Rabi-splitting follows the shape of the field amplitude distribution in the cavities. It tells that the strength of the coupling interaction varies linearly with the vacuum field amplitude defined by the cavity, as expected from the Jaynes-Cummings theory. The measured lifetime of the lowest polaritonic state P- (as long as ps) and the emission quantum yields are mutually consistent. The observation of P- lifetime longer than its constituent states is outside conventional understanding of polariton lifetimes. Moreover, the measured low quantum yield (~ 10-2) demonstrates that the polariton decay is dominated by non-radiative processes in contrast to what might be expected from the small effective mass of the polaritons.

In Chapter 6, we showed, through experiments, some of the open questions related to light–matter strong coupling involving molecular materials. It is clear that the line-widths of static absorption spectra associated with P+ and P- represent the coherent lifetime of the strongly coupled system. However in the case of Rabi-splitting much larger than kBT, the population lifetime of P- is dominated by the dissipation of molecular excited states other than that of cavity

mode. Moreover, the direct excitation of P- is low efficient, which raises the question whether the transition selection rules of polaritonic states could be different from the bare molecules. Clearly more experiments and theory that can handle such complex materials and the particularities associated with individual molecular structures need to be developed to elucidate these strongly interacting systems.[164] Only then will the full potential of using a confined electromagnetic environment to control material and molecular properties be realized.

In Chapter 7, the phase transition of a perovskite was studied while its absorption transition was strongly coupled to the vacuum field of a micro-cavity. The hysteresis and dynamics of the phase transition were significantly modified due to the lowering of the ground states of the two phases by the cavity interaction. As a consequence, the transition barrier was increased and the hysteresis loop is enlarged, demonstrating the potential of using the electromagnetic environment of a material to control its properties. These findings enrich the energy diagram of strongly coupled system.

More generally, these findings provide a deeper understanding of hybrid light-molecule states and illustrate the implications for the modification of molecular and material properties by strong coupling.

Acknowledgements

First of all I would like to thank my supervisor Prof. Thomas W. Ebbesen for giving me the opportunity to join the Laboratory of Nanosturctures and to enjoy the outstanding resources at ISIS and on the campus of university. I am very grateful for his guidance, support and advice that helped me growing on as a scientific and a personal level.

I would also like to thank Dr. James A. Huchison. He was always available for discussion and sharing ideas, even when he was working in Australia. His hard work and enthusiasm for science always encouraged me for going ahead. I also want to thank Dr. Cyriaque Genet. I am very grateful for his teaching of physics and exciting discussions during the lab meetings.

I want to express my gratitude to Prof. Mikael Käll, Prof. David Norris and Prof. Stefan Haacke for accepting to be on my thesis jury, and for the interest they show in my work.

For offering me the organic materials for the studies in this thesis, I would also like to thank Prof. Jean-Marie Lehn, Prof. Hosseini Mir Wais, Dr. Abdelaziz Jouaiti, and Dr. Guillaume Rogez. I also want to thank Dr. Matteo Mauro and Jacek Arabski for their help with deposition techniques.

I am moreover indebted to Dr. Eloise Devaux, who always showed her patience to solve the equipment problems and share her nanofabrication knowledge. I am also very grateful for the help from Marie-Claude Jouaiti. She was always a step ahead of any administrative issues.

I want to extend my gratitude to all members of the nanostructures laboratory and other members of the ISIS building. Especially I would like to thank Thibault Chervy for his help to handle many optical issues and always open the door for exchanging ideas. I

would also like to thank my office mates Juemin Yi, Gabriel Schnoering and Hadi Bahsoun, as well as Jino Geroge, Atef Shalabney, Chunliang Wang, Xiaolan Zhong, Anoop Thomas, Hidefumi Hiura, Yuri Gorodetski, Tal Schwartz, Emmanuel Lombard, Benedikt Stein, Antoine Canaguier-Durand, Aurelien Cuche, Yantao Pang and Arkadiusz Mika. Moreover, I would also like to thank Mirella Gemayel, Nina Matoussevitch and Chien-Wei Hsu who always showed their kindness and offered me much help.

I would also like to thank all my friends on the campus. Especially, I would like to thank Dr. Songlin Li and Dr. Lei Zhang for sharing scientific experiences across borders and for enjoying sports together. My friend off-campus, Dr. Jialiang Xu, I want to thank him for giving me much advice for future.

At last, I would like to thank my family for their unconditional support and particularly I want to thank Chaojie for her patience and her love.

Contents

Abbreviations and symbols

BDAB	5-(4-(dibutylamino) benzylidene)-1,3-dimethylpyrimidine-2,4,6(1H,3H,5H)-trione
BEC	Bose-Einstein condensation
BZ	Brillouin zone
DBR	distributed Bragg reflector
EM	electromagnetic
FIB	focused ion beam
FP	Fabry-Pérot
fs	femtosecond
FWHM	full width at half maximum
H_2TPPS^{4-}	4,4′,4″,4‴-(porphine-5,10,15,20-tetrayl)tetrakis(benzenesulfonic acid) tetrasodium salt hydrate
IR	infrared
IVR	internal vibrational relaxation
LBL	layer-by-layer
N.A.	numerical aperture
OLED	organic light-emitting diode
P-	lower polaritonic state
P+	upper polaritonic state
PDDA	polydiallyldimethylammonium
PDMS	polydimethylsiloxane

PMMA	poly(methyl methacrylate)
ps	picoseconds
PVA	poly(vinyl) alcohol
Q factor	quality factor
RWA	rotating wave approximation
SPPs	surface plasmon polaritons
TDBC	5,6-dichloro-2-[[5,6-dichloro-1-ethyl-3-(4-sulphobutyl)benzimidazol-2- ylidene]propenyl]-1-ethyl-3-(4-sulphobutyl)
TM	transverse magnetic
WM	Wannier-Mott

1 Preface

When two physical oscillators couple so strongly that they develop two new normal modes and display an anticrossing dispersive behavior, the system is said to be in the strong coupling regime. Strong coupling can also be achieved between a matter resonance and an optical mode and this was observed first in atomic physics in 1980s, subsequently in semiconductors in 1990s and recently with molecular materials. This light-matter strong coupling is of much interest from a fundamental point of view but it also has technological potential since it can lead to room temperature Bose-Einstein condensation (BEC) and threshold-less lasing among other things.

Over the past 15 years, light-matter strong coupling involving organic materials has been of increasing interest due to the very large energy splitting such systems exhibit between the two hybrid light-matter states, also known as the polaritonic states typically denoted P+ and P-. The large energy splitting, so-called Rabi splitting, is the result of the high transition dipole moments of the molecules and the small mode volumes of micro-metallic Fabry-Pérot (FP) cavities or surface plasmons used in these studies. Rabi-splittings ~1 eV have been observed, often representing a significant fraction of the electronic transition energy in which case the system is said to be in the ultra-strong coupling regime. In this regime the physical chemistry of molecules or the properties of materials of the coupled system should be modified. Indeed, it has already been shown to affect the relaxation pathways in the coupled system, the rates of photochemical reactions,

the work-function and conductivity of organic-semiconductors in the dark, among other things. A recent thermodynamic study demonstrated that the ground state energy can also be shifted in the ultra-strong coupling regime. Moreover, the strong coupling is not limited to electronic transitions, but also can be used to perturb the ground-state vibrations of molecules in the infrared region. All these results suggest that light-molecule strong coupling has much potential for material and molecular science and therefore merits further study. The subject of my thesis is placed in this context.

In **Chapter 2**, the basic concepts of light-matter interaction, including weak and strong coupling, energy splitting, and collective effects, will be introduced and discussed. Subsequently, the historical development of light-matter strong coupling research will be reviewed. Examples of strong coupling experiments from atomic physics, semiconductors and molecular science will be presented. In the last section, we will focus on the fundamental consequences and applications of strong coupling with organic molecules. In **Chapter 3** a more detailed theoretical description will be provided which successfully predicts experimental observations of strongly coupled systems, for instance the anti-crossing dispersive behavior. Static optical spectra of the coupled system will be derived and simulated in the classical case by treating the linear macroscopic susceptibility. Furthermore, vacuum Rabi-splitting, the ground state shift, and the delocalized nature of the wavefunction will be quantitatively demonstrated by deriving the Hamiltonian for the system. Both the simple classical Lorentzian, the quantum Jaynes-Cummings and Tavis-Cummings model give insights into the physics of strong coupling. Based on these fundamentals, four experimental studies have been carried out:

The first part of the experiments in this thesis (**Chapters 4 and 5**) is devoted to engineering the parameters of optical structures to tune the efficiency of light-matter strong coupling (Rabi-splitting), which plays the main role in the fundamental changes of molecular properties. In addition, the stronger the Rabi-splitting the larger is the fraction of coupled molecules. We will start with an investigation of the strong coupling of porphyrin J-aggregates to plasmonic nanostructures of different symmetry (**Chapter 4**). Optical studies show that nanostructures of higher symmetry display the strongest interaction with the molecular layer, suggesting that surface plasmon mode degeneracy plays an important role in the coupling efficiency. At high coupling strengths a new,

weakly dispersive mode was observed which has recently been predicted theoretically to be due to long-range energy transfer between molecules mediated by surface plasmons. These findings point to new ways for optimizing strong coupling on plasmonic substrates, not only playing on molecular density, but also on photonic mode density.

In a subsequent study (**Chapter 5**), the Rabi-splitting was tuned by precisely varying the spatial position of a thin layer of cyanine dye J-aggregates in FP micro-cavities. The photophysical properties of both half- and full-wavelength cavity samples were tested. The extent of the observed Rabi splitting reproduces the spatial distribution of the cavity mode amplitude in each case. Placing the molecular layer at the cavity field maximum increases the interaction energy (Rabi splitting) by ~ 60% over that observed if the aggregates are simply spread evenly through the cavity, placing the system in the ultra-strong coupling regime. Further aspects of light-molecule strong coupling in these systems, such as the fluorescence quantum yield of polariton emission, and its implications for the decay mechanism of the coupled state, were investigated. The results indicate that the polariton decay is dominated by non-radiative processes in contrast to what might be expected from the small effective mass of the polaritons. In other words, despite the fact that polaritons are quasi-bosons, strongly coupled molecular systems are in most cases uninteresting for making light-emitting devices unless the system is carefully designed such as in the demonstration of polariton lasing.

In **Chapter 6** the properties and dynamics of the strongly coupled system involving three molecules with very different photo-physical properties were systematically studied. In particular we analyze their photoluminescence properties and show that the excitation spectra are very different from the static absorption of the coupled systems. The static absorption peak due to P- does not readily lead to the generation of P- emission or even to any observable transient absorption. The direct excitation of P- is thus a very inefficient way of populating the state, despite the 50:50 photon - molecular excitation mixing for both P+ and P- in our experiments. Furthermore, the emission quantum yields and excited state lifetimes in the ps regime, are self-consistent. The population lifetime of P- is much longer than the lifetime of the photon in the cavity mode, which is counter-intuitive in the conventional picture where the dynamic properties of the

coupled states are directly determined from those of the bare ones, therefore much remains to be understood.

Although light-molecule strong coupling is usually associated with splitting of excited states, the ground state energy level should also be pushed down due to second order perturbation. This prediction was confirmed in a thermodynamical study of strong coupling. Inspired by this result, we investigated whether a thermal phase transition of a material could be modified by strong coupling. In **Chapter 7**, the phase transition of the perovskite type salt $[Pb(II)I_4^{2-}(C_{12}H_{25}NH_3^+)_2]$ is analyzed under strongly coupling with a cavity mode, and show that its hysteresis and dynamics are modified significantly. The modifications are attributed to the lowering of the ground states of the two phases by the interaction with the field. As a consequence, the transition barrier is increased and the hysteresis loop is enlarged, demonstrating the potential of controlling the electromagnetic (EM) environment of a material, e.g. of a spin transition compound.

Finally, the overall results will be summarized in **Chapter 8** with conclusions, and potential issues and developments for further study of strong light-molecules will be given.

Part I.

Fundamentals

2 General introduction

In this first chapter, the basic concepts of light-matter interaction will be introduced. Two regimes of interaction, weak and strong coupling, will be described together with characteristic features of strongly coupled systems, such as energy splitting and collective behaviour. Subsequently, the historical development of light-matter strong coupling research will be reviewed. Examples of strong coupling experiments from atomic physics, inorganic semiconductors and organic materials will be presented. In the last section, we will focus on the fundamental issues and the potential applications of strong coupling with organic materials.

2.1 Basics of light-matter interaction

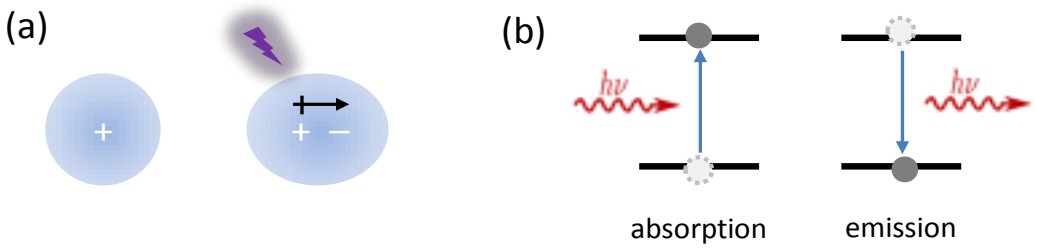

Figure 2.1: Schematic representation of light-matter interaction: (a) the oscillating electric field interacts with electric charges, i.e. the positive nucleus and negative electrons that comprise an atom or molecule, and causes the transitions such as absorption and emission (b).

The interaction between light and matter determines the appearance of the natural world around us. Visible light emitted by the hot plasma on the sun propagates through space and as well some of it scatters off the clouds around earth. The light, arriving at the surface of earth, will be detected and absorbed by the cells of our retina, making possible our vision. Questions then may naturally arise in our minds, such as how does the sun emit light, why does the sky appears blue on sunny days, and why a rainbow occurs on a rainy summer day... With the development of science, we have understood such phenomena and learned that light can behave as both a particle and a wave. The propagation, dispersion and linear scattering of light can be explained by Maxwell's EM wave equations[1, 2], whereas the absorption, emission and non-linear effects can be better understood with quantum notions such as photon and energy levels[3]. In this work, we focus on the coupling between an EM field and a material's transition dipoles, as illustrated in Fig. 2.1, which we will discuss next.

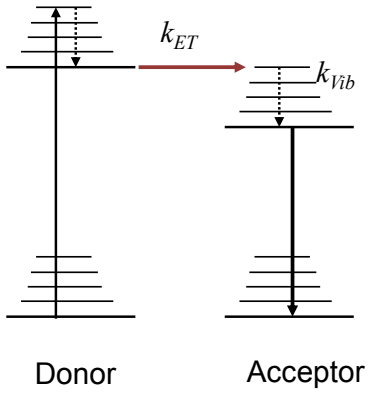

Figure 2.2: Förster energy transfer mechanism between singlet dipole-dipole interactions.

The interactions between physical systems are commonly studied in two different limits known as the weak and the strong coupling regimes. Förster energy transfer[4] (sketched in Fig. 2.2) between donor and acceptor molecules is a good illustration of weak coupling. The energy transfer rate (k_{ET}) from donor to acceptor is smaller than the vibrational relaxation rate (k_{Vib}) in the excited state of the acceptor; hence, the resonance transfer from donor to acceptor is typically an irreversible process. In other words, once the energy is transferred to the acceptor, there is little chance of a back transfer to the donor. However, if the interaction is strong enough so that the energy exchange occurs

faster than the relaxation process then a back transfer to the donor becomes possible; the system is then in the strong coupling limit. In this regime, it is no longer possible to distinguish the donor and the acceptor. Instead, the quantum superposition of the excitation oscillating between the donor and the acceptor define new eigenstates for the whole system collectively and the excitation becomes delocalized over more than one molecule, known as an exciton, as proposed by Davydov[5]. Interestingly, this general mechanism of weak and strong coupling occurring between molecules can be transferred to light-matter interactions.

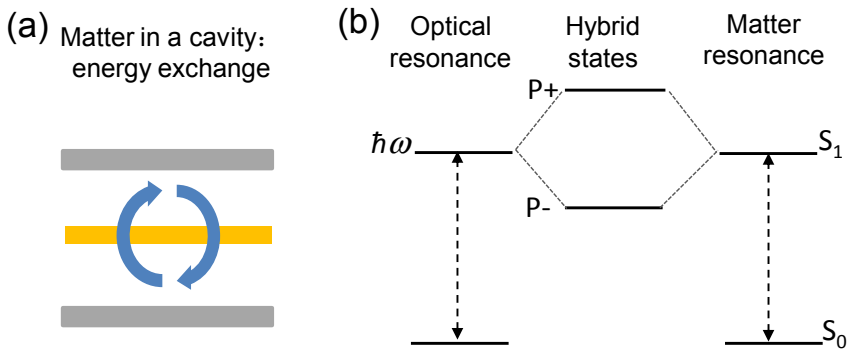

Figure 2.3: (a) Energy exchange between light and matter in the strong coupling regime forms two new hybrid states P+ and P- (b).

We take the process of emission as a paramount example for explaining light-matter coupling. From the quantum electrodynamics perspective, the spontaneous emission of an emitter is due to its excited state coupling to a continuum of the EM field. Confining the EM field to a given mode around a single emitter can lead to either the acceleration or the inhibition of its radiative decay depending the optical mode density at the emission wavelength[6]. The emission wavelength is nevertheless unaltered. This Purcell effect[7] is a weak coupling phenomenon. Once again, if the energy exchange between the emitter and the EM mode is sufficiently fast compared to dissipation then the system can enter into the light-matter strong coupling regime. The dissipation can occur either by radiative decay of the EM mode or relaxation of the excited state. Qualitatively, the back-and-forth energy exchange, known as Rabi oscillations, results in the formation of new energy levels that are different from those of the emitter or of the optical structures,

as illustrated in Fig. 2.3. These hybrid light-matter states are the central topic of this thesis. More specifically, the optical structure, e.g. a FP cavity, and the matter form a composite quantum system with two new polaritonic eigenstates, P+ and P- , which are superpositions of the initial uncoupled states. The energy difference of the two new states, namely the Rabi-splitting, depends on the strength of the coupling. A more theoretical and quantitative description of Rabi-splitting will be given in Chapter 3. Notably it will be shown that even in the absence of light, a residual Rabi splitting, known as vacuum Rabi splitting, exists due to the coupling of transition dipoles with the vacuum field of the cavity.

As we will see theoretically in Chapter 3, our studies involve the strong coupling of N molecules or transition dipoles with a given optical mode. In other words, the N dipoles are collectively coupled together forming a delocalized state over the volume occupied by the mode. Such extended states offer many interesting possibilities for molecular materials that are just beginning to be explored. Furthermore, the Rabi splitting and the Rabi oscillation rate increase as the square root of N. As a consequence ensemble coupling is a way to achieve the strong coupling regime even in the presence of fast dissipation. When the polaritonic states are populated, so-called polaritons are formed. These quasi-bosons can lead to fascinating phenomena such as thresholdless lasing and BEC, the details of which will be mentioned in the subsections below.

2.2 History of light-matter strong coupling research

In 1983, the evidence of strong coupling[8] was obtained in Haroche's group with a collection of Rydberg atoms in a resonant millimeter wave cavity. The atom-field interaction overwhelming dissipative processes was met in this experiment when the number of atoms (N) was large enough, even if the cavity Q factor was moderately high (Q = 3200). The subsequent studies of single Rydberg atom strong coupling was done in a superconducting cavity.[9] In the optical range, strong coupling was achieved first with many atoms[10] and finally with a single atom in 1992[11]. Not only do strong coupling

merge the appealing properties of photon and atoms, they also enrich the quantum physics[12] and offer the prospect of exploiting modern techniques to develop quantum optical systems.[13]

In the beginning of 1990s, Weisbuch et al. first[14] demonstrated strong coupling between semiconductor excitons (electron-hole pairs) and a cavity mode in GaAs quantum wells. When populated, the hybrid states gave thus rise to exciton-polaritons. In semiconductor-cavity systems, many dipoles contributed to the strong coupling effect and consequently the effective dipole moment was larger resulting in much bigger Rabi splitting as compared to atom-cavity systems. The Rabi splitting was therefore referred to as many-body Rabi splitting. Subsequent experiments examined photoluminescence properties[15, 16], dynamics[17] and gain generation of polaritons[18]. The studies of inorganic strongly coupled system eventually led to the observation of macroscopic quantum coherent effects such as BEC of cavity polaritons.[19]

Quantum well excitons in inorganic semiconductors are of the Wannier-Mott (WM)-type.[20] These delocalized and diffuse excited states are usually weakly bound (with an energy below 1 k_BT = 26 meV at room temperature) and can have large Bohr radii (> 10 nm). Therefore, WM excitons can generally be ionised at room temperature, and also have a relatively low saturation density above which the exciton picture starts to break down due to non-linear exciton-exciton interactions.[21] Moreover, the low oscillator strength of WM excitons in inorganic semiconductor gives rise to small Rabi-splitting (~ 10 meV)[22] which is difficult to resolve at room temperature because of thermal broadening (~ 26 meV). All these features shape the critical conditions required to observe strong coupling, such as cryogenic temperatures (~ 77 K), and high quality DBR (distributed Bragg reflector) cavities. Nevertheless, there are several reports of strong coupling at room temperature by employing inorganic excitons with high binding energies, such as GaN quantum wells[23, 24], colloidal quantum dots[25], and single atomic layer of MoS_2[26]. In 2004, a single quantum dot deposited in a photonic crystal cavity exhibited the strong coupling effect.[27] It was the first demonstration of strong coupling of a single two-level solid-state system with a photon, providing a significant new avenue for quantum information processing or coherent control.[22]

Compared with those of inorganic semiconductors, organic materials have a number of appealing physical features for strong coupling. Particularly, large transition dipole moments of organic molecules due to more localized Frenkel excitons (comparing with WM excitons), charge transfer excitons, and π–π^* transitions, etc.[28] Also, a large density of molecules can easily be deposited in an optical structure. Hence high effective transition dipole moments of organic materials can compensate for low Q-factor cavities. Rabi-splitting of 70 meV could thus be observed at room temperature by utilizing low Q (~ 10) and surface confined EM modes (surface plasmon polaritons: SPPs) as first reported in the 1982 seminal paper by Pockrand et al.[29] In 1998, two more publications reported organic strong coupling at room temperature with Rabi-splitting ~100 meV. One was presented by Lidzey et al.[30] using porphyrin molecules located in a planar micro-cavity, and another was presented by Fujita et al.[31] using carbon-chain modified perovskite deposited in a distributed feedback micro-cavity. In 2002, it was shown that a cyanine J-aggregates placed within a metallic micro-cavity may lead to a 300 meV Rabi splitting.[32] This splitting was larger than that shown in a micro-cavity confined by DBR mirrors, due to the larger EM field magnitude existing in the smaller mode volume of an all metallic micro-cavity. In 2011, a Rabi splitting of 700 meV was achieved using a photochrome combined with both a metallic FP cavity and plasmonic structure, representing 32 % of the transition energy. In this context, interest has grown significantly in the use of organic materials to study strong coupling.[13, 21, 33-38]

2.3 State-of-the-art of strong light-molecule coupling

Since 1982, a very large number of works on strong light-molecule coupling have focused on J-aggregates[39-60] because they are characterized by high exciton oscillator strengths, small Frank-Condon shifts, and narrow absorption and emission linewidth (40~60 meV). More recently, many other molecules and organic materials have been used in strong coupling studies to explore the fundamental properties of coupled systems[61-66]

and to use their features to investigate physical phenomena[67-69], devices[70, 71], and the consequences for material and molecular science[72-74].

The photophysical properties of coupled systems have been extensively studied to characterize lifetimes, Rabi oscillations and the spatial and temporal coherence, among other things. For instance the real-time observation (on 10 fs scale) of ultrafast Rabi-oscillations in a J-aggregate/metal nanostructure was reported by Lienau's group[55], indicating coherent energy transfer between excitons and SPP fields. In 2012, Bellessa's group[48] showed that strong coupling between a disordered set of J-aggregate emitters and surface plasmons leads to the formation of spatially coherent hybrid states extended over macroscopic distances. Törmä et al.[62] also studied the spatial coherence properties of a system composed of periodic silver nanoparticle arrays covered with a laser dye film. The evolution of spatial coherence of this composite structure from the weak to the strong coupling regime was investigated. A high degree of spatial coherence was demonstrated in the strong coupling regime from the classical interference fringes. To overcome the short coherence times of SPPs (10-100 fs) in the strong coupling studies, collective delocalized surface lattice resonances in metal nanoparticle arrays[75] and Tamm plasmons existing on the boundary between a metal film and DBR mirror[76] have been exploited.

Interestingly, inhomogeneously broadened molecular absorption peaks can lead to two very distinct situations. On the one hand, it can give rise to extremely large Rabi-splittings, ~1 eV.[71] At the same time, depending on the experimental conditions, Rabi splittings smaller than the inhomogeneous envelope can be generated since the line-width does not reflect lifetime of the molecular excited state.[77] For instance Törmä's group demonstrated distinct strong coupling between vibronic transitions of Rhodamine 6G molecules and SPP.[61] In addition they showed that the Rabi-splitting can be controlled by adjusting the interaction time between waveguided SPPs and molecules deposited on top of the waveguide, in analogy to tunable-Q micro-cavities.

Over the years, the lifetimes of the polaritonic states have been studied by several groups.[51, 54, 78-81] The lifetime of the P- was observed much longer than the lifetime of the photon confined by the optical structures. Moreover, the excited P+ and P- relax with totally different lifetimes. Also in recent experiments using resonant excitation, the lifetime of P- has even been shown to be longer than that of the excited state of the bare

molecule.[59, 60] These properties are counter-intuitive in the conventional picture where the dynamic properties of the coupled states are directly determined from those of the bare ones. The long lifetime of the P- and different lifetimes of P+ and P- have been explained by the non-Markovian character of the relaxation of the dressed organic system.[77]

Thanks to the delocalized wavefunctions of the polaritonic states, the strong coupling can provide an alternate efficient path for energy transfer (which will be discussed in the following theory chapter). The characteristic length-scale for this transfer could potentially be enhanced by the spatial extent of the optical mode and thus be considerably longer than in conventional Förster-type process.[37] Recently, Coles et al[82] from Lidzey's group used strong coupling in an optical microcavity to mix two J-aggregates, probed by both photoluminescence emission and fluorescence excitation spectroscopy to show that organic hybrid-polariton states act as an efficient and ultrafast energy-transfer pathway between the two exciton states even though their lifetimes did not change. Following, they used the same model in order to study the modification of the energy transfer pathways by strongly coupling chlorosomes of photosynthetic bacteria and a confined optical cavity mode.[65]

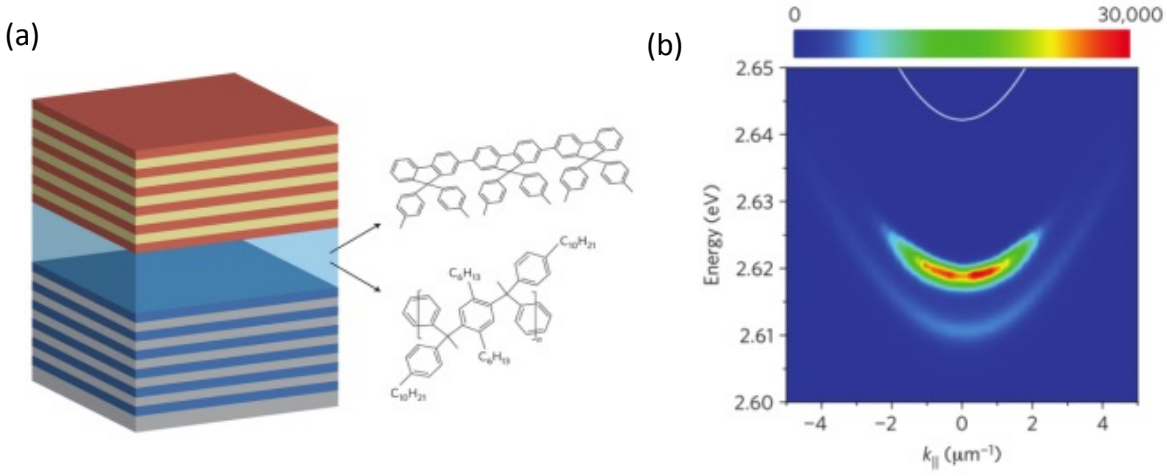

Figure 2.4: (a) Schematic image of an organic micro-cavity constituted by an organic (oligofluorene and polymer) thin film sandwiched in a pair of DBR mirrors.(b) Emergence of room temperature polariton BEC, evidenced by momentum resolved photoluminescence spectroscopy at the excitation intensity above the threshold in the polymer system shown in (a). Figures are from references [37, 69].

As polaritons have bosonic nature, cavity-polaritons are a topic of intensive study into macroscopic quantum-mechanical phenomena such as superfluidity, superconductivity, non-equilibrium BEC (a phase of matter in which many particles coalesce into a single quantum state) and thresholdless polariton lasing (not requiring population inversion).[19] Polariton lasing and BEC were reported with soft organic materials at room temperature.[36] In 2010, Kéna-Cohen and Forrest[68] demonstrated observation of room-temperature polariton lasing in an anthracene single-crystal microcavity. They showed that their polariton population occurs by the vibrational state assisted radiative decay of optically pumped incoherent excitons, rather than through polariton scattering. The latest results of Kéna-Cohen's group[67] and Mahrt et al.[69] presented experimental evidence of BEC at room temperature with strongly coupled organic materials (oligofluorene and conjugated polymer, shown in Fig. 2.4a), although these non-crystalline materials had not been expected to perform well owing to the destructive effects of disorder in condensed phases. Both groups showed the key feature of BEC (a power-dependent blueshift), a collapse of the polariton wavefunction at zero in-plane momentum (Fig. 2.4b), long range spatial coherence and increased temporal coherence above the emission threshold. The ease of fabrication of soft organic micro-cavities thus promises to push the development of new types of optical devices based on macroscopic quantum effects at room temperature.

Due to the low-mass of the polaritonic states, strong coupling has been supposed to inhibit the interaction with vibrations of molecules and relatively enhance their emission efficiency. For instance, Bulovic's group[83] demonstrated an emissive, electrically pumped exciton-polariton device by embedding polyelectrolyte/J-aggregate dye bilayers in a resonant organic LED (OLED) structure. Recently, a low-voltage polariton OLED has been displayed by an ultrastrongly coupled organic system in Kéna-Cohen's group.[70] Nevertheless, as we will see in this thesis, polariton emission quantum yields are typically very low.

Strong coupling is not only of interest in the field of optics but also can be utilized to modify chemical and bulk properties of organic materials. As mentioned previously, Schwartz et al.[71] achieved ultra-strong coupling by employing a photochrome dye with very large transition dipole in the metallic cavity (Fig. 2.5) or on plasmonic arrays. The

system showed a large Rabi splitting of about 700 meV, which is 32 % of the optical transition involved. Hutchison et al.[84] employed this system for modifying chemical landscapes and to control chemical reaction rates by strong coupling: the kinetics of conversion between the spiropyran and merocyanine state change when the molecules are in resonance with the cavity. Hutchison et al.[72] also showed the workfunction of the same photochrome dye in the merocyanine state could be tuned by strong coupling. When strongly coupling an excited state, the energy of ground state of molecules can also be pushed down, as analysed in a thermodynamic study.[66] Orgiu et al.[73] demonstrated the enhancement of conductivity of organic semiconductors by strong coupling. All these findings illustrate the potential of hybrid collective states engineered by interaction with the vacuum field.

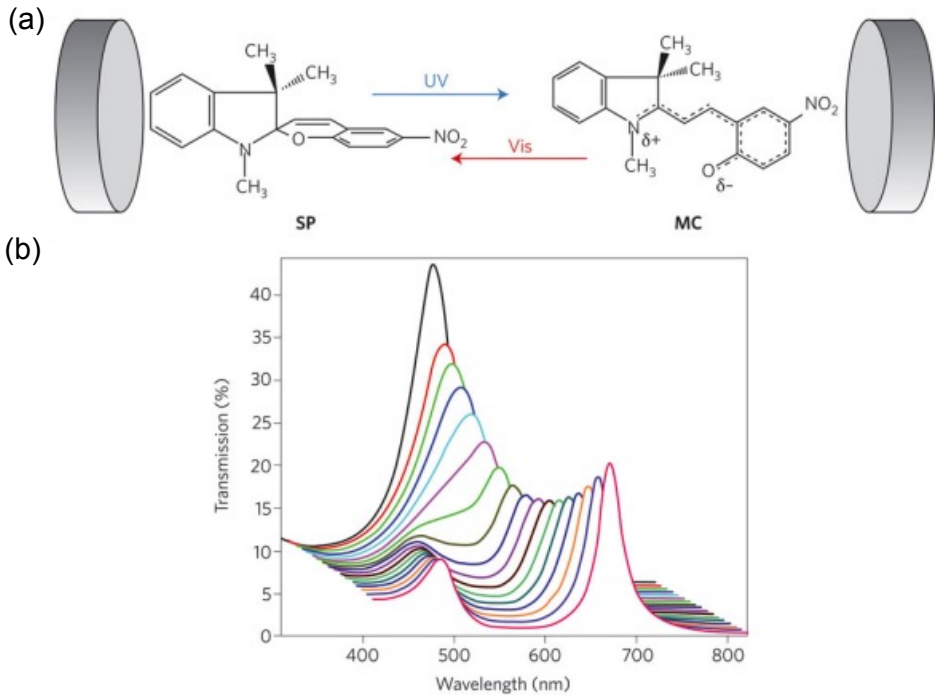

Figure 2.5: Observing ultra strong coupling. (a) Schematic of the photochromic conversion between merocyanine (MC) and spiropyran (SP) in a micro-cavity. (b) The evolution of transmission spectrum of the coupled system under UV illumination. The initial (black) spectrum corresponds to the SP molecules, not in resonance with the cavity mode. By exposing SP to 330 nm UV light, they are converted into MC, resulting in resonance with the cavity. As the concentration of MC increases, a transition from weak to strong coupling and eventually ultrastrong coupling occurs. Figures are from references [35, 84].

Recently, Shalabney and George et al. have shown that the vibrational transitions in the ground state can also be strongly coupled to an optical mode using microcavities in the infrared (IR) region.[85, 86] Subsequently, the spontaneous Raman scattering from such hybridized light-matter states was studied[74], showing that the collective Rabi-splitting occurs at the level of a single selected bond. Moreover, the coherent nature of the vibro-polariton states boosts the Raman scattering cross-section, providing a new enhancement mechanism as a result of coherent vibro-polaritonic states.[74]

2.4 Questions for further studies

Although much understanding of light-matter strong coupling has accumulated over the past 50 years, there are still many issues that remain open in the case of light-molecule strong coupling. The theory for strong coupling was developed for simple two-level systems and it is not clear whether this is adequate for coupling involving molecules which have far more complex energy diagrams involving numerous vibrational modes. Much experimental data is analyzed assuming that the earlier findings for semiconductor quantum wells and atomic systems holds for strongly coupled molecular systems. Typical issues that generate debate are for example the fraction of molecules that are coupled, the lifetime of the polaritonics states and spectral widths, the meaning of the observed Rabi splitting in terms of the energies of the new collective states and that at the molecular level. These questions are detailed below.

It is believed by some researchers that only a very small percentage of molecules are coupled to the optical mode. If this was the case, there would be no significant change in properties under strong coupling in contrast to the experimental observations as discussed in section 2.3. Naturally not all molecules will couple to the optical mode simply because of their orientation relative to the ***E***-field and their position inside the cavity, as we will see in Chapter 5. For a given condition, a stronger Rabi-splitting leads to a larger fraction of coupled molecules. Therefore optimizing the coupling strength by design, as presented in Chapters 4 and 5, is important.

Another question is whether strong coupling of an ensemble of N oscillators, which boosts the Rabi splitting by $\sqrt{N}$ and leads to the formation of the collective polaritonic states, perturbs the energy levels of the molecules involved by the same quantity. The theoretical description of ensemble Rabi-splitting will be discussed in Chapter 3. It is sometimes argued that on the scale of each molecule, the effective Rabi-splitting is the observed collective Rabi-splitting re-divided by $\sqrt{N}$. If this was the case the effect of the strong coupling on individual molecules would be negligible and it would significantly reduce its impact on material properties. Again the experimental evidence discussed in section 2.3 indicates that this view is not correct because significant changes in chemical and material properties are observed. Related examples, such as lifetime (Chapter 5) and ground state phenomena (Chapter 7), will strengthen our view in this issue.

The third question is in regard to the lifetimes of the polaritonic states. It is assumed by some that the lifetime of P+ and P- will be limited by the shortest lived constituent of the coupled system (typically the cavity). This is reasonable in the limit when the Rabi splitting is small and comparable to k_BT. In many cases such as in this thesis, the Rabi splitting is not only much larger than k_BT but also so large that the lifetime cannot simply be deduced directly from the lifetime of the constituents. In addition, it is clear that the line-width of static absorption spectra of the strong coupled system does not relate to population lifetime (Chapter 6). The situation is further complicated by the fact that the line-widths of the molecular absorption spectra are inhomogeneously broadened. The lifetime of the polaritons will be analyzed by different experimental approaches in Chapters 5 and 6 and compared to emission quantum yields.

A related issue is the meaning of the emission spectra of the coupled systems. After all, the shape of the emission spectra of the hybrid system can be reproduced by the product of the bare molecule emission and the optical density of states. In other words, the P- emission spectra can be explained by the "filter effect" of optical resonances on the uncoupled molecular emission as discussed in Chapter 6, where we try to understand the meaning of the emission peaks of strongly coupled system.

The fourth question is to what extent the measured absorption peaks of the coupled system represent transitions to real polaritonic states. As we know, the static absorption

spectra can be perfectly fitted by the classical approach, e.g. transfer matrix method, without the assumption of the existence of new hybrid light-matter states as pointed out by Zhu et al years ago[87]. It has become clear from our various studies that the absorption peaks do not necessarily match the transitions to the polaritonic states. Excitation spectroscopy in Chapter 6 and even thermal dynamics analysis in Chapter 7, provide information about the energy levels of the hybrid states and their intrinsic properties. Very recently, the Raman spectrum of vibro-polariton states was found to be totally different from the static absorption spectrum.[74] It confirms that the static linear spectrum may not provide information about the true energies of the hybrid states.

The work in this thesis tries to contribute among other things to the clarification of the above issues of light- molecule strong coupling. In the next chapter, we start by presenting the standard theory in the strong coupling regime before presenting the experimental results.

3 Theoretical description of strongly coupled systems

In the previous chapter, the basic features of strongly coupled systems were introduced. In this chapter, a more detailed theoretical description will be provided which successfully predicts experimental observations of strongly coupled systems, for instance anti-crossing behavior. Static optical spectra of the coupled system will be derived and simulated in the classical case by treating linear macroscopic susceptibility. Subsequently, vacuum Rabi-splitting, the ground state shift, and the delocalized nature of the wavefunction will be quantitatively demonstrated by deriving the Hamiltonian for the system. Both the simple classical Lorentzian, the quantum Jaynes-Cummings and Tavis-Cummings model give insights into the physics of strong coupling.

3.1 Classical description

We start by describing the matter in terms of Lorentzian oscillators, composed of point-like electric dipoles[1, 2]. The dipoles respond harmonically to the EM field confined by the optical structures. Supposing that each electron of charge -*e*, in a medium is displaced a distance *r* from its equilibrium position. The resulting macroscopic polarization density *P* of the medium is given by

$$P = -\frac{N}{V} e r \tag{3.1}$$

where N/V is the number of dipoles N per unit volume V. If the local field of the dipoles is neglected[88], the equation of motion for an electron bounded by a harmonic force and driven by an external EM field $E(\mathrm{r}, t)$ is

$$m(\frac{\mathrm{d}^2 r}{\mathrm{d}t^2}+\gamma\frac{\mathrm{d}\ r}{\mathrm{d}t}+\omega_0^2 r)=-\mathrm{e}E(r,t) \tag{3.2}$$

here m is the mass of electron, ω_0 is the frequency of the harmonic oscillator and γ measures the phenomenological damping force. Magnetic force effects are neglected in eqn. (3.2).

Now we suppose that the applied EM field varies harmonically with time according to the usual factor $e^{-i\omega t}$. Within the normal dipole approximation, the EM field is constant in r since the electron movement is small compared to the wavelength of the EM field in the scale of visible light. As the motion of the electron has the same harmonic time dependence, eqn. (3.2) becomes

$$m(-\omega^2-i\omega\gamma+\omega_0^2)r=-\mathrm{e}E \tag{3.3}$$

Consequently, the polarization, from eqn. (3.1), is given by

$$P=\frac{N\mathrm{e}^2}{Vm}\frac{1}{\omega_0^2-\omega^2-i\omega\gamma}E \tag{3.4}$$

As we know, the linear polarization is defined as

$$P=\varepsilon_0\chi E \tag{3.5}$$

where ε_0 is the vacuum permittivity, χ is the macroscopic electric susceptibility. Thus we obtain

$$\chi(\omega)=\frac{A}{\omega_0^2-\omega^2-i\omega\gamma} \tag{3.6}$$

where we have denoted $A=\frac{N\mathrm{e}^2}{V\varepsilon_0 m}$. The permittivity of the medium is associated with the susceptibility through

$$\varepsilon(\omega)=1+\chi(\omega) \tag{3.7}$$

Considering our experimental cases, the momentum-energy dispersion of a transverse EM wave in a FP cavity or propagating on the metal surface can be simplified as[13, 42, 63]

$$k = \frac{\omega}{c}\sqrt{\varepsilon(\omega)} \tag{3.8}$$

More details about optical mode frequency tuned by angular momentum associated with this equation will be discussed in the following Chapters 4 and 5. The momentum k is replaced by κ (κ=kc) and eqn. (3.8) then becomes

$$\kappa^2 = \omega^2\varepsilon(\omega) = \omega^2(1 + \frac{A}{\omega_0^2 - \omega^2 - i\omega\gamma}) \tag{3.9}$$

Then for the case that ω is quite close to ω_0, an approximate derivation of eqn. (3.9) is

$$(\kappa - \omega)(\omega_0 - \omega - i\frac{\gamma}{2}) = \frac{A}{4} \tag{3.10}$$

Eqn. (3.10) is the well-known dispersion relation for coupling of material dipoles and an EM field. Its two solutions correspond to two new normal modes of the system in terms of

$$\omega_{\pm} = \frac{\kappa}{2} + \frac{\omega_0}{2} - i\frac{\gamma}{4} \pm \frac{1}{2}\sqrt{A + (\kappa - \omega_0 + i\frac{\gamma}{2})^2} \tag{3.11}$$

At resonance, $\kappa = \omega_0$

$$\omega_{\pm} = \omega_0 - i\frac{\gamma}{4} \pm \frac{1}{2}\sqrt{A - \frac{\gamma^2}{4}} \tag{3.12}$$

The above results neglect the dissipation of the optical modes. In our experiments, the lifetime of cavity (or surface plasmon modes) is limited to ~10 fs. κ can be replaced with κ-$i\gamma_{OM}$/2 to include the losses of optical modes.[13] Eqn. (3.12) is then

$$\omega_{\pm} = \omega_0 - i\frac{\gamma}{4} - i\frac{\gamma_{OM}}{4} \pm \frac{1}{2}\sqrt{A - (\frac{\gamma}{2} - \frac{\gamma_{OM}}{2})^2} \tag{3.13}$$

Eqns. (3.11)-(3.13) show that the two new normal modes $\omega_{\pm}$ inherit the damping of both the optical mode and the oscillator. They dissipate with linewidths in terms of $\frac{\gamma + \gamma_{OM}}{2}$. At resonance, the energy gap between $\omega_{\pm}$, known as the Rabi frequency or Rabi splitting, is given by

$$\Omega_R = \sqrt{A - (\frac{\gamma}{2} - \frac{\gamma_{OM}}{2})^2} \tag{3.14}$$

If the damping and losses of the systems are neglected, namely in the $\gamma = 0$ and $\gamma_{OM} = 0$ case, the Rabi frequency becomes

$$\Omega_R = \sqrt{A} = \sqrt{\frac{N}{V}} \frac{e}{\sqrt{\varepsilon_0 m}} \tag{3.15}$$

We have thus obtained and analyzed result of eqn. (3.9) and derived the energy splitting. The exact solutions of eqn. (3.9) are presented in Fig. 3.1, which plots the energy of two normal modes $\omega_{\pm}$ as a function of photon energy tuning, assuming the parameter A as ω_0^2. We see that around resonance energy of the original matter and optical modes the two branches of new normal modes do not cross (represented by the horizontal and slope dotted line), but instead avoid each other. The new normal modes tend asymptotically towards the bare matter and optical modes in the frequency ranges far away from resonance. This dispersion behaviour is often referred to as an "anti-crossing" and is a typical proof for strong coupling in experiments. In general, strong absorption at a particular frequency is likely to result in the changes in the dispersion curve e.g. anti-crossing, which are associated with hybrid character of the modes. These kinds of hybrid modes are broadly observed in light and matter interactions, such as surface plasmon polaritons[13], surface phonon polartions[89, 90], and surface exciton polaritons[91].

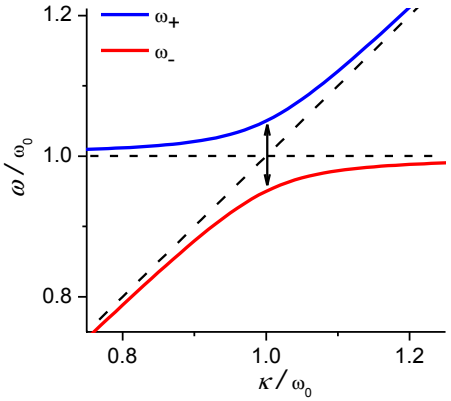

Figure 3.1: Dispersion of the upper and lower branches of the new normal modes of the coupled system as a function of tuning of the optical mode and material oscillator energies, with anti-crossing energy equal to the Rabi frequency $\Omega_R = 0.1\omega_0$. The calculation neglects the dissipations of the coupled system. The horizontal and sloped dotted lines display the energy of the matter and dispersion of optical modes respectively in the absence of coupling.

The above simple model is well-suited to describe the basic physics of strong coupling between Lorentzian oscillators and optical modes. However, the line-shapes of various solid media (e.g. organic molecules) are often more complicated due to inhomogeneous broadening and vibrational manifolds[60, 64, 77]. To better model these more complex experimental line-shapes, a numerical method is often utilized: the optical response of the matter in the cavities or on the plasmonic structures can be modeled by inserting the materials' contribution to the refractive index n into Maxwell's equations[71, 87]. Herein, we take a layer of cyanine J-aggregates sandwiched in a metallic FP cavity as an example. The imaginary part of the refractive index n'' is known as the extinction index, which can be measured from the absorption spectrum $a(\omega)$. The two numbers n'' and a are related by the equation

$$a = \frac{\omega}{c} n'' \tag{3.16}$$

The real part, n', can be calculated by employing the Kramers-Kronig relations

$$n' = 1 + \frac{2}{\pi} \Re \int_0^\infty \frac{\omega' n''(\omega')}{\omega'^2 - \omega^2} \mathrm{d}\omega' \tag{3.17}$$

where $\Re$ represents the principal value. Then the real and imaginary parts of permittivity ε' and ε'' can be calculated by their relationship with the refractive index

$$\varepsilon' = n'^2 - n''^2 \tag{3.18}$$

$$\varepsilon'' = 2n'n'' \tag{3.19}$$

Figs. 3.2a and b show how n' and n'' depend on the energy $\hbar\omega$. The absorption is strongest at the resonance frequency ω_0. n' is greater than the background (as 1.5 in this case) for small frequencies and increases with ω as ω_0 is approached. This is the case of "normal" dispersion. At or near ω_0, however, the dispersion becomes "anomalous" in the sense that n' decreases with increasing ω. The peak and dip of the n' curve can thus produce two new normal modes in a Fabry-Pérot cavity with opposite phases and $n'(\omega_0)$ corresponds to the original optical mode. This expectation is completely matched by the optical spectra of the coupled system calculated utilizing the transfer matrix formalism (see Figs. 3.2c, d and e).

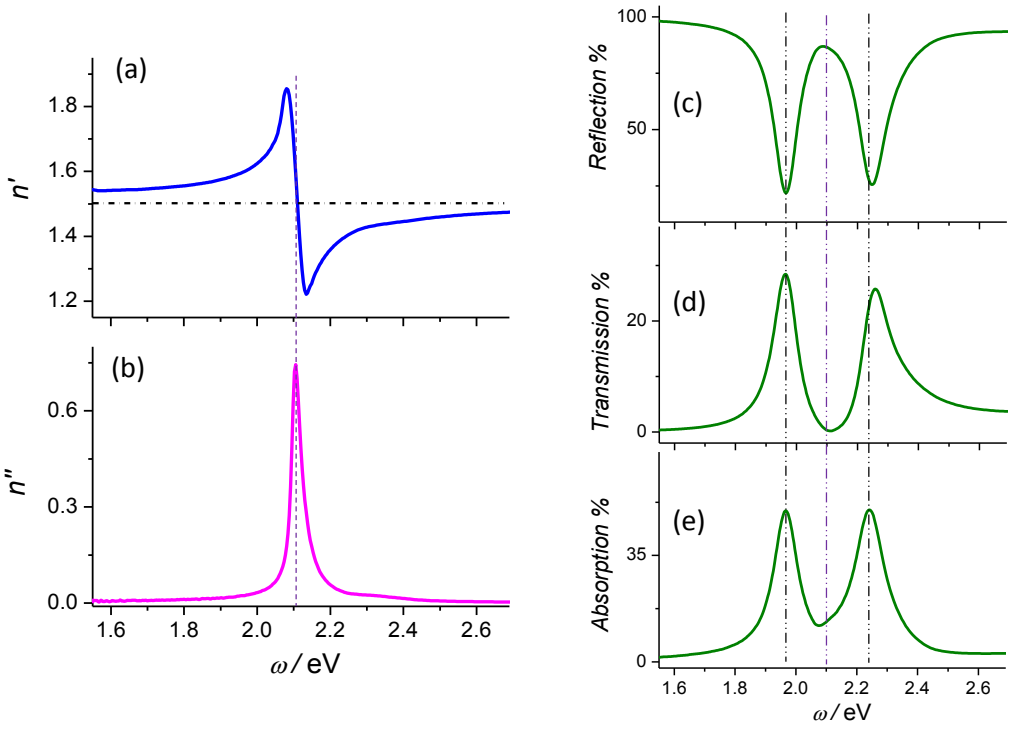

Figure 3.2: The real (a) and imaginary (b) part of refractive index of cyanine J-aggregates (TDBC) dispersed in a polymer (PVA) matrix. The vertical line shows the resonant frequency ω_0 of this dye and the horizontal line in (a) corresponds to the background refractive index. (c), (d) and (e) are the calculated reflection (R%), transmission (T%) and absorption (A%) spectra of the coupled system respectively, demonstrating that the original resonant mode (denoted by the middle dash-dotted line) splits into two new normal modes (the dash-dotted lines) when a 146 nm thick dye layer deposited in a resonant cavity defined by two 30 nm thick Ag films (A%=1- T%- R%).

3.2 Quantum description

3.2.1 Two-level system

In the framework of a full quantum theory for light-matter strong coupling, the description of the light-matter interaction relies on the interplay between two basic systems: a simple two energy level system (a 1/2 spin) and a quantized field (a 'spring').[92] The matter part, the 1/2 spin, possesses an excited state $|e\rangle$ and a ground state $|g\rangle$. ω_0 is the angular frequency of the electric dipole transition connecting the ground and excited state. We first consider a single two-level system interacting with a quantized EM field (see Fig. 3.3).

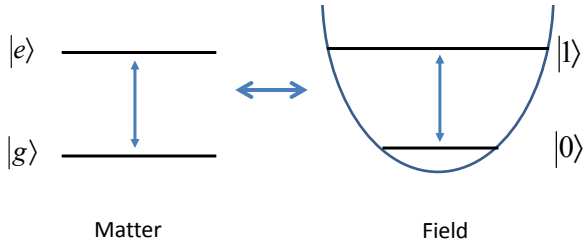

Figure 3.3: An excitation exchange between a single two-level system with a quantized photonic mode.

Let us define several vector bases and operators in the form of matrices in advance. The excited state $|e\rangle$ and the ground state $|g\rangle$ of the matter part are presented as $\begin{pmatrix}1\\0\end{pmatrix}$, and $\begin{pmatrix}0\\1\end{pmatrix}$ respectively. The spin-1/2 operators $\sigma_{\pm,z}$ are given by

$$\sigma_+ = |g\rangle\langle e|,\ \sigma_- = |e\rangle\langle g| \text{ and } \sigma_z = |e\rangle\langle e| - |g\rangle\langle g| \tag{3.20}$$

where transition from the ground to excited state is then expressed as $\sigma_+ = \begin{pmatrix}0 & 1\\0 & 0\end{pmatrix}$ and the inverse process by $\sigma_- = \begin{pmatrix}0 & 0\\1 & 0\end{pmatrix}$. We denote the energies of the states of a spin by $\sigma_z = \begin{pmatrix}1 & 0\\0 & -1\end{pmatrix}$. Within the rotating wave approximation (RWA), the well-known Jaynes-Cummings Hamiltonian [93] can describe the energies of the light-matter coupling system

$$H_{JC} = \frac{1}{2}\hbar\omega_0\sigma_z + \hbar\omega a^+ a - i\frac{\hbar\Omega_R}{2}(a\sigma_+ - a^+\sigma_-) \tag{3.21}$$

$$\Omega_R = (\frac{2d}{\hbar})\xi_0 \tag{3.22}$$

$$\xi_0 = \sqrt{\frac{\hbar\omega}{2\varepsilon_0 V}} \tag{3.23}$$

where Ω_R is the Rabi-frequency[8], d is the transition dipole moment of matter, ξ_0 is the "electric field amplitude per photon" in the mode volume V. a (a^+) is the bosonic creation (annihilation) operator, corresponding to the creation (destruction) of a photon. In the case that one photon is absorbed/emitted when the matter makes a transition between the

ground and the excited states, the Jaynes-Cummings Hamiltonian only couples the states $|e\rangle|0\rangle$ and $|g\rangle|1\rangle$.

Let's introduce the parameter $\Delta=\omega-\omega_0$, measuring the detuning of the field mode frequency relative to the electronic transition. In the basis $\begin{pmatrix}1\\0\end{pmatrix}=|e\rangle|0\rangle$, $\begin{pmatrix}0\\1\end{pmatrix}=|g\rangle|1\rangle$, the Hamiltonan reads

$$H_{JC}=\frac{\hbar(\omega+\omega_0)}{2}\begin{pmatrix}1&0\\0&1\end{pmatrix}+\frac{1}{2}\begin{pmatrix}-\Delta&-i\Omega_R\\ i\Omega_R&\Delta\end{pmatrix} \tag{3.24}$$

From the straightforward diagonalization we derive the new energy eigenvalues

$$E_{\pm}=\frac{\hbar(\omega+\omega_0)}{2}\pm\frac{1}{2}\sqrt{\Delta^2+\Omega_R{}^2} \tag{3.25}$$

The dispersion of the two associated eigenstates as a function of tuning of the photonic mode ($\hbar\omega$) will display the same anti-crossing effect as shown in Fig. 3.1.

Those two states are well known polaritonic eigenstates $|P\pm\rangle$

$$|P+\rangle=\cos\theta|e\rangle|0\rangle+i\sin\theta|g\rangle|1\rangle \tag{3.26}$$

$$|P-\rangle=\sin\theta|e\rangle|0\rangle-i\cos\theta|g\rangle|1\rangle \tag{3.27}$$

with the angle θ defined by

$$\tan(2\theta)=-\frac{\Omega_R}{\Delta} \tag{3.28}$$

On resonance, i.e. at zero detuning, $\Delta=0$, the angle θ is calculated as $\pi/4$ and the polaritonic states are two maximally entangled states

$$|P_{res}+\rangle=\frac{1}{\sqrt{2}}(|e\rangle|0\rangle+i|g\rangle|1\rangle) \tag{3.29}$$

$$|P_{res}-\rangle=\frac{1}{\sqrt{2}}(|e\rangle|0\rangle-i|g\rangle|1\rangle) \tag{3.30}$$

In this situation, the polaritonic states of the system are an equal superposition of the ground state + one photon in the cavity, and the excited state + no photon in the cavity. The polariton's wavefunction is not localized but extends over the volume of the field mode due to its partial photonic character. Moreover, the time-evolution for an initial ground state plus one extra photon is given by[13]

$$|\Psi(t)\rangle = \cos(\Omega_R t/2)|g\rangle|1\rangle - i\sin(\Omega_R t/2)|e\rangle|0\rangle \tag{3.31}$$

We can thus obtain the probability of being in state $|g\rangle|1\rangle$

$$P = \cos^2(\Omega_R t/2) = \frac{1+\cos(\Omega_R t)}{2} \tag{3.32}$$

This means the system performs Rabi oscillations between the states $|g\rangle|1\rangle$ and $|e\rangle|0\rangle$ (Fig 3.4). At resonance the frequency of these oscillations is the Rabi frequency Ω_R.

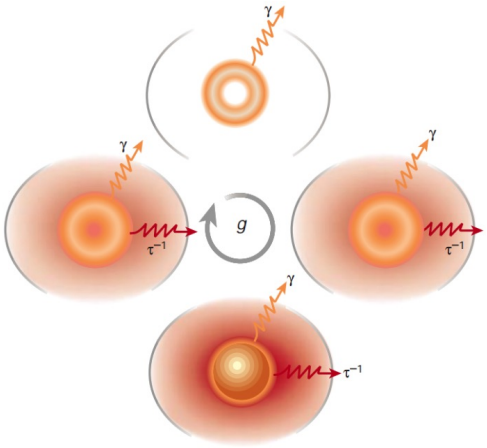

Figure 3.4: Rabi oscillation. An excited atom (a typical two-energy level system) is introduced into the cavity (top) and undergoes vacuum Rabi oscillation mediated by the atom-field coupling strength, $g = \Omega_R/2$, resulting in one quantum being added to the mode (shown in red) (bottom). Dissipation mechanisms are also illustrated although not discussed in the main text. γ is the atomic damping rate and τ is the cavity lifetime. Figure is from reference[94].

The above results are in the limit of the RWA. However, the RWA is invalid in the ultrastrong coupling regime, which is characterized by a coupling of the same order of magnitude as ω_0. In this case, one cannot neglect the anti-resonant part of the Hamiltonian. The full Hamiltonian is

$$H = \frac{1}{2}\hbar\omega_0\sigma_z + \hbar\omega a a^+ - i\frac{\hbar\Omega_R}{2}(a - a^+)(\sigma_- + \sigma_+) \tag{3.33}$$

Diagonalizing this Hamiltonian in the subspace ($|g\rangle|0\rangle, |g\rangle|1\rangle, |e\rangle|0\rangle, |e\rangle|1\rangle$), we get two more eigenstates: a new ground state of the coupled system $|GS\rangle$ and a doubly excited state $|DE\rangle$. They are accessed by coupling between the states $|g\rangle|0\rangle$ and $|e\rangle|1\rangle$. Note that

the ground state of the system has shifted ΔG with respect to the uncoupled ground state. ΔG, neglected in the usual RWA can become important as the relative coupling strength (Ω_R/ω_0) is increased[95]

$$\Delta G = \omega_0(1-\sqrt{1+\frac{1}{4}(\Omega_R/\omega_0)^2}) \tag{3.34}$$

3.2.2 Collective Rabi-splitting

In the last section, we consider the many-body case which is most relevant to organic molecule strong coupling experiments. The collection of N two-level systems acts like a giant quantum oscillator $\sqrt{N}$ d after introducing a new bosonic operator, b, and the so-called Dicke[96] or Tavis-Cummings[97] Hamiltonian becomes approximately (neglecting all damping processes)[98]

$$H^N \approx \hbar\omega_0 (\frac{N}{2}+\mathrm{b}^+\mathrm{b})+\hbar\omega a^+a - i\frac{\sqrt{N}\hbar\Omega_R}{2}(a^+b-ab^+) \tag{3.35}$$

The ground state $|G\rangle|1\rangle$ and excited state $|D\rangle|0\rangle$ of the ensemble of N two-level systems with one excitation are given by

$$|G\rangle|1\rangle = (|g,g,...g\rangle)|1\rangle \tag{3.36}$$

$$|D\rangle|0\rangle = \frac{1}{\sqrt{N}}(\sum_{i=1}^{N}|g,...e_i,...g\rangle)|0\rangle \tag{3.37}$$

This is an approximate system of two coupled oscillators, one associated with the Dicke spin and the other with the EM field. Solving the polaritonic engienstates of H^N leads to a vacuum Rabi splitting:

$$\hbar\Omega_R = 2\sqrt{N}d\xi_0 \tag{3.38}$$

Eqn. (3.38) tells us that the strength of the light-matter coupling can be increased by two methods: by increasing the effective transition dipole moment $\sqrt{N}d$ of the matter part, or by enhancing the EM field magnitude (e.g. confining the light into smaller mode volume structures). The theoretical treatments reviewed here have enriched the whole history of strong coupling research reviewed in Chapter 2.

In theory, the Rabi splitting is supposed to increase as $\sqrt{n_{ph}+1}$ where n_{ph} is the number of photons in the mode and 1 represents the vacuum field.[92] In the experiments detailed in the following chapters, the light-matter strong coupling is always in the vacuum field limit. The total population of excited states does not exceed a fraction of 10^{-7} in our case of static spectroscopic experiments[77] and even in the pump-probe experiments the fraction of excited molecules is on the order of 1%. Intensity studies show the Rabi splitting is unaffected in these experiments and therefore confirm that the systems are coupled in the vacuum field limit.

Part II.

Results

4 Strong light-molecule coupling on plasmonic structures

In this chapter we will focus on the strong coupling between surface plasmon polaritons (SPPs) and organic molecules. Firstly, the dispersive and evanescent properties of SPPs will be introduced. Subsequently, coupling light to SPPs with different plasmonic structures (such as hole arrays, bull's eyes, and groove gratings) will be illustrated using transmission spectra. In the second section, the strong coupling of porphyrin J-aggregates to plasmonic nanostructures of different symmetry will be investigated. Finally, the photoluminescence of strongly coupled systems on dimple arrays will be studied with a cyanine dye.

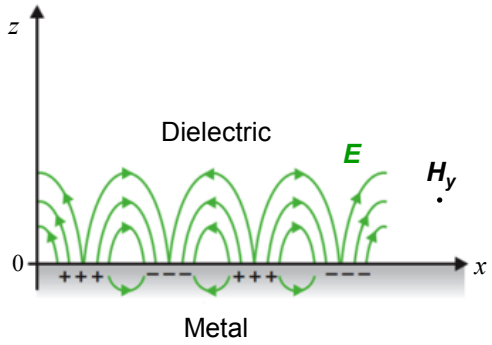

Figure 4.1: Electric field (***E***) and surface charge distributions associated with surface plasmon propagation a metal-dielectric interface.

4.1 Surface plasmon polaritons

SPPs are EM waves that propagate along the interface between a metal and a dielectric.[99, 100] These EM waves involve a mixture of both photon and charge fluctuations on the metal surface; therefore, they have a unique hybrid character whereby EM field is concentrated in volumes much smaller than the diffraction limit and it is thus favorable to observe strong coupling effects. Moreover, the SPPs are transverse magnetic (TM) modes in character (magnetic field ***H*** is in the y direction) and the surface charge fluctuations requires an electric field normal to the surface as illustrated in the Fig. 4.1.

4.1.1 Dispersion of SPPs

The resonant interaction between the surface charges and the EM field of the light that constitutes the SPPs has two consequences. First, the momentum of the propagating SP modes, $\hbar k_{SP}$ is greater than that of light propagating in free-space at the same frequency, $\hbar k_0$ ($k_0 = 2\pi/\lambda$ is the free space wave vector). The wave vector of the SPPs lying along the interface, k_{SP} is determined by the dispersion relation[101]

$$k_{SP} = k_0 \sqrt{\frac{\varepsilon_d \varepsilon_m}{\varepsilon_d + \varepsilon_m}} \tag{4.1}$$

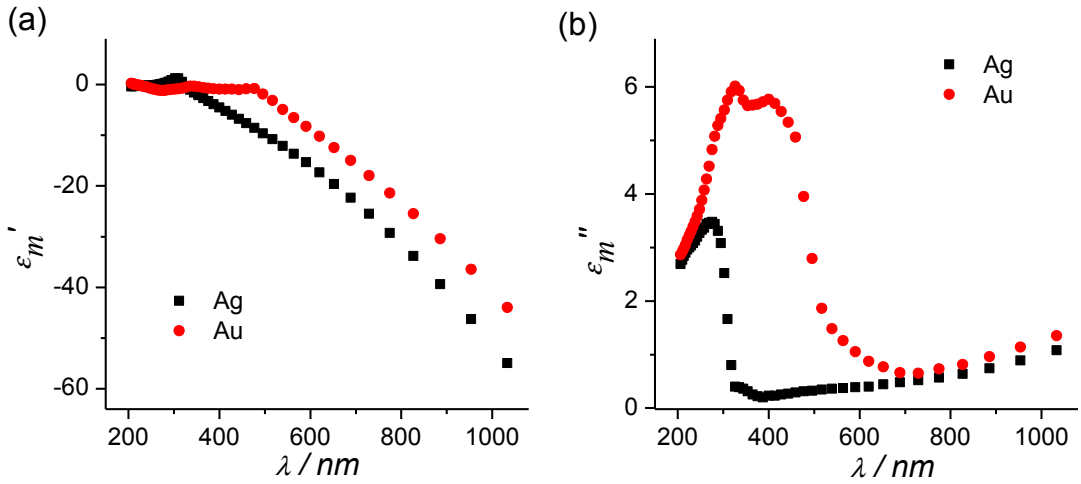

Figure 4.2: The real (a) and imaginary part (b) of the permittivity of silver (Ag) and gold (Au) as a function of wavelength is taken from Babar and Weaver.[102]

where ε_d and ε_m are the permittivities of the infinite dielectric and metal media, respectively. The solution of k_{SP} is satisfied at metal/dielectric interfaces at wavelength regions where the complex permittivity of the metal, $\varepsilon_m = \varepsilon_m' + i\varepsilon_m''$, has a negative, real part (ε_m') (in Fig. 4.2a are shown examples of the permittivity of bulk silver and gold). Note that in regions where absorption and thus the imaginary part (ε_m'') is high, for instance at the interband transitions of gold at 400-500 nm (Fig. 4.2b), SPPs are rapidly dissipated. It suggests that a silver film is a better choice to generate surface plasmon resonances in the visible range from 400 nm to 600 nm than a gold film.

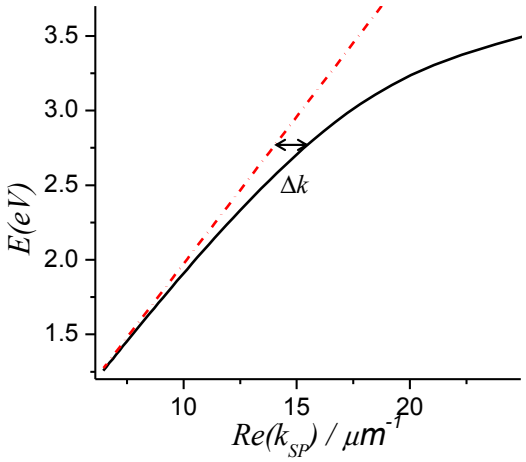

Figure 4.3: Comparison of the dispersion curves of SPPs at an Ag-air interface (solid line) with that of freely propagating light in the dielectric medium, in this case air (dotted line).

The dispersion of SPPs at an Ag-air interface in the energy range 1.3 eV to 3.5 eV is shown in Fig. 4.3 by substituting the permittivity data of Fig. 4.2 into eqn. (4.1). In the range of lower energies, the dispersion curve of the SPPs is asymptotic to that of freely propagating light (the dotted line in Fig. 4.3), at these energies the SPPs is similar to a grazing surface wave and weakly bound to the interface. At higher energies, the coupling between the EM field and surface charge density oscillations becomes stronger, and the wave vector (momentum) of the SPPs k_{SP} turns away from the light line. Here the EM wave is more strongly bound to the surface. It is clear from Fig. 4.3 that the wave vector mismatch, Δk , between k_{SP} and k_0 at the same resonance wavelength should be

compensated for if freely propagating light is to be coupled to SPPs. For instance, SPPs can't be excited by illuminating the interface with a plane wave. Methods to excite SPPS will be discussed in section 4.1.3.

4.1.2 Evanescent properties of SPPs

Due to the relation $\sqrt{\varepsilon_{d,m}}k_0 < k_{SP}$, the wave vectors of SPPs normal to the surface, $k_z^{d,m} = \sqrt{\varepsilon_{d,m}(k_0)^2 - (k_{SP})^2}$, are imaginary. The second consequence of coupling between EM waves and charge density oscillations is thus that the SPP field is evanescent perpendicular to the surface and decays exponentially into the metal on one side and into the dielectric on the other. The SPPs' spatial extension to dielectric or metal can be quantitatively described by the skin depth. Its value at which the SPP field falls to 1/e[101]

$$z^{d,m} = \frac{1}{\left|k_z^{d,m}\right|} \tag{4.2}$$

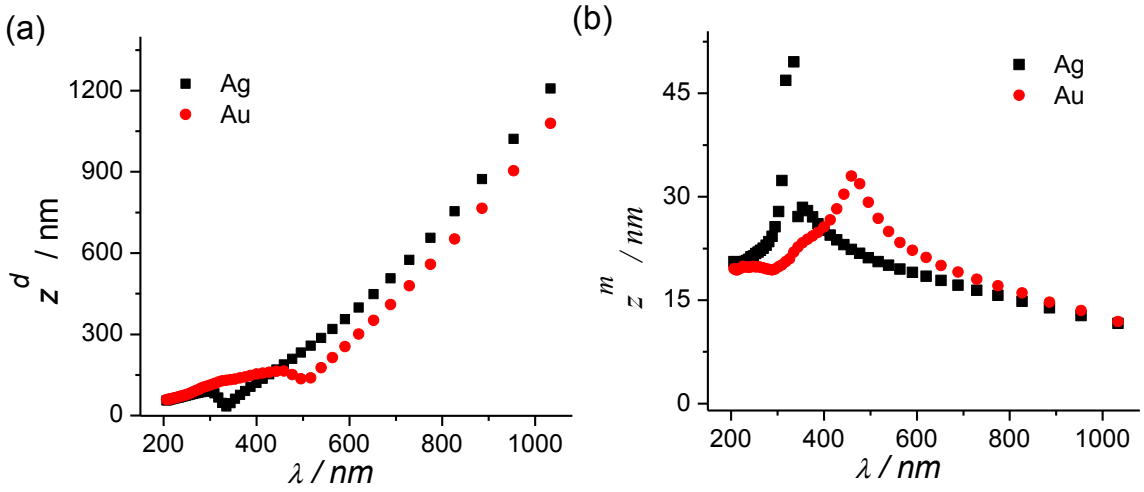

Figure 4.4: The spatial extension of SPPs into the dielectric z^d (a) or metal z^m (b) media as calculated from eqn. (4.2) for Ag-air and Au-air interfaces.

Using the eqn. (4.2), the $z^{d,m}$ values *vs* wavelength for Ag-air and Au-air interfaces are calculated and included in Fig. 4.4. In the visible range, the z^d values are near λ/2, leading to a small mode volume and strong concentration of the field near the surface, which provides an efficient tool for observing strong coupling in the context of

this thesis. In addition, z^d is much smaller at larger energies than at smaller ones, as per the dispersion of the SPPs away from the light line and into the evanescent zone as displayed in Fig. 4.3. Moreover, except around the energies of the metal's interband absorption, the SPP field penetrates into the metal to a depth ~ 20 nm, far less than into the dielectric due to the screening by the charges in the metal.

4.1.3 Excitation of SPPs by sub-wavelength metallic structures

With the characteristic features of SPPs in mind, we discuss next how to efficiently excite them. It has been noted that the coupling between freely propagating light and SPPs requires specific conditions in order to ensure momentum conservation. There are several techniques to achieve this, such as Otto[103] or Kretschman-Raether[104] prism coupling, leakage radiation spectroscopy[105, 106], scattering on a single sub-wavelength hole or slit[107-110], and grating diffraction[111].

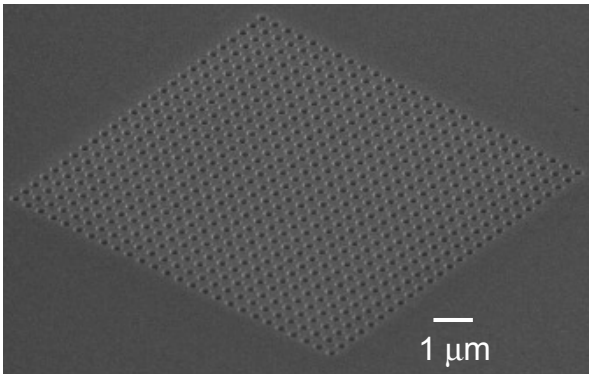

Figure 4.5: An Ag square hole array with period P = 400 nm, hole diameter D =150 nm, milled by focused ion beam (FIB).

Of specific interest for us is the use of sub-wavelength metallic hole arrays (see Fig. 4.5) to excite SPPs, which are generated via Bragg scattering according to the following equation[112]

$$\left|\vec{k}_{SP}\right| = \left|\vec{k}_{//} + i\vec{G}_x + j\vec{G}_y\right| \tag{4.3}$$

where $k_{//}$ is the in-plane wave vector component of the incident light, $\vec{G}_x$ and $\vec{G}_y$ are the reciprocal lattice vectors ($|\vec{G}_x| = |\vec{G}_y| = 2\pi/P$, and P is the lattice period), and i and j are integers. The scattering orders of SPPs modes are denoted by (i, j).

One of the interesting phenomena of such coupling is the observation of extraordinary optical transmission through holes with lateral dimensions which are smaller than half the wavelength of incident light.[112] The peak positions are associated with surface plasmon array excitations, with wavelength λ_{SP}, which can be described at normal incidence by the following equation

$$\lambda_{SP} = \frac{P}{C}\sqrt{\frac{\varepsilon_d \varepsilon_m}{\varepsilon_d + \varepsilon_m}} \tag{4.4}$$

where C is given by $\sqrt{i^2 + j^2}$ for a square array, and $\sqrt{\frac{4}{3}\left(i^2 + ij + j^2\right)}$ for a hexagonal array. Eqn. (4.4) shows that tuning plasmonic modes to a desired frequency can be achieved by changing the array's periodicity (so called periodic dispersion) or by changing the angle of incident light θ (angular dispersion) associated with $k_{//}$ for a fixed periodicity

$$k_{//} = k_0 \sin\theta \tag{4.5}$$

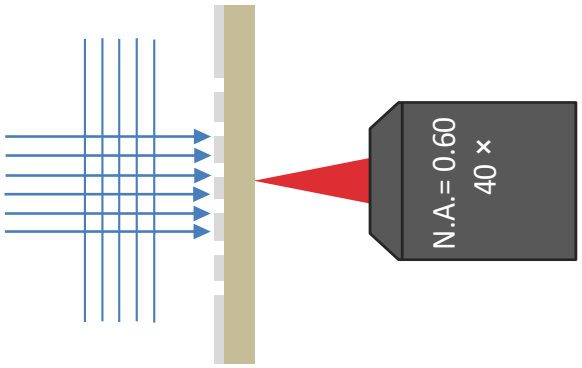

Figure 4.6: Schematic presentation of the acquisition of transmission spectra of plasmonic structures: the nanostructure is illuminated with collimated light and the light transmitted by the nanostructure is then collected by a microscope objective lens.

The transmission spectra of plasmonic nanostructrues can be simply measured by the method shown in Fig. 4.6. The sample is aligned on the optical axis of the microscope

and illuminated with collimated light. The light transmitted by the nanostructure is then collected using a microscope objective lens (e.g. 40× magnification and numerical aperture (N.A.) of 0.60) which is connected to a spectrometer (Acton SpectraPro 300i) and a silicon charge-couple device (CCD) (Princeton Instrument VersArray 1300B).

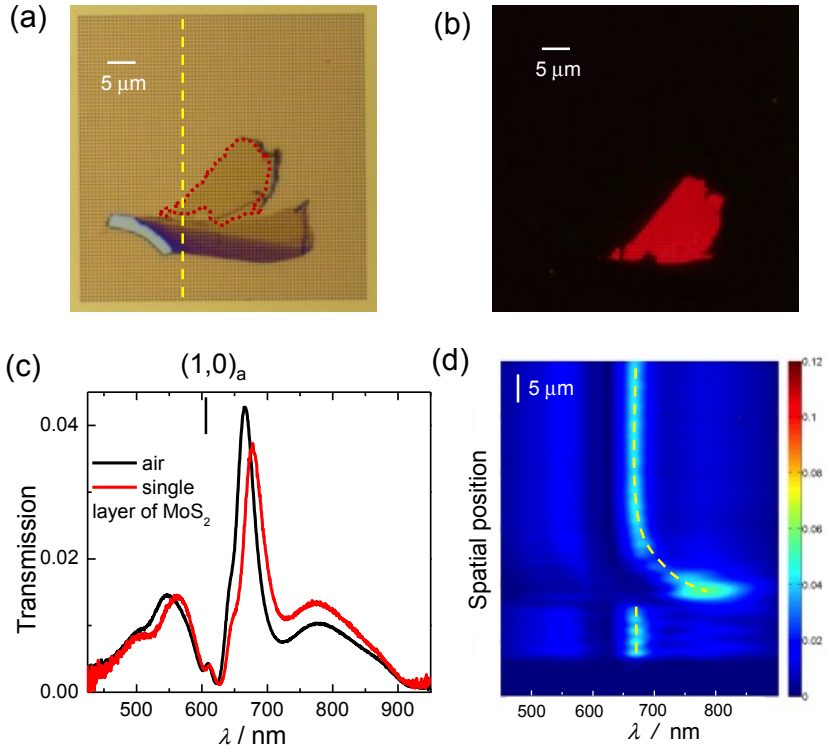

Figure 4.7: a) Optical micrograph of a layered semiconductor MoS_2 on a square hole array in gold film (P= 600 nm, D = 175 nm), (b) A photoluminescence image of the same area (excited by 480 nm). The luminescent part corresponds to a zone of single atomic layer MoS_2 (indicated by the red dotted line in (a)), (c) The normal incidence transmission spectra of a bare part of the hole array (black curve) and the part with a single layer of MoS_2 on top (red curve).The vertical line corresponds to the theoretical $(1,0)_a$ SP resonance (see text). (d) Intensity plot of the transmission spectrum of the hole array as a function of spatial position along the yellow vertical line in (a). The color bar represents the transmitivity.

The experiments in the rest of this section investigate SPP resonances as a function of surface dielectric constants, period of hole arrays, and degeneracy of SPPs modes. The black curve in Fig. 4.7c shows the transmission spectra of a square hole array with hole diameter 175 nm, period 600 nm on a glass substrate, which is milled in a 200 nm gold film with 5 nm of chrome at the bottom. The predicted theoretical resonance of the $(1, 0)_a$ air mode (indicated by the vertical line in Fig. 4.7c) is in fact at a transmission minimum

and located at a shorter wavelength than the experimental peak. The glass modes are attenuated by the 5 nm chrome film, also shown for comparison in Fig. 4.7c. Moreover, the shape of peak (e.g. the $(1, 0)_a$ air mode) is not Lorentzian but Fano-type. The displacement and Fano shape are the result of an interference effect between a resonant (SPPs) contribution and a continuum of directly transmitted light (direct scattering and diffraction).[113]

After transferring a layered semiconductor (MoS_2) on the same hole array (see Fig. 4.7a), the transmission peaks of air modes are red-shifted. The red curve of Fig. 4.7c displays the result for a single atomic layer (6.5 Å)[114] of MoS_2 by measuring the red, circled zone in Fig. 4.7a. This is confirmed to be a single layer of MoS_2 since it is highly luminescent (Fig. 4.7 b). The peak of the $(1, 0)_a$ air mode red shifts from 665 nm to 677 nm due to the influence of the single atomic layer (effective refractive index 1.018). This experiment shows clearly that the surface plasmon resonance of a hole array can be applied as a highly sensitive sensor[115] and that, for instance, the layer number of the MoS_2 can be tested by the SPP shift. This concept is proved by taking the spectrum of the hole array along the vertical yellow dashed line (see Fig. 4.7a) such that a region of multi-layered MoS_2 is also sampled by the SPPs. The result shown in Fig. 4.7d reveals the SPP peak gradually shifts further to the red as the effective index (number of layers) increases for the MoS_2 on the array surface.

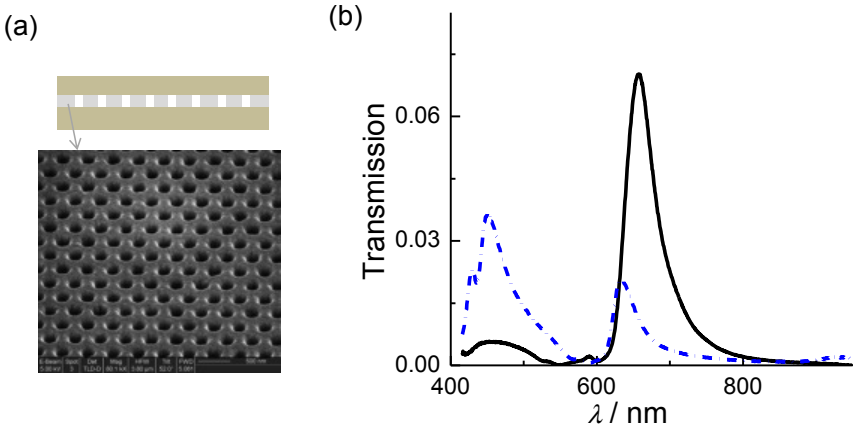

Figure 4.8: (a) The hexagonal hole array shown in the SEM image with period P = 420 nm and diameter D = 150 nm is milled in 250 nm thick silver film. The schematic picture shows the symmetric structure, in which the hole array is bonded with a 2 mm thick piece of PDMS. (b) Normal incidence transmission spectra of the hole array shown in (a) without (blue dashed curve) and with (black curve) bonding to the PDMS.

Fig. 4.8 demonstrates another example of the sensitivity of SPPs to the dielectric refractive index. A hexagonal symmetry hole array (P = 420 nm and D = 150 nm) is cladded with a PDMS substrate (with 1 mm thickness and refractive index 1.46 in the visible range). Note that there is no chrome film at the bottom. The PDMS overlayer results in a near refractive index matching for the SPPs on the dielectric and substrate sides of the metal film (shown in Fig. 4.8a). Subsequent coupling of the SPPs mode on both sides of the silver film results in the transmission intensity of the glass mode $(1, 0)_g$ around 650 nm (black solid curve) being greatly enhanced (dashed blue curve).[116]

Staying with the normal incident light condition, the linear periodic dispersion of SPPs modes for a hole array is shown in Fig. 4.9. Here the ratio of the hole diameter to the period of hole array D/P was kept constant at 1/2. The SPPs resonance $(1, 0)_g$ varies linearly with the periodicity (see Fig. 4.9b), as expected from eqn. (4.4).

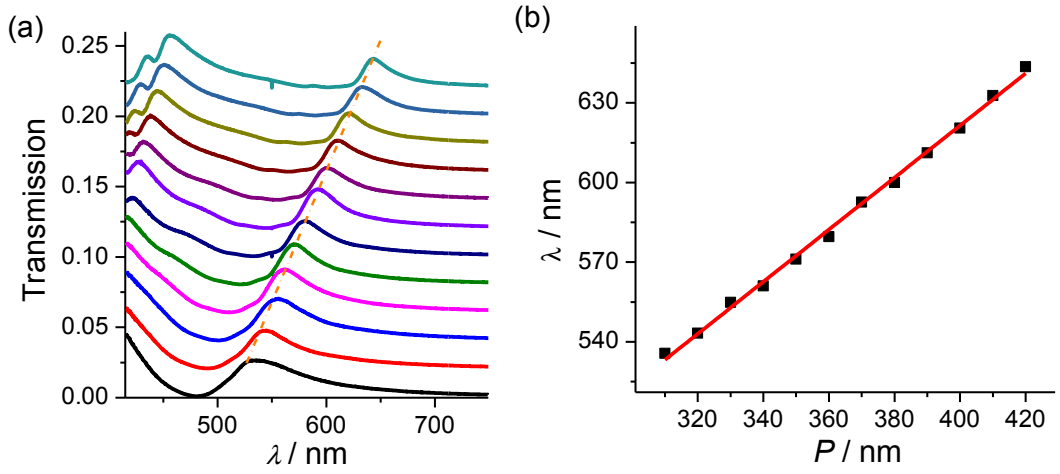

Figure 4.9: (a) The normal incidence transmission spectra of hexagonal hole arrays with period P = 310 nm to 420 nm. The yellow dashed line marked the peaks of the $(1,0)_g$ modes. (b) The wavelength of the $(1,0)_g$ SPPs resonance as a function together with linear fit ($\lambda = 229.3+1.0P$).

The factor C of eqn. (4.4) tells about the degeneracy of the SPPs modes supported by hole arrays at normal incidence. For instance there are four degenerate modes in the case of a square hole array: (1, 0), (-1, 0), (0, 1), and (0, -1). They have the same energy but propagate in different directions (demonstrated in Fig. 4.10a). For the hexagonal case (Fig. 4.10b), each resonance is contributed by six degenerate modes: (1, 0), (-1, 0), (0, 1), (0, -1) (1, -1), and (-1, 1). Therefore, the transmission enhancement of hexagonal holes

array is qualitatively larger than the instance of square one. This is shown in Fig. 4.11, displaying that the normalized-to-area transmittance of hexagonal hole array is ~ 2.2 times that of the square case at the same resonance (around 700 nm), even though the hole density of square array is a little larger than (~1.05 times) that of hexagonal array. This phenomenon invites us to consider the effect of symmetry on strong coupling efficiency, which will be investigated in Section 4.2. Additionally, from eqns. (4.3) and (4.5) the degeneracy can be broken by tilting the hole array sample and from the angular dispersion curves, the different surface plasmon bands (i, j) are distinguished very well except (see for example Fig. 4.23e).

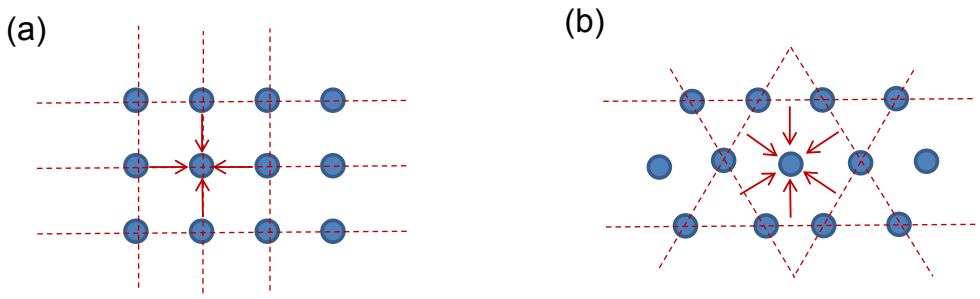

Figure 4.10: The degenerated SPPs modes created by the grating (dashed line) in the case of square (a) and hexagonal hole array (b).

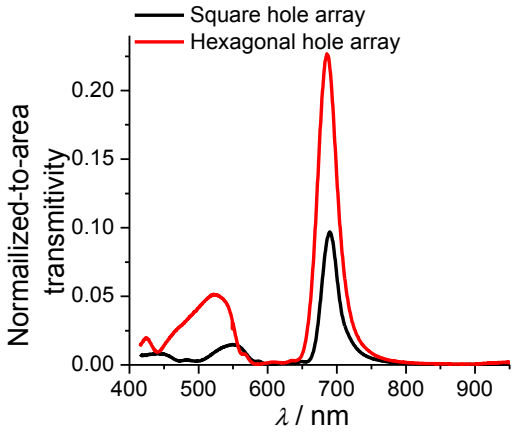

Figure 4.11: The normal incidence transmission spectra of hexagonal hole array with P = 430 nm (red curve) and square hole array with P = 390 nm (black curve). The diameter of holes in both cases is 140 nm. The hole arrays are milled in 250 nm thick silver film.

Besides hole arrays, other structures also can be good candidates for enhancing light-matter interactions. One is a single slit surrounded by periodic grooves and another is the bull's eye structure.[117-119] In both structures, the center slit or hole can play the role of "hot spot" which collects the SPPs which propagate towards it.[120-122] The resonance condition can be approximated by

$$\lambda_{SP} \propto P\sqrt{\frac{\varepsilon_d \varepsilon_m}{\varepsilon_d + \varepsilon_m}} \tag{4.6}$$

The linear periodic dispersion of both structures is demonstrated by Figs. 4.12-4.13. For the slit case, the width of grooves and the center slit are fixed at 100 nm and 250 nm respectively, and the distance between the center slit and the nearest grooves is equal to the periodicity of grooves. The spectra were taken using TM polarized light (in which case incident probe is normal to the surface and polarized perpendicular to the long axis of the grooves). However for the case of bull's eye, it is not necessary to use polarized light to excite SPPs because of the hole's circular symmetry. The ratio of the diameter D of the center hole to the period P of bull's eye is kept fixed at 1/2 so that the transmittance of structures with different periodicity is nearly the same, unlike the case for the groove structures where the D/P ratio decreases (Fig. 4.12).

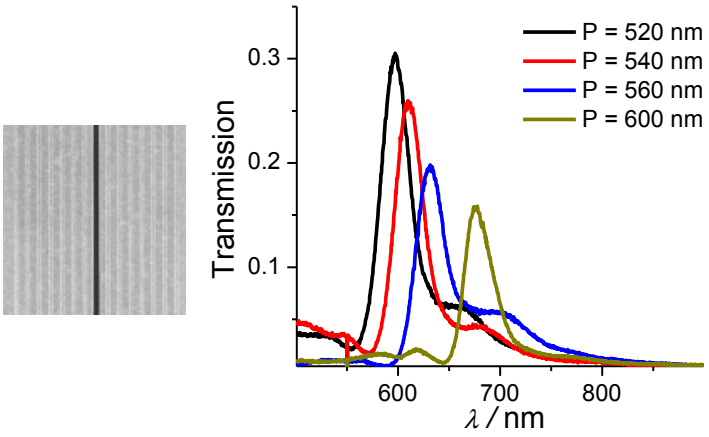

Figure 4.12: Normal incidence transmission spectra of a single slit surrounded by periodic grooves. The width of the grooves and center slit are kept constant at 100 nm and 250 nm respectively, and the distance between the center slit and the nearest grooves is equal to the period P of grooves. The structures are milled in 160 nm thick gold film.

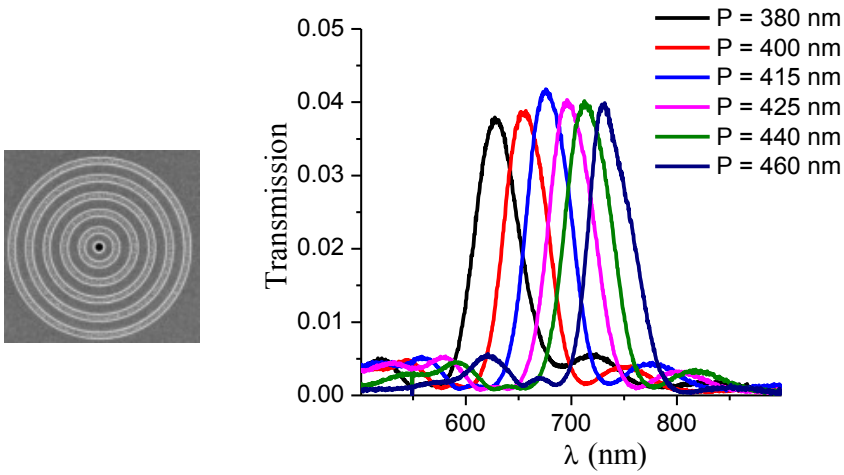

Figure 4.13: Normal incidence transmission spectra of bull's eyes: single holes surrounded by periodic, circular grooves. The ratio of the diameter of the center hole to the width of the grooves and to the period of grooves is kept constant at 1/2 and 1/3 respectively. The distance between the center hole and the nearest groove is equal to the period *P* of grooves. The structures are milled in 250 nm thick silver film.

4.2 Strong light-molecule coupling on plasmonic arrays of different symmetry

The previous section we saw that the same SPP resonance launched by square hole array and hexagonal array has different degeneracy in the normal incidence condition. The degeneracy should have consequences for the coupling strength between SPPs and molecules. Here the strong coupling on plasmonic arrays of different symmetry is investigated.[58]

4.2.1 Experimental methods

Sub-wavelength hole arrays were milled by focused ion beam (FEI Dual Strata 235) in sputtered silver films of 260 nm thickness on glass substrates. The hole diameter was kept constant at 150 nm as the array period was varied. Layers of J-aggregates of 4,4′,4″,4‴-(porphine-5,10,15,20-tetrayl)tetrakis(benzenesulfonic acid) tetrasodium salt hydrate, H_2TPPS^{4-}, (Aldrich) and of the polycation poly(diallyldimethylammonium

chloride), PDDA solution (average M_w 200,000-350,000, 20 wt. % in water, Aldrich), were alternately adsorbed onto 1 mm thick PDMS slabs using layer-by-layer (LBL) assembly. Polyelectrolyte layers were deposited by soaking the PDMS slab for 10 minutes in a solution of PDDA (8×10^{-2} M) and NaCl (0.7 M) in deionized water. J-aggregate layers were deposited by soaking the PDMS slab for 10 minutes in a solution of H_2TPPS^{4-} (1×10^{-4} M) in H_2O, which had been previously sonicated for 5 minutes and then adjusted to have a pH of 1.5 using HCl, promoting J-aggregate formation. The polyelectrolyte was deposited first and between each subsequent layer deposition the substrate was rinsed with water (pH = 1.5) and dried with nitrogen. To avoid two surfaces of PDMS being exposed to solution, one face of the PDMS slab was bonded to a glass substrate. The amount of J-aggregate deposited in each bi-layer depends on the acidity of the J-aggregate solution between solution pH = 1.0 and pH = 2.0, affording another control for the final absorbance of the layer.

4.2.2 Results and discussion

Fig. 4.14a shows the schematic of the hybrid organic/inorganic structure we chose for this study. A film of H_2TPPS^{4-}, which forms J-aggregates in acidic conditions (H_4TPPS^{2-}), is adsorbed on a nanostructured silver film (260 nm thick) which supports SP modes. The porphyrin J-aggregates typically have a rod-like shape with lengths in the micrometer range consisting of thousands of molecules.[123] In a previous study[80], J-aggregated H_4TPPS^{2-} in PVA (poly-vinyl alcohol) was deposited on nanostructured silver films by spin-casting, but here we chose to use LBL electrostatic deposition[124] to confine the molecules in the highest field amplitude near the surface and to avoid any deleterious chemical effects on the Ag film. Several bi-layers of H_4TPPS^{2-}/PDDA were absorbed on 1 mm thick PDMS slabs (see Experimental Methods for details). The slab of PDMS with the molecular film was dried using a stream of nitrogen and then gently bonded to the Ag surface (Fig. 4.14a).

Absorption spectra of the J-aggregate films on PDMS as a function of H_4TPPS^{2-}/PDDA bi-layer number are shown in Fig. 4.14b. Each bi-layer is typically 3-5 nm thick.[125, 126] The films exhibit two well-defined absorption bands in the visible region at

706 nm (1.76 eV) and at 491 nm (2.53 eV), with full width at half maximum (FWHM) of 56 nm and 29 nm respectively. The measured absorbance at the J-aggregate bands per bi-layer adsorbed to the PDMS slab was very sensitive to experimental conditions and varied from one run to another, however for any single series of adsorptions, the J-aggregate absorption increased linearly with the numbers of bi-layers (inset, Fig. 4.14b). These high optical density films with well-defined absorptions are perfect for studying strong interactions with plasmonic substrates.

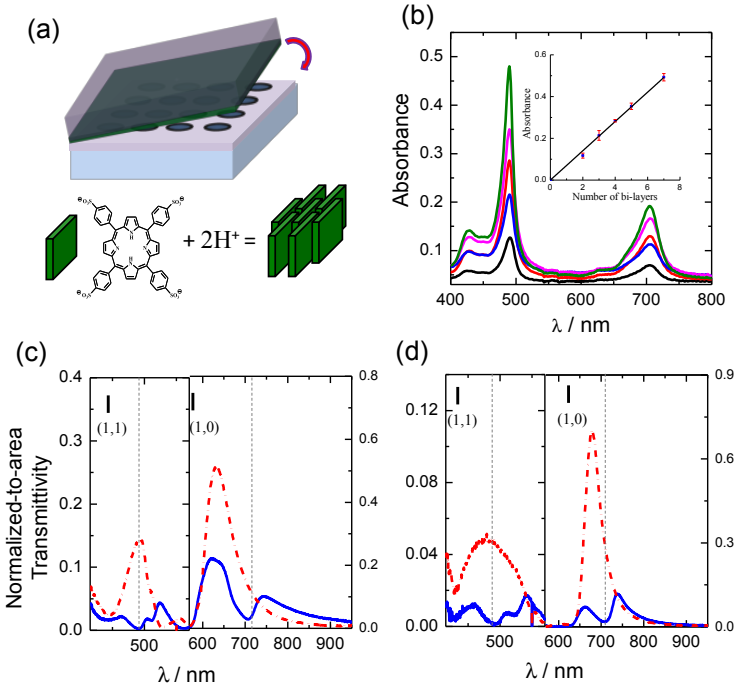

Figure 4.14: (a) Schematic sub-wavelength hole array milled in a silver film on a glass substrate upon which is adsorbed J-aggregated H_4TPPS^{2-}/PDDA bi-layers grown on a slab of PDMS. The structure of H_2TPPS^{4-} and the promotion of its J-aggregation by acidity is indicated. (b) Absorption spectra of two, three, four, five, and seven J-aggregated H_4TPPS^{2-}/PDDA bi-layers deposited on PDMS. The peak positions of the J-aggregate absorptions are at 706 nm (1.76 eV) and 491 nm (2.53 eV) respectively. Inset: absorbance at 491 nm vs. J-aggregate/PDDA bi-layer adsorption on PDMS. (c) Normal incidence transmission of a square hole array (P = 330 nm) when bonded to a 1 mm thick PDMS slab (red curve) and when bonded to a PDMS slab with J-aggregated H_4TPPS^{2-}/PDDA bi-layers with absorbance 0.898 at 491 nm (blue curve). (d) Normal incidence transmission of a hexagonal hole array (P = 430 nm) when bonded to a 1 mm thick PDMS slab (red curve) and when bonded to a PDMS slab with J-aggregated H_4TPPS^{2-}/PDDA bi-layers with absorbance 0.898 at 491 nm adsorbed (blue curve). In Figs. c and d the vertical scale is expanded to show clearly the interaction of the (1,1) SP mode with the 491 nm J-aggregate transition, the dashed vertical lines indicate the J-aggregate transition energies, and the short, solid vertical marks indicate the wavelengths of the SP modes estimated from Eq. (4.4) in section 4.1 by the indices (i, j). Figure is from reference[58].

Eqn. (4.4) in section 4.1 shows that changing the symmetry of the nanostructure provides a further tool for the systematic study of the interaction of molecular excited states with SP modes of different grating orders as shown in Fig. 4.10, and varying levels of degeneracy as will be discussed further below.

The red curves in Figs. 4.14c and 4.14d show the transmission spectra through square and hexagonal arrays respectively when a slab of PDMS is adsorbed to the array surface (no J-aggregates present). The two transmission peaks are due to SP modes propagating at the second and the third Brillouin zone (BZ) respectively. The effect of PDMS adsorption compared to a metal/air interface is a strong enhancement of the lowest energy mode (noted (1,0) here) and broadening of the next highest energy mode (noted (1,1) here) due to the presence of SPPs on the upper and lower surfaces of the hole array (the refractive index of bulk PDMS and the glass substrate are 1.46 and 1.47 respectively at 633 nm, see also the result of Fig.4.8). The periods of the arrays were chosen such that the (1,1) SP modes of the array were resonant with the 491 nm absorption band of the J-aggregate. Owing to the smaller lattice angle of hexagonal hole array, its (1,0) mode is then coincidentally also resonant with the 706 nm absorption of the J-aggregate.

The blue curves in Figs. 4.14c and 4.14d show the transmission spectra through square and hexagonal arrays respectively when a slab of PDMS/J-aggregate film was bonded to the surface of the arrays (absorbance of J-aggregate film was 0.898 at 491 nm). The splitting of the (1,1) mode due to interaction with the J-aggregate band at 491 nm is magnified for clarity. Note that the molecules interact mainly with the modes on the PDMS side. For the square array, the Rabi splitting of the (1,1) SP mode, 0.30 eV, is larger than the FWHM of the corresponding (1,1) mode, 0.19 eV. However for the hexagonal array the Rabi splitting (0.42 eV) is actually slightly smaller than the FWHM of the bare mode (ca. 0.51 eV). Nevertheless as shown below, all the other data (dispersion curves, concentration dependence, etc) demonstrates that the strong coupling regime is reached. In addition the dip in the transmission spectrum is not solely the negative of the molecular absorption. This suggests that the SP (1,1) mode broadened by the coupling to the SP mode from the opposite interface is not a good reference for judging the strongly coupled regime. It can be noted that the single side mode is much narrower with a FWHM of 0.29 eV (e.g. see Fig. 4.8).

In Figs. 4.15 and 4.16, the period dispersion at normal incidence is shown for two different coupling strengths wherein the adsorbed J-aggregate film absorbance at 491 nm was 0.460 (Figs. 4.15a and 4.16a) or 0.898 (Figs. 4.15c and 4.16c). The very large Rabi splitting observed for the interaction between the J-aggregate absorption at 491 nm and the (1,1) SP mode observed is due primarily to the higher molecular extinction coefficient of the J-aggregate at that wavelength, but may also benefit from higher confinement of the (1,1) SP modes as compared to the (1,0) SP mode. Concentrating the J-aggregate in a thin layer (< 50 nm[125, 126]) at the array surface where the plasmon field has the greatest amplitude also maximizes interaction compared to spreading the aggregates over hundreds of nanometers in a host polymer matrix on the array. For instance, for the same porphyrin J-aggregate dispersed in 150 nm of poly(vinyl) alcohol on a silver hexagonal array with absorbance at 491 nm of 0.49, a Rabi splitting of 200 meV was measured.[80] The layer-by-layer J-aggregate film here with absorbance of 0.460 at 491 nm gives a splitting of 312 meV.

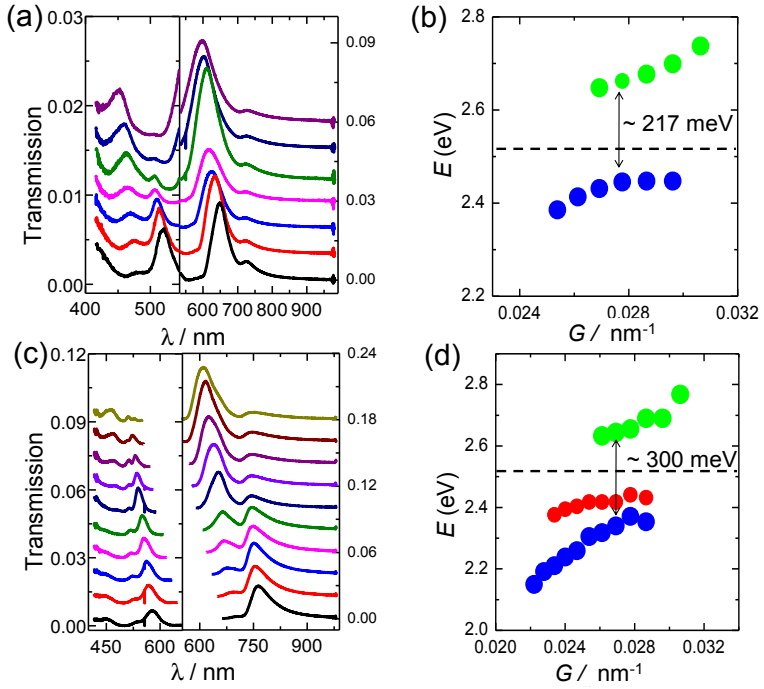

Figure 4.15: Square Arrays (a) Normal incidence transmission spectra of a set of square hole arrays (Periods from 310 nm to 400 nm as indicated by the arrow) with PDMS/J-aggregate film adsorbed (absorbance 0.460 at 491 nm). (b) Peak positions of the two peaks observed in the region 400-550 nm in a). The green and blue dots correspond to the upper and lower polariton bands respectively. The black dashed line is the J-aggregate 491 nm absorption energy. (c) Normal incidence transmission spectra of a set of square hole arrays (Periods from 310 nm to 400 nm as indicated by the arrow) with PDMS/J-aggregate film

adsorbed (absorbance 0.898 at 491 nm). (d) Peak positions of the two peaks observed in the region 400-550 nm in (c). The green and blue dots correspond to the upper and lower polariton bands respectively, while the red dots correspond to the new, less dispersive mode close to the molecular resonance. The black dashed line is the J-aggregate 491 nm absorption energy. Figure is from reference[58].

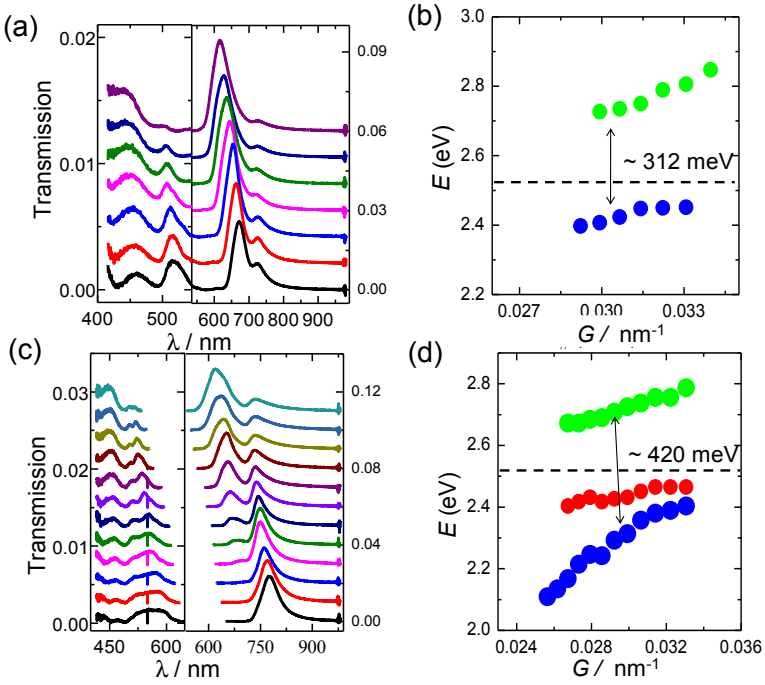

Figure 4.16: Hexagonal Arrays (a) Normal incidence transmission spectra of a set of hexagonal hole arrays (Periods from 380 nm to 490 nm as indicated by the arrow) with PDMS/J-aggregate film adsorbed (absorbance 0.460 at 491 nm). (b) Peak positions of the two peaks observed in the region 400-550 nm in (a). The green and blue dots correspond to the upper and lower polariton bands respectively. The black dashed line is the J-aggregate 491 nm absorption energy. (c) Normal incidence transmission spectra of a set of hexagonal hole arrays (Periods from 380 nm to 490 nm as indicated by the arrow) with PDMS/J-aggregate film adsorbed (absorbance 0.898 at 491 nm). (d) Peak positions of the two peaks observed in the region 400-550 nm in (c). The green and blue dots correspond to the upper and lower polariton bands respectively, while the red dots correspond to the new, less dispersive mode close to the molecular resonance. The black dashed line is the J-aggregate 491 nm absorption energy. Figure is from reference[58].

One of the important results of the optimization of strong coupling on these hole arrays is the observation of a new, weakly-dispersive transmission mode associated with the hybridization process and which appears both for the square and hexagonal arrays when the J-aggregate density is largest. This is shown in the dispersion curves in Figs. 4.15 and 4.16. The peak lies between the upper and lower cavity polariton bands, slightly red-shifted from the maximum of the J-aggregate absorption (see red dots, Figs. 4.15d and 4.16d). The band remains weakly dispersive even at high momenta (high observation

angles/array periods), where the upper and lower cavity polariton bands disperse strongly. The peak vanishes at lower molecular densities independent of the absolute value of the Rabi splitting (compare Figs. 4.15b and d, 4.16b and d). This new feature of molecule-surface plasmon strong coupling on nanostructured arrays was predicted theoretically very recently and attributed to a long range energy transfer between J-aggregates, mediated by SPPs.[127] We have also observed weakly-dispersive transmission modes associated with molecular absorption bands when adsorbing a dense layer of J-aggregates within 30 nm of a nanostructured metal surface.[128] These systems are very different but the origin could be the same, a question which demands further exploration.

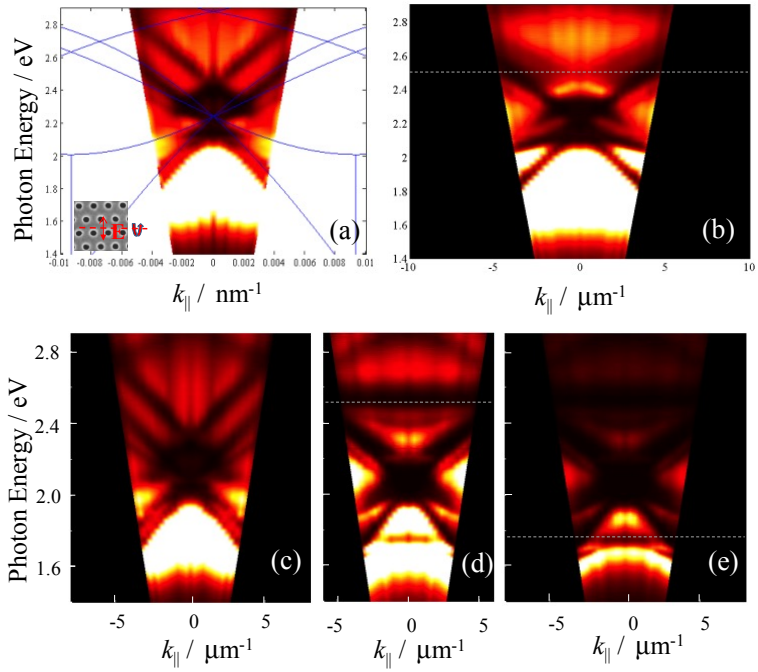

Figure 4.17: Transmission of p-polarized light through hexagonal arrays (intensity scale, white = high transmission, black = low transmission) as a function of in-plane photon momentum. The spectra were collected for positive angles only and the symmetrical representation is for clarity. (a) A silver hexagonal hole array, Period 420 nm, with a PDMS slab adsorbed. Inset is a SEM image of the hole array and indication of its rotation relative to incident light polarization. The blue lines are the theoretical dispersion calculated from Eqn. (4.3). (b) Angular dispersion for the same hexagonal array as in (a), but with a J-aggregate/PDMS slab adsorbed with absorption of 0.460 at 491 nm (2.53 eV, indicated by white dashed line). (c) A silver hexagonal hole array, Period 420 nm, with a PDMS slab adsorbed. (d) Angular dispersion for the same hexagonal array as in c), but with a J-aggregate/PDMS slab adsorbed with absorption of 0.898 at 491 nm (2.53 eV, indicated by white dashed line). (e) The same angular dispersion as in (d) but with contrast reduced to highlight dispersion around the 706 nm transition of the J-aggregate (1.76 eV, indicated by the white dashed line). Figure is from reference[58].

In the subsequent experiments, the same dispersion curves are shown as a function of angle for a single period array of hexagonal symmetry (Fig. 4.17). Fig. 4.17a shows the angular dispersion for a hexagonal array (period 420 nm) with a slab of PDMS adsorbed (no J-aggregate), while in Fig. 4.17b is shown the same array with a J-aggregate/PDMS slab adsorbed with absorption of 0.460 at 491 nm. The same comparison is made using a J-aggregate/PDMS slab with absorption of 0.898 at 491 nm in Figs. 4.17c-e. The dispersion of the SP modes is completely complementary to that observed for the periodic dispersion in Figs. 4.15 and 4.16. The new, non-dispersive mode observed at higher J-aggregate absorption clearly observed in Fig. 4.17d.

To understand the role of mode degeneracy on the Rabi splitting, we compared the J-aggregate absorption at 491 nm for the hexagonal and square arrays. Fig. 4.18c shows that for arrays of both symmetries, the degree of vacuum Rabi splitting has the well-known square root dependence on the absorbance of the material, which satisfies the expectation of theoretical eqns. (3.15) and (3.38) of Chapter 3. However, at any absorbance, the Rabi splitting is always much greater for the hexagonal array. This points to a hitherto little considered possibility- that the higher degeneracy of the plasmonic vacuum field can increase $\hbar\Omega_R$ in a similar way to the density of organic absorbers. Given the SP modes we have chosen in this study, the hexagonal array supports a 6-fold degeneracy, whilst the square array supports only a 4-fold degeneracy.

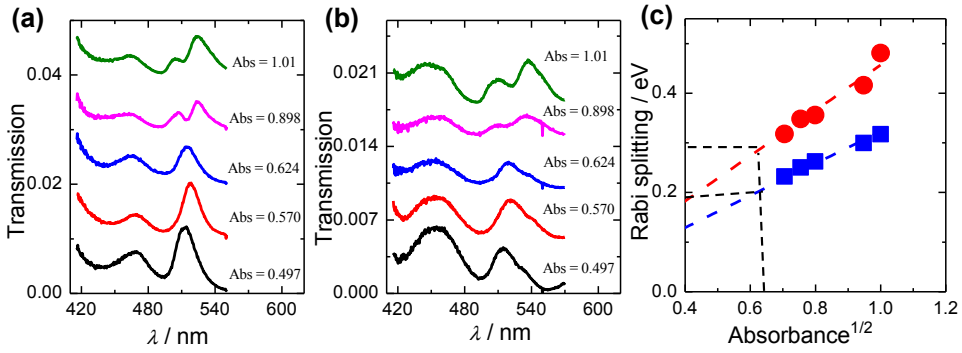

Figure 4.18: Normal incidence transmission spectra of square (a) and hexagonal (b) hole arrays upon increasing the adsorbed J-aggregate layer absorbance at 491 nm. At absorbance of 0.898 or higher, a new peak is observed between the two hybrid modes for both array symmetries. (c) Rabi splitting values as a function of the square root of the J-aggregate absorbance at 491 nm for both hexagonal (●) and square arrays (■). The dashed lines are linear fits (slopes 0.323 and 0.457 for square and hexagonal arrays respectively). Figure is from reference[58].

As presented in Chapter 3, the energies of the eigenstates P- and P+ in the absence of dissipation and detuning are given by

$$E = \frac{1}{2}(E_{SP} + E_{\mathrm{Ex}}) \pm \frac{1}{2}\sqrt{4g^2} \tag{4.7}$$

so that

$$\hbar\Omega_R = \sqrt{4g^2} \tag{4.8}$$

where g is the interaction coupling strength between the SP mode energy E_{SP} and the molecular transition energy E_{Ex}. Each SP mode of the same frequency, i.e. degenerate modes, will contribute to the coupling interaction. As a consequence, the Rabi splitting should depend on the SP mode degeneracy (n_d) as it contributes to the field amplitude

$$\hbar\Omega_R = \sqrt{4n_d g^2} \tag{4.9}$$

which shows that the ensemble of degenerated SP modes enhances the Rabi-splitting by $\sqrt{n_d}$. We therefore might expect that the ratio of the Rabi splitting of the hexagonal and square arrays is $\sqrt{\frac{6}{4}} = 1.22$. The ratio derived experimentally, 1.41, is in good qualitative agreement considering this simplified model derived from symmetry considerations alone.

Surface plasmon field intensities may also play a role in the different Rabi splittings observed for the square and hexagonal arrays. Optimal field amplitudes occur on hole arrays when the hole diameter matches half the array period.[129] The hole diameter for all the experiments was kept constant at 150 nm, in order to suppress low intensity transmission modes that result from SP coupling on each interface and which complicate band assignment. Thus, the field amplitudes are more optimal for the square array (P = 330 nm) than for the hexagonal array (P = 440 nm) and therefore cannot explain the greater Rabi splitting for hexagonal arrays. Independent of the particular conditions, we have noticed that for other dyes the Rabi splitting was always greater for the hexagonal array. The increase in degeneracy is akin to an increase in the density of optical states which should naturally increase the coupling strength.

4.3 Photoluminescence of strongly coupled systems on plasmonic arrays

In this section, the periodic dispersion of strongly coupled systems of SPPs and a standard fluorescence dye is investigated by reflection spectroscopy and its photoluminescence is studied in the Fourier space.

4.3.1 Experimental methods

To avoid the influence of substrate SP modes, dimple arrays are good candidates for the investigation of coupling of SPPs with adsorbed molecules. In this experiment, square dimple arrays were milled by FIB in sputtered silver films of 300 nm thickness on glass substrates. The depth and diameter of the dimples were both kept at 100 nm as the array period was varied. After that, the substrate was coated with polymer Su8 of 65 nm thickness doped with Cy3 ($C_{39}H_{45}ClN_2O_4$) dye molecules (see Fig. 4.19). Cy3 has a very high absorption coefficient, ~1.5 x10^5 L·mol^{-1}cm^{-1} in ethanol[130]. The dimple structures covered only with Su8 acted as a reference.

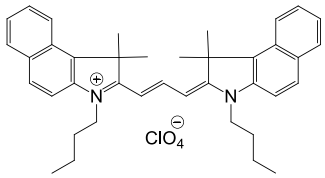

Figure 4.19: The molecular structure of Cy3 dye.

The SPPs of dimples and their coupling with Cy3 were analyzed by normal incidence reflection using standard optical microscope. The incident and reflected light passed through a low (0.13) N.A. objective lens (4× magnification) so that the reflection spectra were measured in a nearly collimated condition. In addition, the photoluminescence (PL) of the Cy3/dimple arrays were taken via the micro-spectroscopy setup shown in Fig. 4.20. In this setup, the light emitted from the nanostructures is collected by an objective lens (OL) and then momentum (angular) distribution of the

emission is analyzed in Fourier space. For simplicity, the part of white light microscope (used to locate the dimple arrays, and align the excitation beam) in this setup has been omitted.

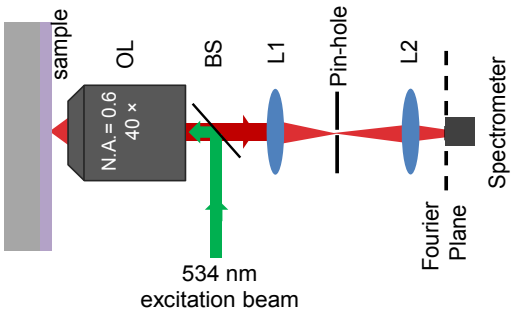

Figure 4.20: PL micro-spectroscopy setup. The sample is excited by 532 nm laser beam. The emission light is collected by an objective lens (OL), and then passes away a beam splitter (BS), a 4f system consisted by two lenses (L1 and L2) and arrives at the Fourier plane of L2, which also is the position of the slit of the spectrometer. The pinhole posted at the imaging plane of L1 is used to choose the area of the sample to probe.

4.3.2 Results and discussion

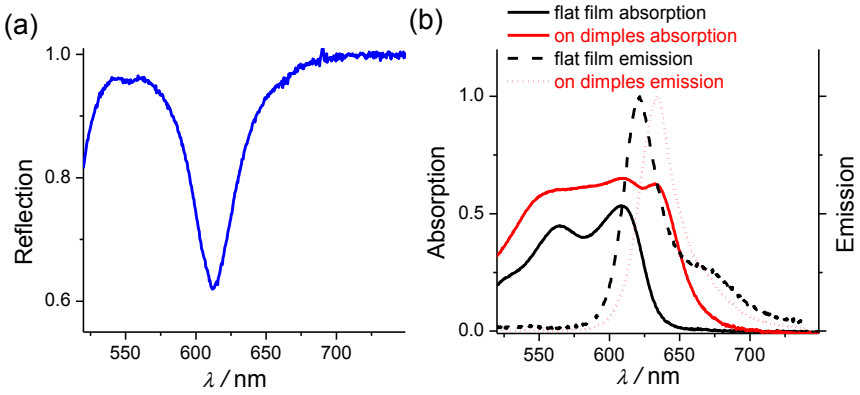

Figure 4.21: (a) Normal incidence reflection spectrum of a dimple array (P = 400 nm, D = 100 nm) coated with 65 nm polymer Su8. (b)The absorption (solid line) and emission spectrum (dotted line) of Cy3 dyes in Su8 on the flat silver film (black) or on the dimple array (red) of (a).

Fig. 4.21a shows the reflection spectrum (R %) of a dimple array (P = 400 nm) with 65 nm visible transparent polymer Su8 on top. The (1,0) surface plasmon mode of this dimple array is resonant at 613 nm (2.02 eV with a FWHM of 0.115 eV and a Q

factor of 20). As there is no transmission through the dimples, the absorption (*A* %) of the sample is simply equal to 1- *R* %. The red solid and dotted lines in Fig. 4.21b display the absorption and emission spectrum of the dimple arrays coated with same thickness of Su8 but doped with Cy3 dye molecules on top (1% weight ratio of Cy3 in the diluted solution of 2000.5 Su8). The black lines correspond to that of the molecular layer on a flat part of the silver film, in which there are double absorption peaks at 564 nm (2.20 eV with a FWHM of 0.145 eV) and 608 nm (2.04 eV with a FWHM of 0.109 eV) corresponding to Cy3 dyes' two different vibronic transitions. The absorbance of molecular layer at 608 nm and 564 nm are 0.15 and 0.12 respectively. These two peaks turns to three observable ones after coupling with the (1,0) surface plasmon mode of dimple array (see the red solid line of Fig. 4.21b). Especially the left peak around 550 nm is broadened and there is a new peak appearing at 638 nm. Moreover, the main emission peak of the Cy3 dyes on flat Ag film has a Stokesshift of 12 nm, but for the case of molecules on the dimple array, the emission peak coincides exactly with the lowest absorption peak. All these observations suggest that the coupling between the SPPs and Cy3 dyes result in totally different absorption and emission spectra from their original ones.

The further studies of strong coupling between the SPPs and Cy3 dyes are proved by periodical and PL dispersion spectra in Figs. 4.22-24. The nearly normal incidence reflection (with associated solid angle 7.5°) and emission spectra of the dimple array with varying periodicity from *P* = 330 nm (bottom) to 440 nm (top) are presented in Fig. 4.22. The dot-dashed lines in the spectra denote the same measurements for the Cy3 dye film on a flat part of the silver as a reference. The three new dips in the reflection spectra and the new emission peaks are summarized in terms of energy *vs* in-plane momentum in Fig. 4.23. The polariton dispersion extracted from the reflectivity minima in Fig. 4.22a can be fitted by a coupled three-oscillator Hamiltonian given by

$$\begin{bmatrix} E_{SPs} & V_1 & V_2 \\ V_1 & E_1 & 0 \\ V_2 & 0 & E_2 \end{bmatrix} \begin{bmatrix} \alpha \\ \beta \\ \gamma \end{bmatrix} = \varepsilon \begin{bmatrix} \alpha \\ \beta \\ \gamma \end{bmatrix} \tag{4.10}$$

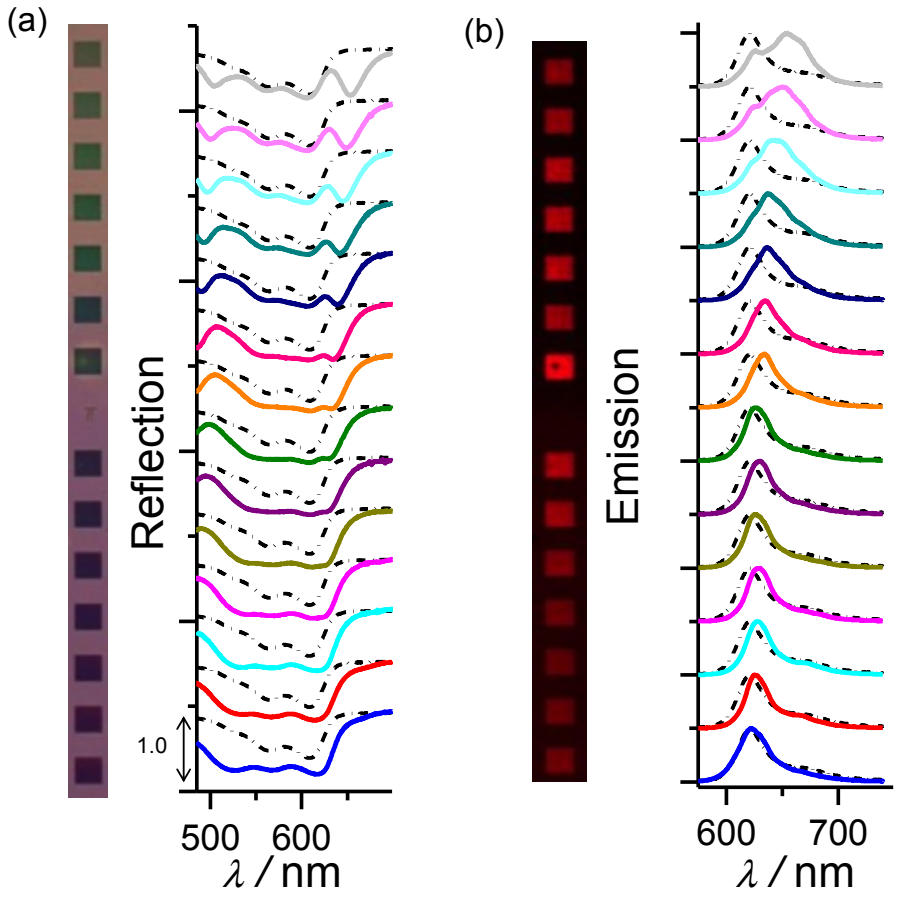

Figure 4.22: Normal incidence reflection (a) and emission (b) spectra of Cy3 dyes in Su8 on dimple arrays with periodicity varied from P = 310 nm (at the bottom) to 440 nm (at the top). The microscopic reflection and PL images of the sample are at the side of spectra. The dot-dashed lines in the spectra denote the results of molecular layer on the flat silver film.

where E_{SP} is the energy of surface plasmon mode, V_1 and V_2 are interaction potentials between the SPPs and two excited states of Cy3 dye with energy E_1 = 2.04 eV and E_2 = 2.20 eV, and ε are momentum dependent hybrid eigenvalues. From the experimental measurements, the periodic dispersion of the (1,0) surface plasmon mode of the dimple array with 65 nm bare Su8 polymer is $E_{SP}(G) = 0.884 + 0.489*G$, where G is equal to $2\pi/P$. V_1 and V_2 are equal to 170/2 meV, 190/2 meV respectively since the magnitude of the Rabi splitting is proportional to twice the interaction energy. Both the experimental data and the fitted curves demonstrate an obvious anti-crossing effect, resulting from the strong coupling between the SPPs and Cy3. Additionally, only P- emission (see Fig. 4.23b) is observable. It would be interesting to see if P+ will also emit at the cryogenic temperatures as it has been shown for inorganic compounds[15]. More discussion on this

point will be investigated in the following chapters on quantum yield and excitation spectroscopy.

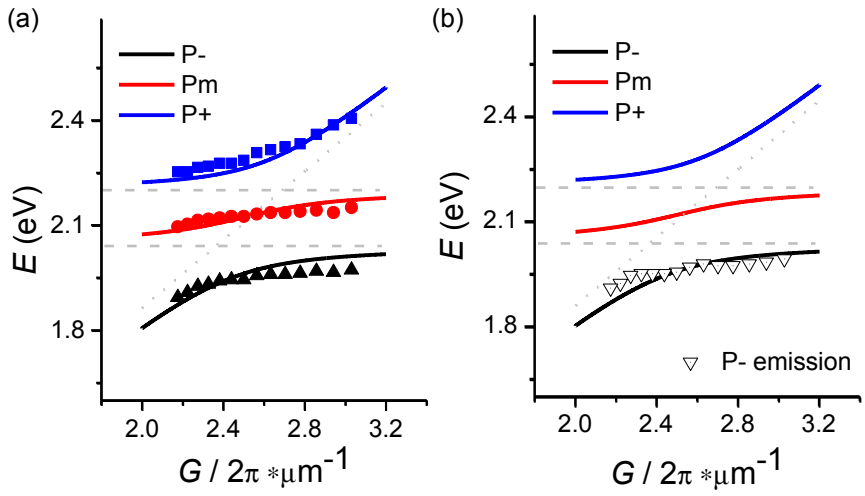

Figure 4.23: Polariton dispersion extracted from the reflectivity minima (a) and new emission peaks (b) in Fig. 4.21. As expected, three polariton branches (P+, Pm and P-) are observed in the reflection spectra of (a), in which the extracted new minima of the reflectivity (▲●■) denote the positions of the polariton branches, while the solid lines correspond to a coupled-oscillator modeling fit. For reference, the original SPPs dispersion curve (dotted line) and two absorption bands of Cy3 dyes (horizontal dashed lines) are also indicated. In (b), the new emission peaks only appear, and follow closely, the P- branch.

Figs. 4.24a-d gives the emission dispersion of Cy3 dyes in Su8 on dimple array with four different periodicities as collected in Fourier space. There are two branches in the spectra: one is associated with the dispersionless uncoupled emission at 2.00 eV and the other at lower energies is the emission following the dispersive P- band, as illustrated in Fig. 4.23b. From Fig. 4.23a, the original SPPs band of the dimple array with P = 400 nm is resonant with the lowest absorption band of Cy3 dye (E_1, dashed white line) at 2.04 eV at the normal incidence condition, *viz* $k_{//} = 0$. This is confirmed in Fig. 4.24c where the highly dispersive emission becomes apparent in addition to the non-dispersive uncoupled emission following the dashed line. If the period is further increased to 440 nm as in Fig. 4.24d, the emission becomes convoluted with the pure SPPs band as can be seen by comparing with the Su8 reference in Fig. 4.24e. In other words, the emission of the sample in this condition looks like the emission of the bare molecules enhanced by the optical density of states of the SPP bands.

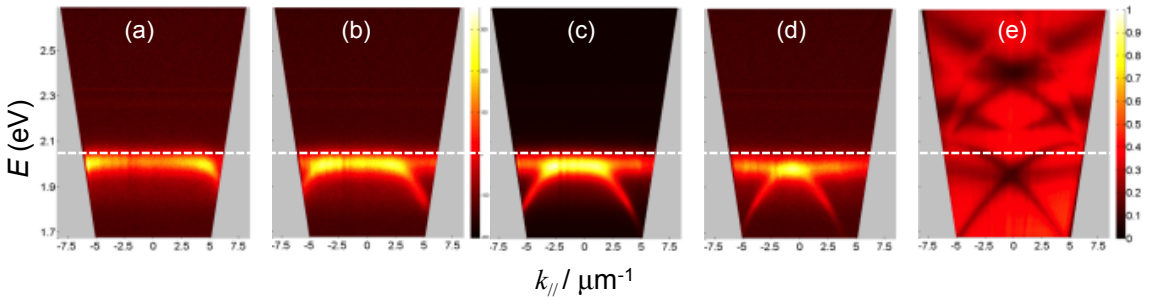

Figure 4.24: Emission dispersion of Cy3 dyes in Su8 on dimple arrays with periods P = 340 nm (a), 370 nm (b), 400 nm (c) and 440 nm (d). (e) Reflection dispersion of a neat Su8 film of 65 nm thickness on a dimple array with period P = 440 nm. The horizontal dashed line denotes the lowest absorption band of Cy3 dyes, E_1, at 2.04 eV. The color bar of (b) and (e) represent the emission intensity and reflectivity respectively. For clarity, it is noted that the symmetry of the dispersion bands shown in (a)-(e) do not correspond to the zero momentum, due to imperfect alignment of the PL micro-spectroscopy setup.

4.4 Conclusions

In this chapter we used a combination of layer-by-layer and elastomeric deposition techniques to adsorb a J-aggregate in thin layer directly at the surface of plasmonic arrays to maximize strong coupling. It was demonstrated that hybrid light/matter states with larger Rabi splitting could be achieved when using plasmonic nanostructures of higher symmetry, indicating that SP mode degeneracy is important for efficient coupling. A new weakly-dispersive transmission mode was observed in the gap which has been predicted theoretically to be associated with exciton-exciton hybridization. These findings point to new ways for optimizing strong coupling on plasmonic substrates, not only playing on molecular density, but also on photonic mode density.

In the last section we investigated the strong coupling of a plasmonic dimple arrays with the two transition bands of a cyanine dye by reflection and emission spectroscopy. The two observable emission bands at room temperature are related to the uncoupled molecular and P- polariton bands. The anti-crossing in the dispersion of the polaritonic modes was clear both in reflection and emission. In the next chapters, the issue of polariton lifetimes and emission quantum yields will be addressed to try to obtain better understanding of the photophysics of coupled systems.

5 Strong light-molecule coupling in micro-cavities

In the previous chapter surface plasmon polaritons were employed as optical resonances for strong light-molecule coupling. Plasmonic structures benefit from providing small mode volumes and high field enhancements. The half-open character of plasmonic structures is also more favorable in some experiments[72, 73] to avoid unnecessary interferences from closed optical systems. However, plasmonic structures made by focused ion beam (FIB) are typically limited to the micrometer size range for practical reasons and also optical characterization by micro-spectroscopy becomes more complex. Accordingly, another parallel optical structure, planar Fabry-Pérot (FP) optical micro-cavity, was also used in this thesis for study the dynamics of strongly coupled systems.

To begin, the physics of micro-cavities will be introduced in terms of multiple interferences. In addition, the energy-momentum dispersion of the cavity mode will be derived from the phase condition. Subsequently, the efficiency of light-matter strong coupling is tuned by precisely varying the spatial position of a thin layer of cyanine dye J-aggregates in FP micro-cavities and their photophysical properties are determined. These findings provide a deeper understanding of hybrid light-molecule states and have implications for the modification of molecular and material properties by strong coupling.

5.1 Physics of FP micro-cavity[1]

Let us consider an incident beam with a fixed wavevector traveling through a FP Micro-cavity, which is confined by two parallel and semi-transparent mirrors. For simplicity, the mirrors are considered to be infinitely thin and the optical response of the media in zones 1-3 are the same and lossless. Fig. 5.1 demonstrates the paths of light rays through the cavity: the primary beam is partially reflected and transmitted at the first mirror, and the transmitted part is subsequently reflected back and forth between the two mirrors. The division of the amplitude E_0 of the incident beam occurs in terms of E_0t, E_0tr, E_0tr^2, E_0tr^3, … inside the cavity, accordingly, E_0t^2, $E_0t^2r^2$, $E_0t^2r^4$… represent the transmitted rays. Here, r is the coefficient of reflection of mirror and t the transmission one. Taking the phase difference between successive transmitted rays into account as $e^{i\delta}$, the intensity of the transmitted light is derived from the interference of the multiple transmitted beams:

$$I_T = \left|E_T\right|^2 = \left|E_0t^2 + E_0t^2r^2e^{i\delta} + E_0t^2r^4e^{i2\delta} + ...\right|^2 = \frac{I_0\left|t\right|^4}{\left|1-r^2e^{i\delta}\right|^2} \tag{5.1}$$

where $I_0 = \left|E_0\right|^2$ is the intensity of the incident beam. If R denotes the reflectance and T the transmittance of the mirrors, then

$$I_T = \frac{I_0T^2}{\left|1-\mathrm{Re}^{i\delta}\right|^2} = I_0\frac{T^2}{(1-R)^2}\frac{1}{1+F\sin^2\frac{\delta}{2}} \tag{5.2}$$

The factor

$$F = \frac{4R}{(1-R)^2} \tag{5.3}$$

is well known as the coefficient of finesse of the cavity.

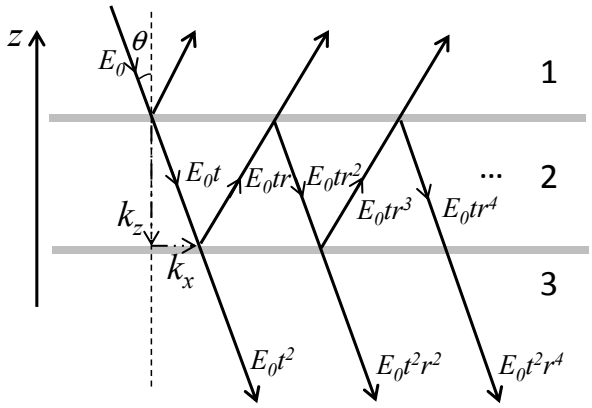

Figure 5.1: Schematic representation of paths of light beams undergoing multiple reflections in a FP micro-cavity confined by two infinitely thin mirrors.

The Airy function $\left[1+F\sin^2(\delta/2)\right]^{-1}$ in eqn. (5.2) thus strongly depends on the values of R as shown in Fig. 5.2. From the experimental view, the transmission peak is associated with the maximum of the Airy function. If the reflectance R is very small (i.e. few reflections inside the cavity) , so that F is small, the transmission peaks are broad and indistinct; whereas if R is near unity, resulting in large F and sharp transmission peaks with a high Q-factor. In the visible range, thin silver and aluminum films (20-30 nm) with high reflection coefficient (0.7-0.9) are favorable to form the cavities.

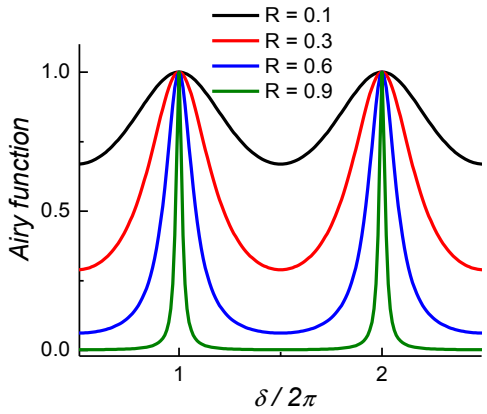

Figure 5.2: Airy function $\left[1+F\sin^2(\delta/2)\right]^{-1}$ curves with different values of reflectance R of mirror.

The condition for a transmission maximum is $\delta/2=\ell\pi$ (see Fig. 5.2), here ℓ is an integer and denoted as the order of the optical modes of the cavity. If only considering the geometric path difference between any two successive transmitted rays and the phase change $\delta_r/2$ in every associated reflection[63], δ can be written as

$$\delta = \frac{4\pi}{\lambda_0} nd\cos\theta + \delta_r \tag{5.4}$$

where n is the refractive index of the medium in the cavity, d is the cavity length, and θ is the incidental angle of the optical beam. Then the phase condition for the transmission peaks is equivalent to

$$\frac{2\pi}{\lambda_0} nd\cos\theta + \frac{\delta_r}{2} = \ell\pi \tag{5.5}$$

which reveals that the resonant wavelength of the cavity λ_0 blue shifts when the incident angle θ increases.

The eqn. (5.5) can be rewritten in terms of the wave vector

$$k_z d + \frac{\delta_r}{2} = \ell\pi \tag{5.6}$$

where k_z is the vertical component of the wave-vector of the optical beam in the cavity (shown in Fig. 5.1). If the phase change associated with reflection is neglected, namely in the case of $\delta_r = 0$, the quantization of the vertical wave-vector can be expressed as $k_z = \ell\pi/d$. Therefore, the angular dispersion of cavity modes can be approximately written as

$$E_c(k_x) = \frac{1240}{n \cdot 2\pi}\sqrt{{k_x}^2 + (\frac{\ell\pi}{d})^2} \tag{5.7}$$

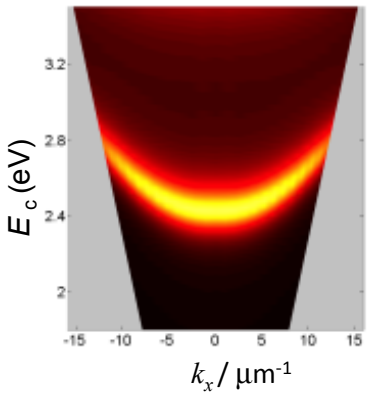

Figure 5.3: Energy-momentum dispersion of the 1st cavity mode of a metallic FP with parameters n = 1.5, d = 150 nm, and ℓ =1.

where k_x is the horizontal component of the wave-vector of the optical beam in the cavity and E_c is the energy of the cavity mode in electronvolts. Fig. 5.3 displays a parabolic energy-momentum dispersion of the 1st cavity mode with parameters n = 1.5, d = 150 nm, and ℓ =1.

5.2 Spatial tuning of strong coupling in micro-cavities

In this thesis, metallic FP micro-cavities are used for the study strong light-molecule coupling due to their easy fabrication and strong optical field enhancement within a small mode volume, and despite their low Q-factor (10-20). Strong coupling can be illustrated by placing J-aggregates of a cyanine (TDBC), having a maximum absorption at 588 nm (Fig. 5.4b), inside a resonant FP cavity as illustrated in Fig. 5.4c. As discussed in earlier chapters, the hybrid states P- and P+ are formed when energy is exchanged between the J-band of molecules and a resonant optical cavity mode at a rate faster than their respective de-phasing processes (see Fig. 5.4a). The transmission spectrum is strongly modified with two new peaks separated in this case by a Rabi splitting of 325 meV (Fig. 5.4c).

We have already seen that the Rabi splitting ($\hbar\Omega_R$) is proportional to the square root of the molecular concentration within the optical mode volume (V) as predicted by both classical and quantum theories of strong coupling (Chapter 3). The classical description of strong coupling, as well as the semi-classical[13] and quantum theories, predict further that the Rabi splitting ($\hbar\Omega_R$) should be a linear function of the EM field amplitude ($\vec{E}$), which has been seen by changing the degeneracy of surface plasmon in the previous chapter. Here, $\hbar\Omega_R$ will be spatially tuned by depositing a molecular layer in the different positions inside the FP microcavities.[60]

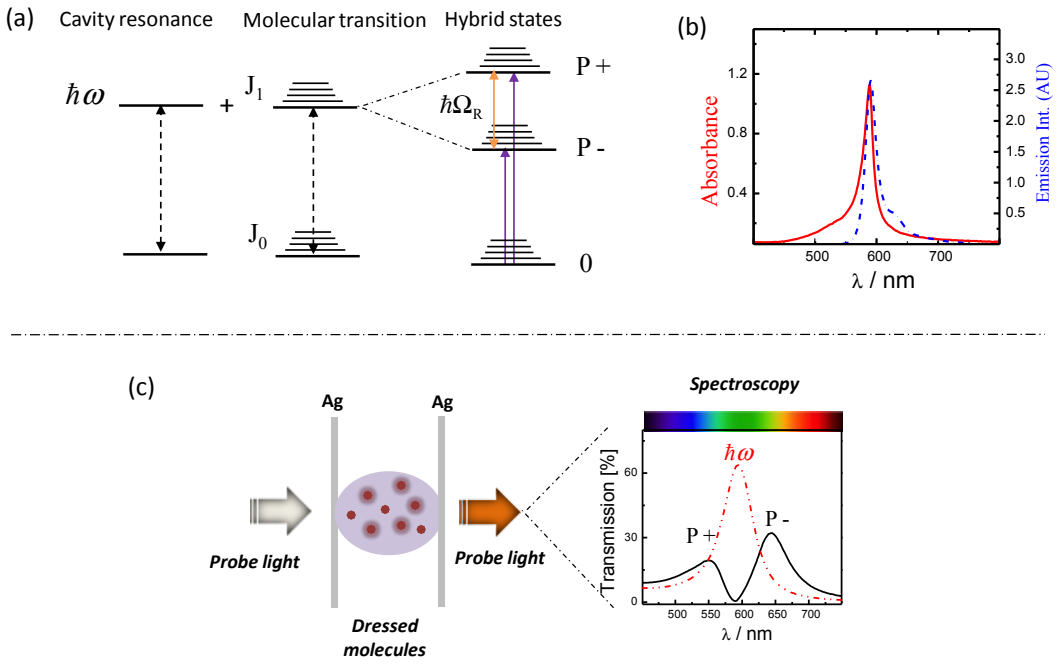

Figure 5.4: (a) Schematic representation of the coupling of a molecular transition (J_0-J_1) and an optical resonance of energy ($\hbar\omega$) forming the hybrid states P+ and P- separated by the Rabi splitting energy ($\hbar\Omega_R$). (b) Absorption (red solid line) and emission spectrum (blue dashed line) of J-aggregate layer of TDBC. (c) Schematic illustration of TDBC dispersed in the λ/2 Fabry-Perot (FP) cavity everywhere. Transmission spectra of the bare cavity (red) and in the presence of dispersed TDBC in resonance with the cavity giving rise to P+ and P-. Figure is from reference.[60]

5.2.1 Experimental methods

Sample fabrication: we developed a bonding technique for the precise control of the cyanine J-aggregate film's position in the FP micro-cavity. To begin, a 30 nm-thick silver film was sputtered on a glass substrate, upon which was spin-coated a film of poly(methyl methacrylate) (PMMA) of variable thickness (labeled slab A). Meanwhile, a 30 nm-thick silver film was evaporated on a 1.0 mm thick poly(dimethyl siloxane) (PDMS) substrate upon which was spin-coated a layer of PMMA of variable thickness (labeled slab B). The surface of the PMMA on slab A was made hydrophilic by spin-coating a ~2 nm thick PDMS layer on it (from 0.3 wt% in *tert*-butanol) and exposing it to an oxygen plasma for 30 seconds. Next, layers of J-aggregates of the cyanine TDBC (5,6-dichloro-2-[[5,6-dichloro-1-ethyl-3-(4-sulphobutyl)benzimidazol-2-ylidene]propenyl]-1-ethyl-3-(4-sulphobutyl) benzimidazolium hydroxide, inner salt, sodium salt, Few

Chemicals) and of the PDDA solution (average M_w 200,000-350,000, 20 wt. % in water, Aldrich) were alternately adsorbed onto the surface of slab A using LBL assembly.[124, 131] Polyelectrolyte layers were deposited by soaking slab A for 5 minutes in a solution of PDDA (6×10^{-2} M) in deionized water. J-aggregate layers were deposited by soaking slab A for 5 minutes in a solution of TDBC (1×10^{-4} M) in H_2O, which had been previously sonicated for 60 minutes at 35°C. The surface of slab B was coated with a ~2 nm thick film of PDMS. Finally, the polymer face of slab B was sealed to the molecular film surface of slab A to form a low quality (Q factor~12) optical micro-cavity. By controlling the thickness of the PMMA layers on slab A and slab B, the position of the J-aggregate layer could be placed near the edge of the cavity or at the centre of the cavity. The whole cavity length, including the PMMA and molecular films, could be tuned such that the J-aggregates absorption band at 588 nm was resonant with either the λ/2 or λ FP cavity mode. Film thicknesses were measured using Alpha-step IQ surface profilometer.

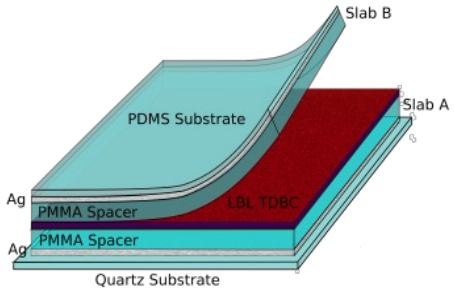

Figure 5.5: Schematic representation of the Ag-Ag micro-cavity sample. Figure is from reference.[60]

In Fig. 5.6, the transmission spectra of two cavity samples demonstrate that the Q-factor of bare cavity modes (without LBL TDBC) is 10-20. The order of cavity mode *l* ($1^{st}, 2^{nd}, 3^{rd}$...) can be found the ratio between the wavelengths of successive peak.

Steady-state spectroscopy: steady-state transmission and reflection spectra were taken on a Shimadzu UV3101 spectrometer. Steady-state fluorescence spectra were taken with a Horiba Jobin Yvon-Spex Fluorolog-3 fluorimeter.

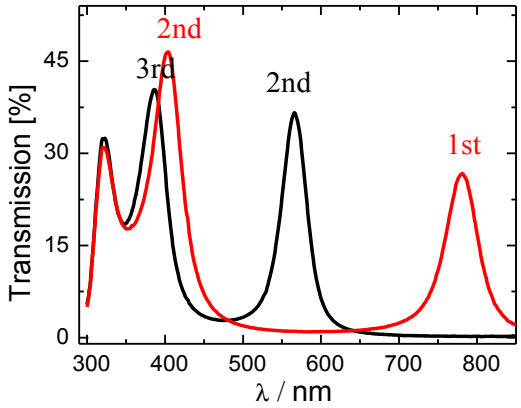

Figure 5.6: Transmission spectra of two cavity samples (demonstrated in Fig. 5.5 without LBL TDBC) prepared by bonding technique.

5.2.2 Results and discussion

As detailed in the experimental methods, we have developed a method to the precisely locate a highly absorbing, thin (~25 nm) film of a cyanine J-aggregate in a FP micro-cavity, varying its position in ~10 nm steps from the edge to the centre of the cavity (Fig. 5.7). This allows us to quantitatively analyze the strong coupling interaction strength as a function of molecular spatial position inside the cavity with much higher resolution than had been achieved previously for organic systems.[46] The spatial distribution of the optical field amplitude E in the cavity for the λ/2 and λ FP modes is indicated schematically in Fig. 5.7a and d respectively.

In Fig. 5.7b are shown transmission spectra for the λ/2 FP cavity in resonance with the J-aggregate, when the molecular film of the same absorbance as in Fig. 5.4b, is moved gradually from the edge of one of the silver mirrors to the centre of the cavity. The Rabi-splitting increases from 310 meV to 503 meV for this sequence (Fig. 5.7b), following the predicted spatial distribution of the optical field amplitude for the mode as simulated using Maxwell's equations (compare Figs. 5.7a and c). Indeed, the observed $\hbar\Omega_{VR}$ can be reproduced by inserting the complex refractive indices of the various cavity component layers into Maxwell's equations in the 'classical' limit and employing transfer matrix formalism (Fig. 5.7c).[71, 87]

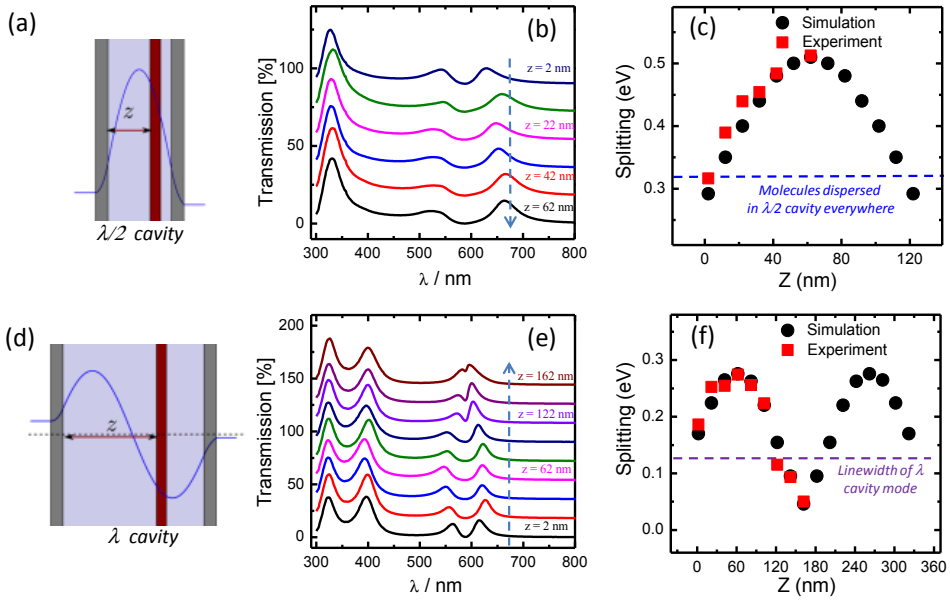

Figure 5.7: (a) Schematic representation of the *λ/2* cavity and the corresponding field amplitude. (b) Transmission spectra of a set of *λ/2* cavities resonant with a TDBC molecular layer located at different spatial positions inside the cavity (*z* from the edge to center as indicated by the dashed blue arrow and every offset of T% is 18%). These spectra were measured under 35˚ incidental angle and TE polarization. (c) Rabi splitting verses spatial position of the molecular layers inside the *λ/2* mode cavities (blue dashed line represents the $\hbar\Omega_{VR}$ when the molecules are dispersed evenly inside the cavity). (d) Schematic representation of the *λ* cavity and the corresponding field amplitude. (e) Normal incidence transmission spectra of a set of *λ* mode cavities with TDBC molecular layer and (f) their corresponding $\hbar\Omega_{VR}$ (red squares) at different spatial positions inside the cavity. The purple dashed line indicates the FWHM line-width of the *λ* mode (150 meV) as the minimum energy splitting below which strong coupling can no longer be defined. Black dots in (c) and (f) are the calculated splittings using the transfer matrix simulation where the complex refractive index of the TDBC J-aggregate film was extracted from its absorption spectrum via a Kramers-Kronig transformation and the thickness of the Ag mirrors and PMMA spacer layers were taken from experiments. Figure is from reference.[60]

When the J-aggregate film is at the centre of the λ/2 cavity (the field anti-node) the Rabi splitting is 1.54 times higher than if the same optical density of J-aggregate is dispersed throughout the whole cavity (dashed blue line, Fig. 5.7c). This is further confirmed by the anti-crossing angle-dependent dispersion properties of the cavity in which the molecular layer is positioned at the field maximum (Fig. 5.8b), which were measured by TE polarization light. An important point to note for coupling to the λ/2 FP mode is that even when the molecular layer is at the edge of the cavity (Fig. 5.8a), the system remains in the strong coupling regime (that is, $\hbar\Omega_{VR}$ is greater than the line-width of the λ/2 FP mode (210 meV) and the FWHM of the J-aggregate band at 588 nm (72

meV)). This is due to the fact that the molecular layer has finite width where the field is already significant (Fig. 5.7a).

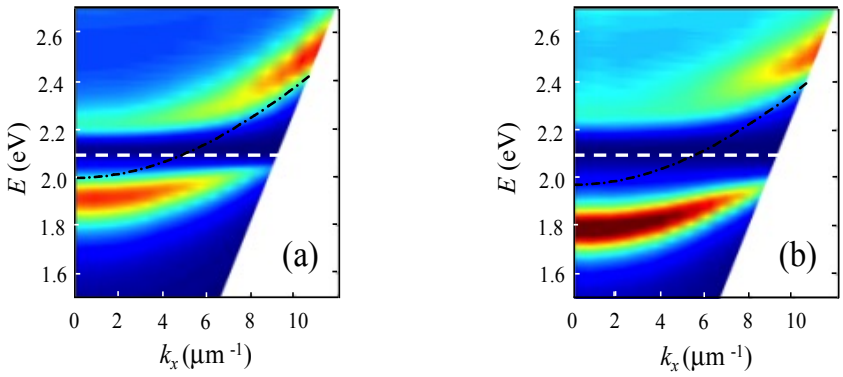

Figure 5.8: Angular-dependent dispersion of TDBC layer at the edge (a) or in the center (b) of the λ/2 cavity. The angle of TE polarization incidental light was measured from 0° to 65°. The black dot-dashed lines and white dashed line denote the dispersion of the empty cavity and bare TDBC layer respectively. Figure is from reference.[60]

In the next set of experiments we increased the thickness of the FP cavities to 350 nm, such that the λ FP cavity mode was resonant with the 588 nm absorption band of the J-aggregate (Figs. 5.7d-f). Again the 25 nm thick TDBC layer was moved from the centre of the cavity (z = 162 nm) to the edge (z = 2 nm). The observed Rabi splitting is at a maximum (280 meV) when the molecular film is at a quarter of the cavity (z = 62 nm), whereas it reduced to 190 meV for molecules at the edge of the cavity, and to just 40 meV when the molecules are at the centre. Again this corresponds to the expected spatial distribution of the λFP cavity mode amplitude and closely agrees with transfer matrix simulations. It is interesting to note that $\hbar\Omega_{VR}$ is about 1.58 higher for the λ/2 cavity than for the λcavity when the molecular layer is placed at field antinode of these cavities. This observation is in quantitative agreement with the dependence of the Rabi splitting on the mode volume as predicted by eqns. (3.23) and (3.28) ($\frac{\hbar\Omega_{VR}^{\lambda/2}}{\hbar\Omega_{VR}^{\lambda}} \propto \sqrt{\frac{V_{\lambda}}{V_{\lambda/2}}} = 1.60$), the two different mode volumes being estimated by the transfer matrix method.

The dashed blue line in Fig. 5.7f is the Rabi splitting energy threshold above which the system can be defined to be in the strong coupling regime (125 meV ± 25 meV). Thus by moving the position of the molecular layer from the quarter of the cavity to the

centre, the λ cavity can be tuned from weak to strong coupling regime which is very valuable for elucidating cavity effects as we present below.

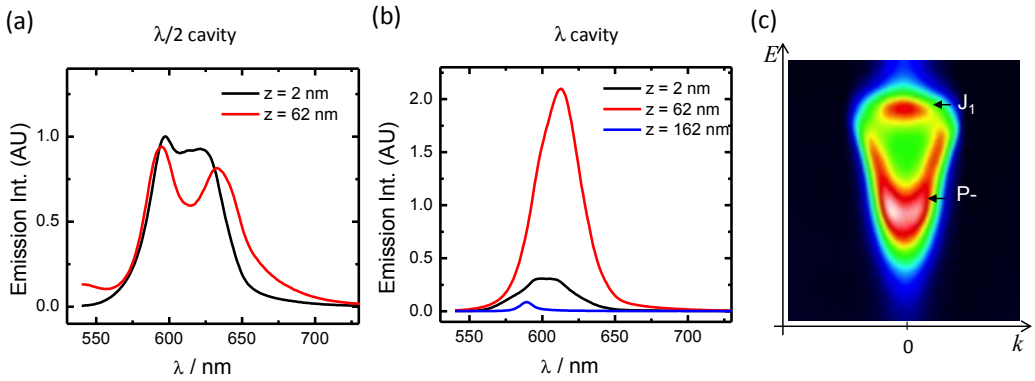

Figure 5.9: Fluorescence emission spectra (collected normal to the sample plane, excitation wavelength 520nm) of (a) λ/2 mode cavities with TDBC molecular layer in two different spatial positions of the cavity (z: 2 and 62 nm); (b) λ mode cavities with three different spatial positions of the cavity (z: 2, 62, 162 nm). The dashed vertical line in the spectra indicates the maximum of the fluorescence of J_1 of uncoupled J-aggregates. The peaks to the right are due to the fluorescence of P-. (c) An example of the dispersion of the P-fluorescence collected over k-space. Figure is from reference.[60]

Fig. 5.9 compares the emission spectra of the molecular film placed at the field nodes and anti-nodes in the λ/2 and λ cavities. Fluorescence spectra of such coupled systems typically exhibit two components- one corresponding to uncoupled molecules from J_1, and the other to P- state.[59, 132] Furthermore, emission from P+ is rarely observed which is attributed to rapid non-radiative decay to the lower energy levels at room temperature.[132, 133] This is certainly the case here for the λ/2 cavity, where emission peaks from both uncoupled molecules and P- can be observed whether the J-aggregate film is placed at the centre (anti-node) or at the edge (node) of the cavity (Fig. 5.9a). Note that, as expected, the P- emission moves to longer wavelengths with the higher coupling strength at the anti-node (z = 62 nm).

In the case of the λ cavity, only the fluorescence from the uncoupled excited state J_1 is observed (blue curve, Fig. 5.7b) when the J-aggregate film is placed at the center of the cavity (the central node, z = 162 nm). In contrast, the polariton emission dominates (red curve, Fig. 5.7b) when the molecular films is at the anti-node of the cavity (z = 62 nm). Finally at the edge of the λ cavity (z = 2 nm), the emission from both states overlap.

5.3 Emission quantum yield and lifetime of cavity polariton

In the previous section, we showed that the Rabi splitting is at a maximum when molecules are placed at the anti-nodes of the optical field modes where ***E*** is strongest, and this should be optimal for the smallest mode volume *V*. Here we investigate further fundamental aspects of light-molecule strong coupling, such as the quantum yield of polariton emission. To our knowledge this has never been reported before despite having important implications for the decay mechanism of the coupled state. We study these features as function of the Rabi splitting and the location of the molecules relative to the optical mode (illustrated in Figs. 5.7a and d). [60]

5.3.1 Experimental methods

Quantum yield measurements: in order to assess the fluorescence quantum yield of strongly coupled TDBC, we performed a relative measurement as detailed in reference.[134] This standard approach is to compare the emission of the sample to that of a reference of known absolute quantum yield, correcting for the fraction of light absorbed by each sample. One writes

$$\Phi_s = \Phi_r \cdot \frac{I_s}{f_s(\lambda_{ex})} \frac{f_r(\lambda_{ex})}{I_r} \frac{n_s^2(\lambda_{em})}{n_r^2(\lambda_{em})} \tag{5.8}$$

where Φ_s (Φ_r) is the quantum yield of the sample (reference), I_s (I_r) is the integrated emission intensity of the sample (reference) when pumped at λ_{ex}, $f_s(\lambda_{ex})$ ($f_r(\lambda_{ex})$) is the absorption fraction at this same pumping wavelength and $n_s^2(\lambda_{em})$ ($n_r^2(\lambda_{em})$) is the refractive index of the sample (reference) environment at the average emission wavelength. The protocol proposed here is composed of three steps. First, we measured the absolute quantum yield of a standard dye (Lumogen Red, LR) in a chloroform solution using a commercial integrating sphere (Hamamatsu C11347-11). This value was then

used as a reference for computing the quantum yield of a thin polymer film containing the same standard dye, using eqn. (5.8). Finally, we obtained the quantum yield of strongly coupled TDBC by comparison to this new reference quantum yield using the same equation. Absorption of the samples (shown in Fig. 5.10a) were measured using Shimadzu UV3101 spectrometer at 520 nm (the excitation wavelength). In the case of strongly coupled TDBC, this corresponds to non-resonant excitation of the polaritons but the same values were obtained by exciting at 550 nm (resonant with P+). The fluorescence spectra (Fig. 5.10b) were recorded using a Fluorolog-3 fluorimeter and the emission intensities were integrated over the emission band. For strongly coupled TDBC, we only integrated the emission spectrum over P- region as the P+ state is not radiative in our conditions. It should be noted that since our Fluorolog emission spectrometer has a small numerical aperture of detection, it only collects P- emission over a small range of angles around the bottom of its dispersion branch. By performing angle-resolved photoluminescence measurements on P- (shown in Figs. 5.9c and 5.10c), we took into account the anisotropy of the emission

Time-Resolved Measurements: narrow band (linewidth = 6 nm), 150-fs-pulses centered at 585 nm were used for transient absorption spectroscopy measurements. The spectra were recorded using low-energy (<100 $\mu J/cm^2$) pump pulses to avoid spurious effects and exciton-exciton annihination in the TDBC J-aggregates. The principle details of the pump-probe spectroscopy experiment will be introduced in the following chapter.

5.3.2 Results and discussion

The fluorescence quantum yield (Φ_f) gives insight into the relaxation pathways in strongly coupled molecular systems since

$$\Phi_f = \frac{k_r}{k_r + k_{nr}} = \tau \cdot k_r \qquad (5.9)$$

where k_r and k_{nr} are the radiative and non-radiative decay rates and τ the lifetime of the emitting state. We measured the Φ_f values of the coupled system and that of a bare TDBC film outside the cavity. The $\Phi_f(J_1)$ of the bare film was found to be 0.02. Since the cavity emission properties are dispersive (angle dependent) as shown in Fig. 5.9c, the

measurement of Φ_f of P- requires careful integration over all angles as described in the method section.

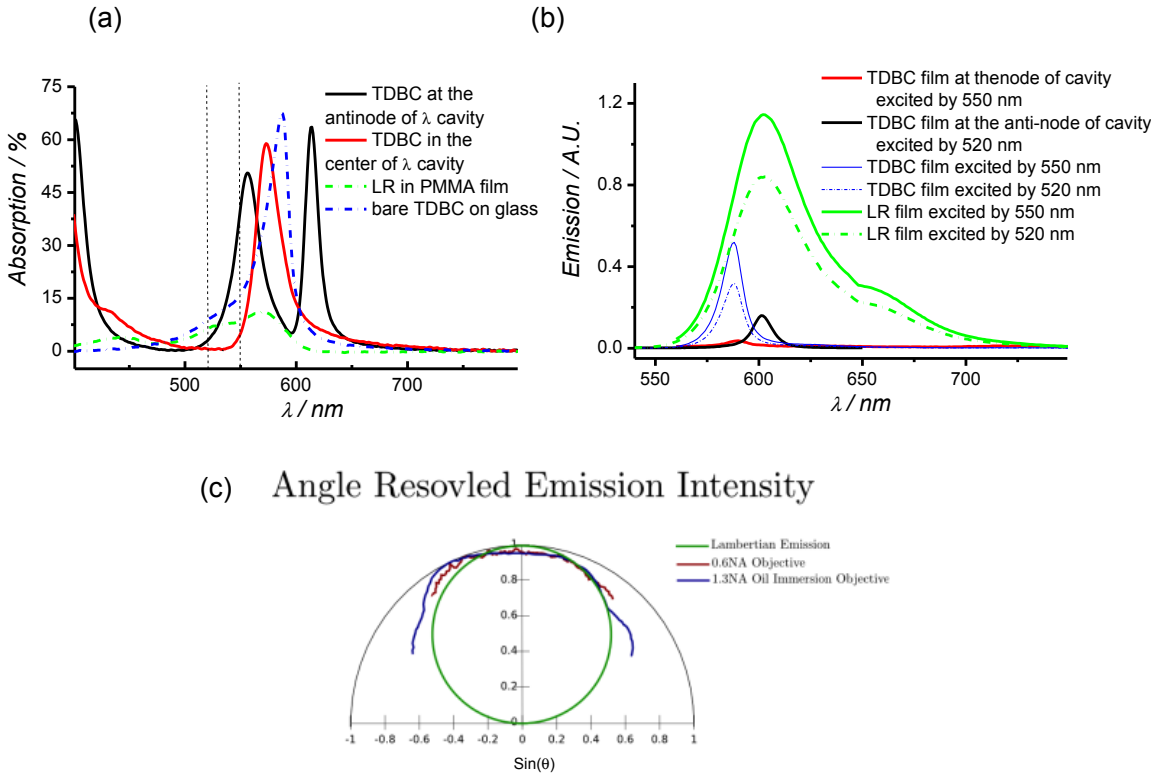

Figure 5.10: Absorption (a) and emission spectra (b) of bare LBL TDBC film on quartz substrate, the TDBC film at the anti-node and in the center of the λ cavities, and the referenced LR in PMMA film (with calibrated QY = 0.3). Note that we used the same incident angle (θ= 0°) of excited light for emission spectrum as the absorption spectrum. (c) Angle resovled emission intensity of P- when LBL TDBC film deposited at the anti-node of λ cavity. The maximum collection angle (60°) was reached using an oil immersion objective (NA=1.3). The rest of the emission pattern was extrapolated from a Lambertian fit. Figure is from reference.[60]

When the J-aggregate layer is at the anti-node in the $\lambda/2$ cavity, Φ_f (P-) ~ 8×10^{-3} while it is slightly higher (10^{-2}) at the anti-node of the λ cavity. In contrast, at the center of the λ cavity where only J_1 emits, $\Phi_f(J_1) = 10^{-3}$. These very low values confirm that non-radiative relaxation is the dominant decay pathway in both coupled systems and the bare TDBC with $k_{nr} \sim 10^{12}\ s^{-1} > 100k_r$. This is due to the numerous molecular vibrational modes which are available to redistribute the energy (ca. 180 fundamental modes in the

case of TDBC), and also the energy transfer to some defects and perhaps dimers in the J-aggregates [135, 136].

Next we undertook fs transient absorption spectroscopy (the principle of this technique is described in Section 6.1) measurements by exciting at 585 nm, comparing the spectra and the decay dynamics outside the cavity with the data collected for different positions inside the cavity. Figs. 5.10a and c show the differential absorption spectra recorded for the λ cavity at the node (center) and the antinode respectively. In the center the differential spectrum is that of the bare TDBC and decays with the same lifetime ($\tau_{1/2}$ = 0.6 ps) (Fig. 5.11b) in agreement with the fact that the system is in the weak coupling regime.

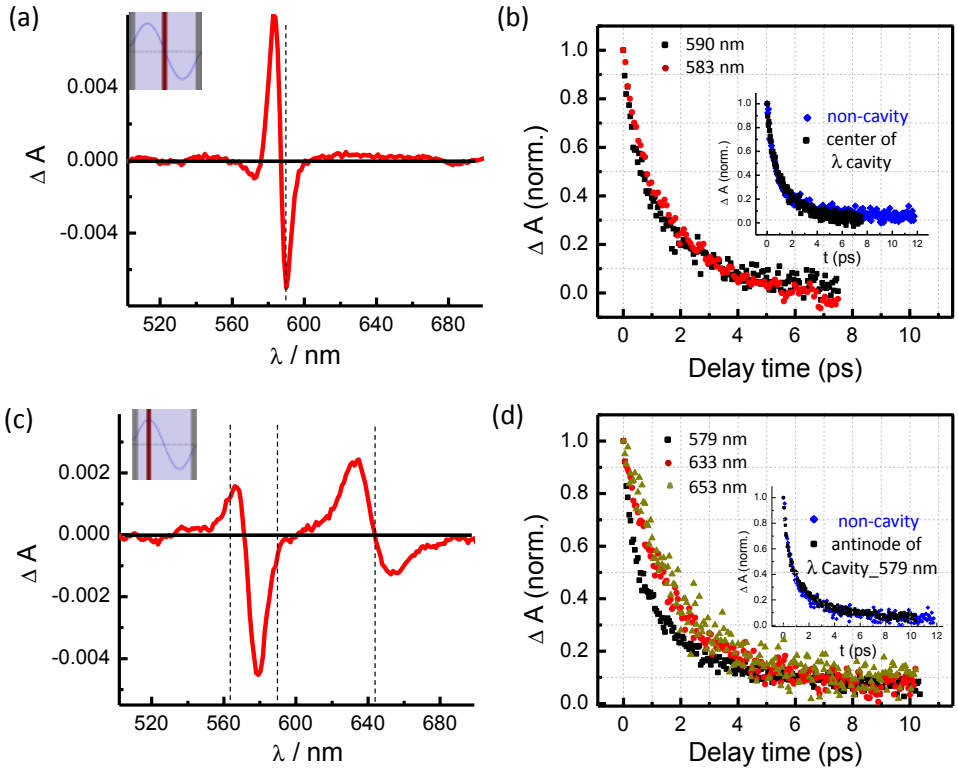

Figure 5.11: (a) and (c) Transient absorption spectra of TDBC layer in the center and at the antinode of λmode cavity. The dashed vertical lines indicate the absorption maxima of the J-band of uncoupled molecules, P+ and P- in (c). (b) and (d) Decay kinetics for the two spatial positions in (a) and (c) respectively, measured at different wavelengths. The insert in (b) show that the decay at the node of the cavity is identical to that of the TDBC layer in the absence of the top mirror (non-cavity). The insert in (d) shows that the decay at 579 nm for a TDBC layer at the anti-node is the same as that of TDBC in the absence of cavity (non-cavity). Figure is from reference.[60]

At the antinode, the spectral shape (Fig. 5.11c) is in agreement with those reported previously for strongly coupled TDBC systems.[54, 59, 137] However at this location, the decay depends on the detection wavelength. At the region corresponding to the absorption of the uncoupled molecules (around 588 nm), the decay matches that measured outside the cavity ($\tau_{1/2}$ = 0.6 ps), but at the region corresponding to the P- absorption, the decay lifetime is longer ($\tau_{1/2}$ = 1.4 ps) (Fig. 5.11d). It should be noted that the decay kinetics are not a true exponential but we checked that they are independent of pump intensity in the range used even inside the cavity for the uncoupled TDBC. In the other words, the complex decay is due to intrinsic inhomogeneity in the sample.

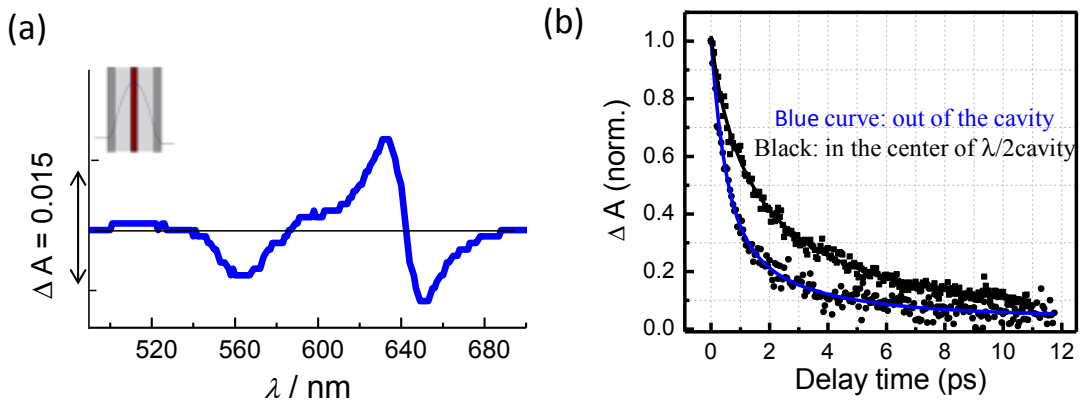

Figure 5.12: (a) Transient absorption spectrum of TDBC molecular layers in the center of a λ/2 cavity characteristic of P-. (b) Decay of the coupled state (independent of wavelength) compared to that of TDBC in the absence of a cavity (non-cavity). Figure is from reference.[60]

In the λ/2 cavity, the transient spectra have features of the strongly coupled system and the decay kinetics ($\tau_{1/2}$ = 1.4 ps) is the same at all wavelengths, indicating that most of the TDBC molecules are coupled (see Fig. 5.12). We summarized the experimental data of different samples in Table 1.

Table1. Summary of experimental results of different samples

	J_1 of Bare film	P- of λ/2 cavity Antinode	J_1 of λ cavity Node	P- of λ cavity Antinode
$\tau_{1/2}$ (ps)	0.6	1.4	0.6	1.4
Φ_f	2×10^{-2}	8×10^{-3}	1×10^{-3}	1×10^{-2}
k_r (s^{-1})	3×10^{10}	5.7×10^{9}	1.7×10^{9}	7.1×10^{9}
k_{nr}(s^{-1})	1.6×10^{12}	7.1×10^{11}	1.7×10^{12}	7.1×10^{11}

The above measured lifetimes and Φ_f (P-) are related by k_r as seen from eqn. (5.9). k_r of J-aggregates are known to be much larger than those of the monomer due to the extended exciton delocalized over approximately 10 molecules. It can also be calculated from the absorption using Einstein's coefficients as is typically done to estimate the radiative rates of organic molecules with the Bowen and Wokes equation[138, 139]

$$k_r \approx 2.9n^2\bar{\nu}^{-2}\int \varepsilon d\nu \qquad (5.10)$$

where n is the refractive index of the film, $\bar{\nu}$ is the central absorption frequency in cm^{-1} and ε is the molar extinction coefficient. For TDBC, k_r is reported in the literature to be ~4×10^9 s^{-1} in solution[140], yielding $\Phi_f(J_1)$~2×10^{-3}, while if we calculate k_r from our experimentally determined absorption using eqn. (5.10) assuming the cross-section of 10 molecules contributing to a typical excitonic excitation, we find k_r ~10^{10} s^{-1} which gives Φ_f (J_1)~6×10^{-3}. These values are in reasonable agreement considering all the uncertainties.

For P-, we can also estimate k_r from eqn. (5.10) assuming that the oscillator strength is ultimately preserved in the coupled system of the two new transitions (P+ and P-). Measurement of the area under the absorption curve before and after coupling indicates that this is indeed the case. With this approach, we estimate k_r ~0.5×10^{10} s^{-1} which, given a lifetime of 1.4 ps, yields Φ_f (P-) ~7×10^{-3}. This is in remarkable agreement with our measured values.

These results clearly indicate that the lifetime of the P- is much longer than the lifetime of the photon in the cavity (here 20 fs). This has been observed in previous case[54, 59, 78, 137] but here the combination of precise positioning inside the cavity has allowed verification of this point beyond doubt. In the past, long lived P- has been generally attributed to complex energy transfer processes involving the weak/uncoupled molecular states, a form of delayed fluorescence.[42] The quantum yields and the transient dynamics presented here are mutually consistent and do not require the invocation of any such special mechanism. P- is thus intrinsically longer lived than its constituent states. This might seem surprising but there are many examples of species whose lifetime are

longer than their components. In molecular science, the most notable are excimers formed from the coupling of excited molecule (M*) and another molecule in the ground state (M):

$$M^* + M \rightleftharpoons (MM^*)$$

The excimer is stabilized by the coupling interaction, leading to cases where the lifetime of (MM*) is much longer than M*. For instance, excited naphthalene monomer has a lifetime of 52 ns at room temperature in ethanol while its excimer has a lifetime of 380 ns.[138] Similarly upon formation of the exciplex between naphthalene diimide and toluene, the lifetime increases by an order of magnitude over the monomer.[141]

The lifetime of the hybrid light-matter states is going to be sensitive to the Rabi splitting and not necessarily longer than both the component states. In the Markovian regime, where the splitting is typically small relative to k_BT, the lifetime of the polaritonic states are similar and determined by the shortest of the states involved in the strong coupling. In the cases where the Rabi splitting is much larger than k_BT, the coupled system is in the non-Markovian regime in which case the properties of P- and P+ cannot be predicted in any simple way.[77] Instead these properties can only be determined theoretically in the coupled state *ab initio*. In the non-Markovian regime, P+ is always observed experimentally to be much shorter lived than P-, in a similar way to upper excited molecular states, due to rapid vibrational relaxation. As we have shown here, P- lifetime can be relatively long but it is also determined overwhelmingly by the very fast non-radiative relaxation processes ($k_{nr} \sim 10^{12}$ s^{-1}). Polariton fluorescence is thus a very minor decay path. On the fundamental side, this cautions against using only emission spectra to elucidate decay mechanisms. In addition, despite the fact that polaritons are quasi-bosons, strongly coupled molecular systems are in most cases uninteresting for making light-emitting devices unless the system is carefully chosen such as in the demonstration of polariton lasing.[68] Nevertheless, strong coupled systems offer many exciting possibilities for modifying molecular and material properties with potential applications from chemistry to opto-electronics.

5.4 Conclusions

In this chapter, the efficiency of light-molecule strong coupling was tuned by precisely varying the spatial position of a thin layer of cyanine dye J-aggregates in FP micro-cavities. The vacuum Rabi-splitting follows the shape of the field amplitude distribution in the cavities. It tells that the strength of the coupling interaction varies linearly with the vacuum field amplitude defined by the cavity, as expected from the Jaynes-Cummings theory. Placing the layer at the cavity field maximum affords an interaction energy (Rabi splitting) of 503 meV, a 62% increase over that observed if the aggregates are simply spread evenly through the cavity, placing the system in the ultra-strong coupling regime.

The measured lifetime of the lowest polaritonic state P- (as long as ps) and the emission quantum yields are mutually consistent. The observation of P- lifetime longer than its constituent states is outside conventional understanding of polariton lifetimes. Moreover, the measured low quantum yield (~ 10^{-2}) demonstrates that the polariton decay is dominated by non-radiative processes in contrast to what might be expected from the small effective mass of the polaritons.

6 Ultra-strong light-molecule coupling in micro-cavities: spectroscopy and dynamics

The previous chapter examined the emission properties, quantum yield, and lifetime of cavity polaritons using the example of LBL J-aggregates as the organic material oscillator. We report here a systematic study of strong coupling involving three molecules with very different photo-physical properties. In particular we will analyze which wavelengths are necessary to produce emission from the lowest polaritonic states (P-) by fluorescence excitation spectroscopy and show that the excitation spectra are very different from the static absorption of the coupled systems. Furthermore we will report the emission quantum yields and excited state lifetimes again, which are self-consistent. The above results raise a number of fundamental questions that will be discussed. At the beginning of this chapter, the details of one important experimental method, ultra-fast transient absorption spectroscopy, will be introduced in detail.

6.1 Transient absorption spectroscopy

Transient absorption spectroscopy, also known as flash photolysis, is a technique used to analyze the identity and dynamics of excited species, and can give information on processes such as photoinduced energy and charge transfer. The absorbance at a particular wavelength or range of wavelengths of a sample is measured as a function of

time after excitation by a flash of light. In our experiment, both the light for excitation ('pump') and the light for measuring the absorbance ('probe') are generated by a 150 fs laser pulse, the arrival of one at the sample delayed from the other by optical delay lines. We use transient absorption spectroscopy here to measure the spectral and lifetime characteristics of P- by exciting at a given wavelength. We also use this equipment to carry out the absorption excitation spectra by varying the pump wavelength.

6.1.1 Principle[142]

Let us first consider the general case of a sample outside an optical cavity, such as a bare molecular film on a quartz substrate or a solution in a quartz cell. The absorption of the sample can be described by the Beer–Lambert law in terms of absorbance (A)

$$A = -\log_{10}(\frac{I}{I_0}) = \varepsilon l c \tag{6.1}$$

where I_0 and I are the optical intensity of the probe-beam before and after transmission through the sample; ε, l, c are the ground-state absorption coefficient, thickness, and molar concentration of the sample. In transient absorption spectroscopy, a differential absorbance (ΔA) is used to monitor the dynamics of the transient species

$$\Delta A = A_{pump-on} - A_{pump-off} \tag{6.2}$$

where $A_{pump\text{-}off}$, $A_{pump\text{-}on}$ are the absorbance of the sample measured in the absence and presence of the excitation of a pump-beam respectively.

The sample is in the ground electronic state S_0 before the excitation and its absorbance is thus

$$A_{pump-off} = \varepsilon l c \tag{6.3}$$

After the excitation, some fraction of the sample transitions from (for example) the ground state to the first excited electronic state: $S_0 \rightarrow S_1$. The absorbance of the sample changes to

$$A_{pump-on} = \varepsilon l (c - c^*) + \varepsilon^* l c^* \tag{6.4}$$

where c^*, ε^* are the concentration and absorption coefficient of the excited state S_1. Then eqn. (6.2) can be written as

$$\Delta A = (\varepsilon^* - \varepsilon) l c^* \tag{6.5}$$

This equation shows that the transient absorbance ΔA is linear with the concentration of the transient excited species; therefore it is reasonable to extract the time evolution of the transient species by monitoring the time evolution of the transient spectrum. If the spectrum evolves with the same shape and kinetics at every wavelength over some time range after pump excitation are the same, it suggests that only one transient excited state is significantly populated over that time-scale. Because in eqn. (6.5), $\varepsilon, \varepsilon^*$ is a function of wavelength $\varepsilon(\lambda)$, $\varepsilon^*(\lambda)$ and only c^* is associated with time $c(t)$, eqn. (6.5) is rewritten as

$$\Delta A(\lambda, t) = [\varepsilon^*(\lambda) - \varepsilon(\lambda)] l c^*(t) \tag{6.6}$$

which tells us that ΔA varies as a function of wavelength (spectrum) and time (kinetics). Moreover, the observed transient spectrum is a sum of two contributions: $\varepsilon^*(\lambda)$ and $-\varepsilon(\lambda)$. The positive contribution due to absorption of the excited state of the sample and negative one associated with the ground state depopulation (bleaching) following the pump. In other words, the spectrum of the transient species is the superposition of the absorption of the excited state and the bleaching of the ground state. If there are several transient species, then

$$\Delta A(\lambda, t) = \sum_i [\varepsilon_i^*(\lambda) - \varepsilon(\lambda)] l c_i^*(t) \tag{6.7}$$

Besides the contributions from absorption and bleaching, the observed transient spectrum can show contributions due to stimulated emission from a transient state, if the probe pulse has sufficient peak power density (typically only observed in transient absorption using femtosecond laser probe beams). It is equivalent to a negative absorption as $-\varepsilon^*_{SE} l c^*$ where ε^*_{SE} is proportional to the cross section for stimulation emission. This gives then the full expression for ΔA by modification of eqn. (6.7)

$$\Delta A(\lambda, t) = \sum_i [\varepsilon_i^*(\lambda) - \varepsilon(\lambda) - \varepsilon_{i,SE}^*(\lambda)] l c_i^*(t) \tag{6.8}$$

6.1.2 Signal acquisition

The transient absorption signal is normally recorded in the configuration shown in Fig. 6.1: the sample is excited by an intense pump pulse and a weak probe pulse (white

light) is sent through the sample with a delay τ with respect to the pump pulse. The detector records the intensity of probe beam after traveling through the sample in the presence/absence of the pump. From eqns. (6.1) and (6.2), the differential absorbance is measured as

$$\Delta A = (\log \frac{I_0}{I})_{pump-on} - (\log \frac{I_0}{I})_{pump-off} \tag{6.9}$$

Typically a fraction of the probe is split off in front of the sample, and used as a reference (I^r) to control for power density fluctuations of the probe beam in time and wavelength

$$\frac{I^r_{pump-off}}{I^r_{pump-on}} = \frac{(I_0)_{pump-off}}{(I_0)_{pump-on}} \tag{6.10}$$

Substituting the eqns. (6.10) to (6.9), ΔA is calculated as

$$\Delta A = \log(\frac{I_{pump-off}}{I_{pump-on}} \times \frac{I^r_{pump-on}}{I^r_{pump-off}}) \tag{6.11}$$

Again this equation is valid across all wavelengths of the probe beam. To extract kinetics, ΔA is calculated using eqn. (6.11) for various τ in the time range of interest.

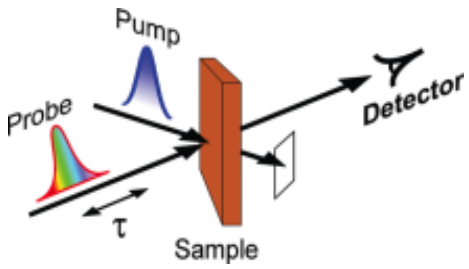

Figure 6.1: Schematic representation of a typical pump-probe experiment.

6.1.3 Helios setup

We used a commercial transient absorption spectrometer (Helios, Ultrafast Systems) to measure ΔA, and discuss here some of its peculiarities, especially for measurement of optical cavities where the possibility of significant optical reflections must be considered.[59] As illustrated in Fig. 6.2, probe pulses at 1 kHz of intensity (I_0)

pass through the sample and can be collected in reflection (I_R) or transmission (I_T). Pump pulses pass through the same part of the sample at 500 Hz, thus I_T or I_R is collected alternatingly in the absence or presence of the pump. One arm is used to monitor the spectral intensity fluctuations of the probe.

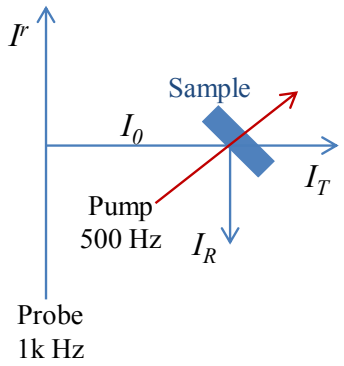

Figure 6.2: Beam paths before and after the sample in the Helios setup.

For typical dielectric samples, $I_R \sim 0$, transient absorption is calculated from measurement of I_T in the presence and absence of the pump (as already discussed earlier). For a cavity with a thick back mirror (e.g. 300 nm thick silver film in the previous chapter), $I_T \sim 0$, and transient absorption is calculated from measurements of I_R. For the intermediate case (*e.g.* a cavity with thin mirrors) both I_R and I_T are significant. In this case one must measure 'ΔA' using the Helios on both the *R* and *T* lines separately, and then manipulate to get the global ΔA. However there is no way to get raw data of I_T and I_R in the absence of pump from the Helios system, only 'ΔA' recorded by eqn. (6.11) is available, and measurement of standard transmission or reflection spectra on another spectrometer is required to extract the true change in absorption.[59]

6.2 Systematic studies on ultra-strong light-molecule coupling

For better understanding of the properties of the polaritonic states, their dynamics and how they are modified relative to the bare molecules, a greater variety of molecules

need to be characterized to look for trends. In this section, the photophysical properties of a subset of strongly coupled molecules with very different bare features are compared using both static and fs transient absorption spectroscopy. The results raise fundamental questions that will be discussed.

6.2.1 Three different molecules

The three different molecules that were investigated under strong coupling are as follows[64] :

TDBC- The first one is the well-known TDBC in its J-aggregated form which was used in previous chapter. The only difference herein is that the molecules/aggregates are dispersed in the polymer (PVA) by spin-coating instead of in a high density film deposited by LBL. J-aggregates are themselves formed by transition dipole-dipole strong coupling of neighboring molecules, where the symmetry of the aggregates is such that only the transition from the ground state to the lower coupled state is allowed, as illustrated in Fig. 6.3b. The Stoke shift is characteristically very small (<10 meV).

The Rabi splitting is such that P− lies below the Frenkel excitonic state involved in the coupling process (Fig. 6.3b). As a consequence, the energy level of the lower polariton branch lies amongst the higher vibrational states of the ground state manifold.[77] Thus it will relax very efficiently by dissipating energy into this bath of non-radiative states. This is despite the fact that polaritons, generated by excitation to P− or P+, are expected to interact (scatter) very weakly with phonons due to their low effective mass (being quasi-bosons). The measurements presented in Chapter 5 on TDBC (having ~180 normal vibration modes) in FP cavities show, indeed, that the non-radiative decay rate constant $k_{nr}{}^{P-}$ of P− is smaller than the corresponding k_{nr} of the bare molecule. Nevertheless, in both cases the non-radiative rate constants are in the order of 10^{12} s^{-1}. This dominates the decay kinetics of P−. It is also the source of the low P− fluorescence quantum yield, $\Phi_f{}^{P-} = \frac{k_r{}^{P-}}{k_r{}^{P-} + k_{nr}{}^{P-}}$, since the radiative rate constant $k_r{}^{P-}$ has an upper limit for a fully allowed transition in the order of 10^9 ~10^{10} s^{-1}. Vibrational relaxation *within* electronically

excited states occurs on the 100 fs timescale and is characterized by small spectral shifts, or sliding, during the relaxation. This has also been seen for the P− of TDBC and it is important that this is not confused with other possible excited decay pathways when observing P− and P+ at very short time scales.[59]

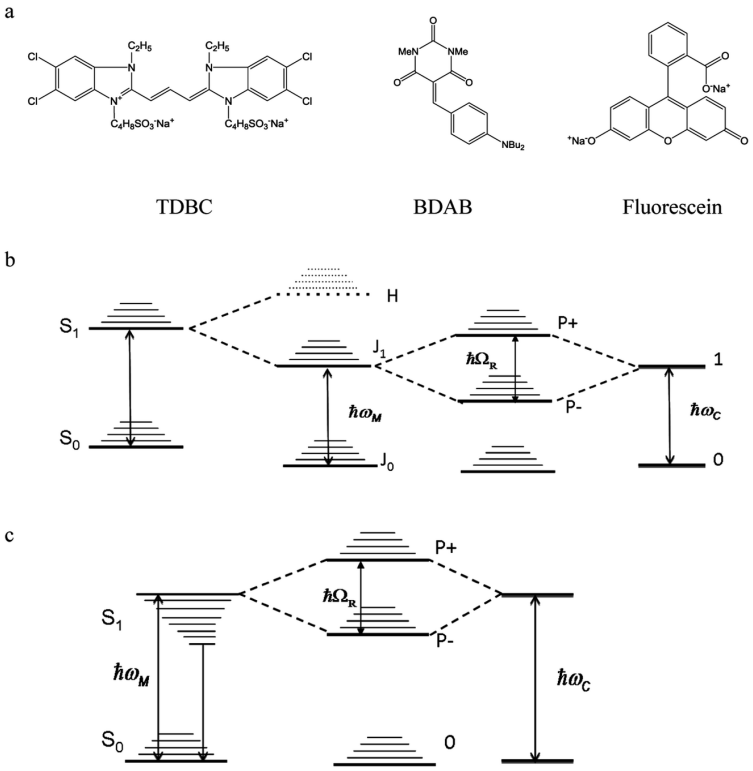

Figure 6.3: Molecular structures of the three compounds (a) and the corresponding energy diagrams for TDBC (b) and BDAB (c) upon coupling. The TDBC dipole–dipole coupling gives rise to new states marked J and H, but for the J-aggregates only the J state is observed in the absorption spectrum as the transition to H is forbidden. Figure is from reference.[64]

BDAB- The second molecule is a so-called push–pull molecule, 5-(4-(dibutylamino) benzylidene)-1,3-dimethylpyrimidine-2,4,6(1H,3H,5H)-trione (BDAB)[66] with an unusually large Stokes shift (~560 meV). The strong coupling energy level diagram for such molecular systems that undergo significant electronic re-distribution in the excited state is illustrated in Fig. 6.3c. The strong coupling in this case involves the transition from the molecular ground state to a higher vibrational state of the excited state manifold (the Franck–Condon transition). As a consequence, the lower P− polariton

branch may lie above, or be isoenergetic with, the relaxed excited state of the bare molecule (see for instance ref.[143]). This may have consequences on the dynamics and the decay processes of the coupled system, as has already been shown by Törmä and co-workers.[143]

Fluorescein, as its name indicates, is a highly fluorescent dye in dilute solutions with a $\Phi_f \approx 0.9$ and a Stoke shift of ~ 110 meV. It is a representative of standard organic dyes and will strongly couple to the cavity.

6.2.2 Experimental methods

All the steady state measurements were performed in reflective cavities, in which the Ag mirror deposited on the glass was 200 nm thick, and the top mirror was 30 nm thick. For pump–probe measurements, experiments were performed in transmission with cavities in which both mirrors were 30 nm thick and kinetics were recorded in terms of $\Delta T / T$. The bottom Ag film was sputtered on borosilicate glass, followed by spin-coating of the molecules dispersed in a polymer to form a thin film, and then sputtering the second Ag film on top. TDBC films were spin-cast from aqueous solution (Milli-Q) containing 0.5% TDBC and 5% PVA (M.W. 205 000) by weight. Fluorescein films were cast from aqueous solutions of 1% fluorescein disodium salt and 2% PVA by weight. BDAB films were cast from toluene solutions of 0.5% BDAB and 1% PMMA, (M.W. 120 000) by weight. Toluene (Sigma Aldrich), PVA (FLUKA), PMMA (Sigma Aldrich), fluorescein disodium salt (Exciton) and TDBC (Few Chemicals) were obtained commercially and used without further purification. BDAB was synthesized as follows. 4-dibutylaminobenzaldehyde (196 mg, 840 μmol, 1.00 eq.) and 1,3-dimethylpyrimidine-2,4,6(1H,3H,5H)-trione (131 mg, 840 μmol, 1.00 eq.) were dissolved in 5 mL of ethanol. The resulting mixture was refluxed for 3 h. After cooling the precipitate was filtered off and washed with 10 mL of H_2O, 10 mL of ethanol and 10 mL of n-pentane. The yellow solid was dried in vacuum to give the product in quantitative yield (312 mg). 1H NMR (400 MHz, CDCl3, δ/ppm): 0.98 (t, J = 7.3 Hz, 6H), 1.45–1.32 (m, 4H), 1.69–1.57 (m, 4H), 3.44–3.37 (m, 10H), 6.66 (d, J = 8.98 Hz, 2H), 8.36–8.41 (d, J = 9.23 Hz, 3H). ESI-

MS: *m/z*: 360.3 (100%). HRMS (ESI, *m/z*): calculated for $C_{21}H_{29}N_3NaO_3$ 394.210; found 394.210.

Steady-state transmission and reflection spectra were taken on a Shimadzu UV3101 spectrometer. Steady-state fluorescence spectra were taken with a Horiba Jobin Yvon-Spex Fluorolog-3 fluorimeter. Pump–probe experiments were carried out with narrow band (linewidth = 6 nm), 150 fs-pulse tunable Spectra Physics laser system. The spectra were recorded using low-energy (<100 μJ cm^{-2}) pumping pulses to avoid spurious effects.

6.2.3 Results

The strongly coupled samples were prepared by encasing polymer films containing the dyes between two silver films to form an optical cavity (see Experimental section for details). The thickness of the polymer film, and thus the final separation between the Ag mirrors in the cavity, was chosen to give an optical mode resonant with the absorption maximum of the dye/aggregate (at 590 nm for TDBC, 470 nm for BDAB, and 510 nm for fluorescein). The Q-factors of these cavities are low, typically ~10–20. Unless specified otherwise, the cavity thicknesses are tuned such that the Rabi splitting occurs at normal incidence ($k_{//} = 0$) where the photon–exciton mixing is 50: 50.

Transition probability to P−

We start by comparing in Fig. 6.4 the optical absorption and emission (fluorescence) spectra of the FP cavities containing TDBC, fluorescein and BDAB at normal incidence with their bare spectra. All the absorption spectra are inhomogeneously broadened, even TDBC. The two new absorption peaks corresponding to P+ and P− (blue solid curves in Fig. 6.4) have a full width half maximum (FWHM) that is mainly determined by that of the cavity mode, as expected.[144] It should be noted that for fluorescein the cavity induced splitting is more complex, due to the double peaked absorption of the bare molecule, as seen before for Rhodamine.[61] The coupling strengths

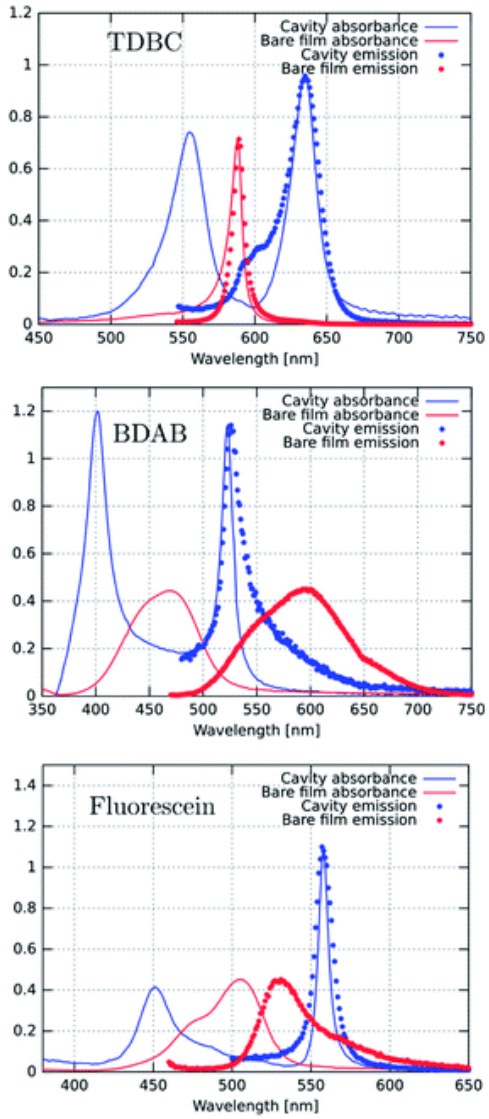

Figure 6.4: Absorbance (solid lines) and emission (dotted lines) spectra of the bare molecules (red) and the corresponding coupled systems (blue). The excitation wavelengths were either 530 nm for TDBC or 450 nm for BDAB and fluorescein. Figure is from reference.[64]

($\hbar\Omega_{VR}$) for these samples are, respectively, 277, 554 and 720 meV for TDBC, BDAB and fluorescein and the corresponding fractions of the transition energy ($\hbar\Omega_{VR}/\hbar\omega_0$) are 13, 24 and 27%. These fractions, especially the latter two, are sufficiently high that the coupled systems are in the ultra-strong coupling regime which has consequences on their properties as already discussed. Notice that the P− fluorescence peak of coupled BDAB is at higher energy than that of the bare molecule in agreement with the schematic

illustration of Fig. 6.3c. Careful observation of the emission spectra of the coupled systems shows that at least some fluorescence of the bare molecules is always present in these cavities. In other words, some of the molecules are not coupled to the cavity due to the disorder (energetic and orientational) in the system.[66, 145] This uncoupled emission does not disperse with angle and therefore can be easily distinguished from the P− emission. The apparent Stoke shift of the P− emission for all three molecules is extremely small or, depending on the conditions of the sample, it sometimes even appears to be slightly blue shifted relative to absorption.[59] The blue shifted emission and its origin will be discussed again further on, after the presentation of more results.

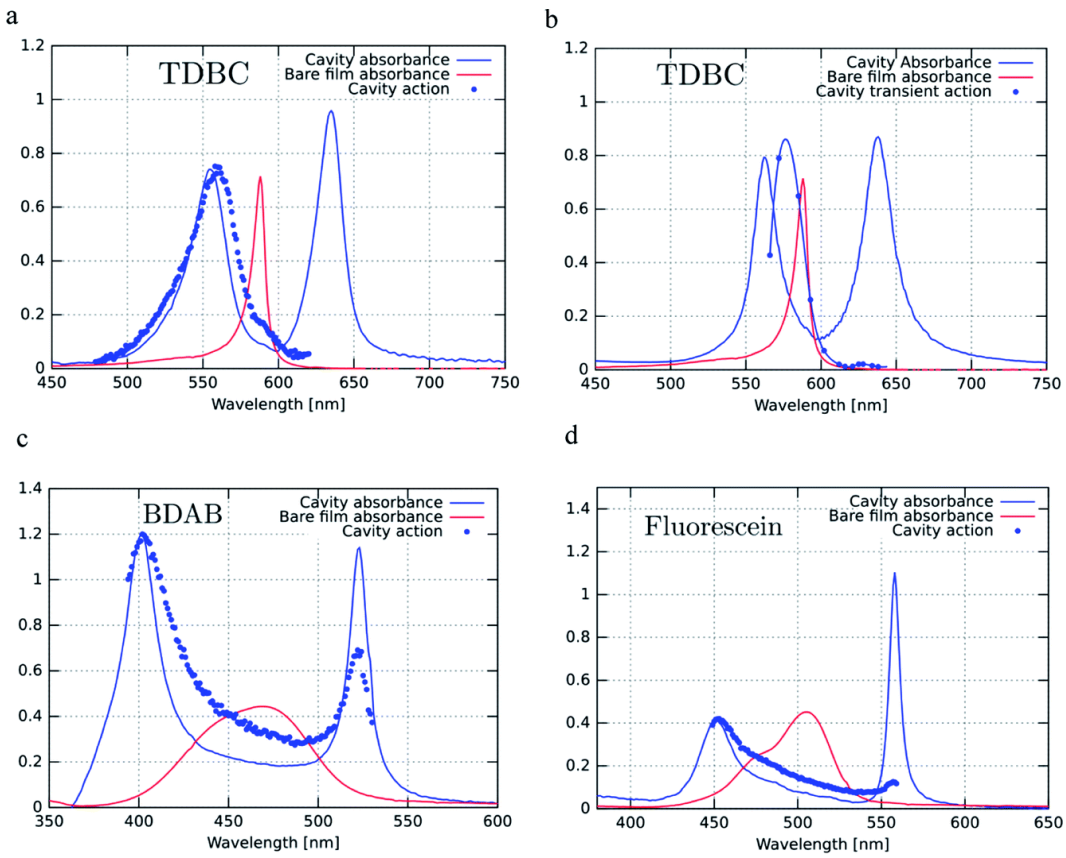

Figure 6.5: Excitation or action spectra (blue dots) recorded at normal incidence for P− emission for (a) TDBC (at 680 nm), (c) BDAB (at 540 nm) and (d) Fluorescein (at 576 nm) and (b) for P− transient absorption of TDBC. These spectra are compared to the bare molecule absorbance spectra (solid red lines) and the strongly coupled system absorbance spectra (solid blue lines) of the same samples. Figure is from reference.[64]

Next, we measured the excitation spectra associated with the P− emission. This is a standard technique used in molecular science to understand the origin of the emission

and associated processes and we first introduced this for studying strong coupling in an earlier study.[59] It consists of measuring the emission or fluorescence intensity, $I_F(\lambda)$, at a given wavelength while scanning the excitation wavelength through the absorption spectrum of the sample. Since $I_F(\lambda) \propto \Phi_F \sigma_A(\lambda) I_0(\lambda) c = \Phi_F I_A(\lambda)$, where $\sigma_A(\lambda)$ is the absorption cross section of the molecule, c is the molecular concentration and $I_0(\lambda)$ is the incident light intensity, one would expect that when I_0 is normalized then $I_F(\lambda)$ will be proportional to the light absorbed, $I_A(\lambda)$. Therefore, by just plotting I_F at a given λ while scanning the normalized excitation, $I_0(\lambda)$, the shape obtained should reflect the absorbance of the states contributing to the emission process.

Figs. 6.5a, c and d show the excitation spectra of the three molecules recorded for their P− emission and these are compared to their absorbance spectra. The first striking feature is the relative contribution of P+ and P− to the emission of P− (here all the excitation spectra have been normalized to the P+ absorbance peak). It thus appears that the direct excitation of the P− peak contributes very little to the P− emission, while when exciting to P+ or the uncoupled molecules it rapidly relaxes to P−, where emission can occur. This relaxation to P− can occur via energy transfer between the coupled and the uncoupled molecular reservoirs as well as by rapid internal vibrational relaxation (IVR). The latter is a standard feature of molecules, with their very large number of normal modes and their overtones that provide a continuum of sublevels between the various states. It is interesting to note that the ratio of P−/P+ excitation peaks is the smallest for TDBC (~ 0.1) and the largest for BDAB (~ 0.5).

This raises the question of whether the direct excitation into the P− static absorption peak actually populates P− or not. To answer this question we also recorded the excitation spectrum of pump–probe experiments by looking at the intensity of the transient absorption spectrum of P−, proportional to the population of P−, as a function of laser pump wavelength. This was possible to do for TDBC since our 150 fs-laser could be tuned to cover the static absorption peaks. The resulting spectrum is plotted in Fig. 6.5b and it has very similar features to the fluorescence excitation spectrum (Fig. 6.5a). Again, the direct excitation of P− appears not to be allowed. Interestingly, the $\hbar\Omega_{VR}$ deduced from the excitation spectra appears to be smaller than the static absorption spectrum

indicates. This is probably the origin of the blue-shifted emission relative to the static absorption that is sometimes observed.

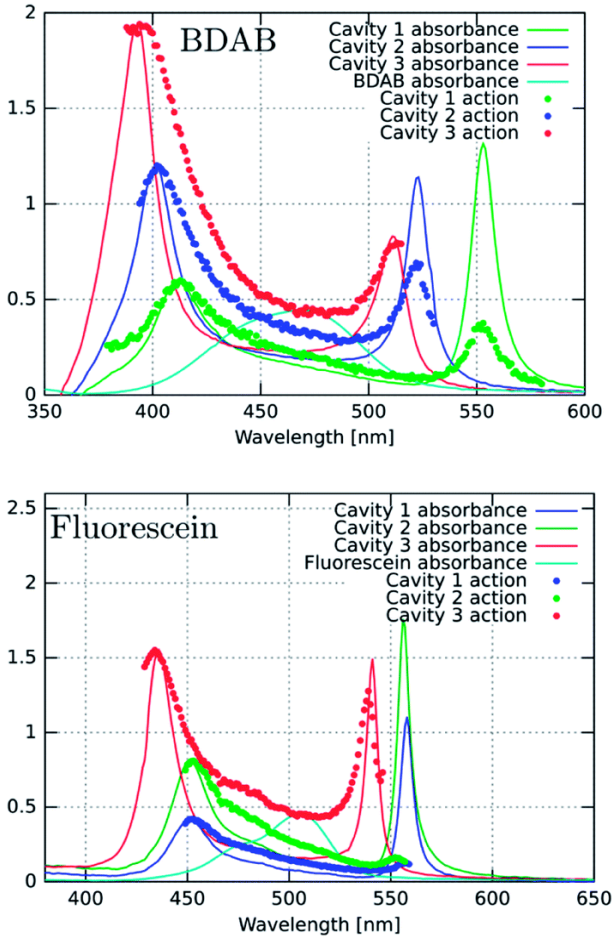

Figure 6.6: Excitation spectra (dotted lines) for BDAB and fluorescein for detuned cavities (red and green curves) compared to the tuned cavities (blue curves) and compared to the corresponding absorbance spectra of the coupled systems and the bare molecules (light blue). The emission detection wavelengths for BDAB are 525 nm (red curve), 540 nm (blue curve) and 600 nm (green curve). For fluorescein these are 556 nm (red curve), 570 nm (green curve) and 576 nm (blue curve). Figure is from reference.[64]

To try to understand the origin of these observations, the cavities were detuned and the fluorescence excitation spectra were recorded. For fluorescein, the detuning of the cavity to higher energies (ca. 60 meV) seems to enhance direct P− excitation, as shown in Fig. 6.6a (red curve). This could be explained by the higher exciton content of the P− branch. However, in the case of BDAB (Fig. 6.6b), the reverse tendency is seen, i.e. detuning to lower energies enhances the relative contribution of P− to the excitation spectrum. Taken together with the results of Fig. 6.5, it appears that the internal vibronic

structure of the molecule plays an important role and also possibly the excited state rearrangement involved in the Stoke shift.

Lifetime of P−

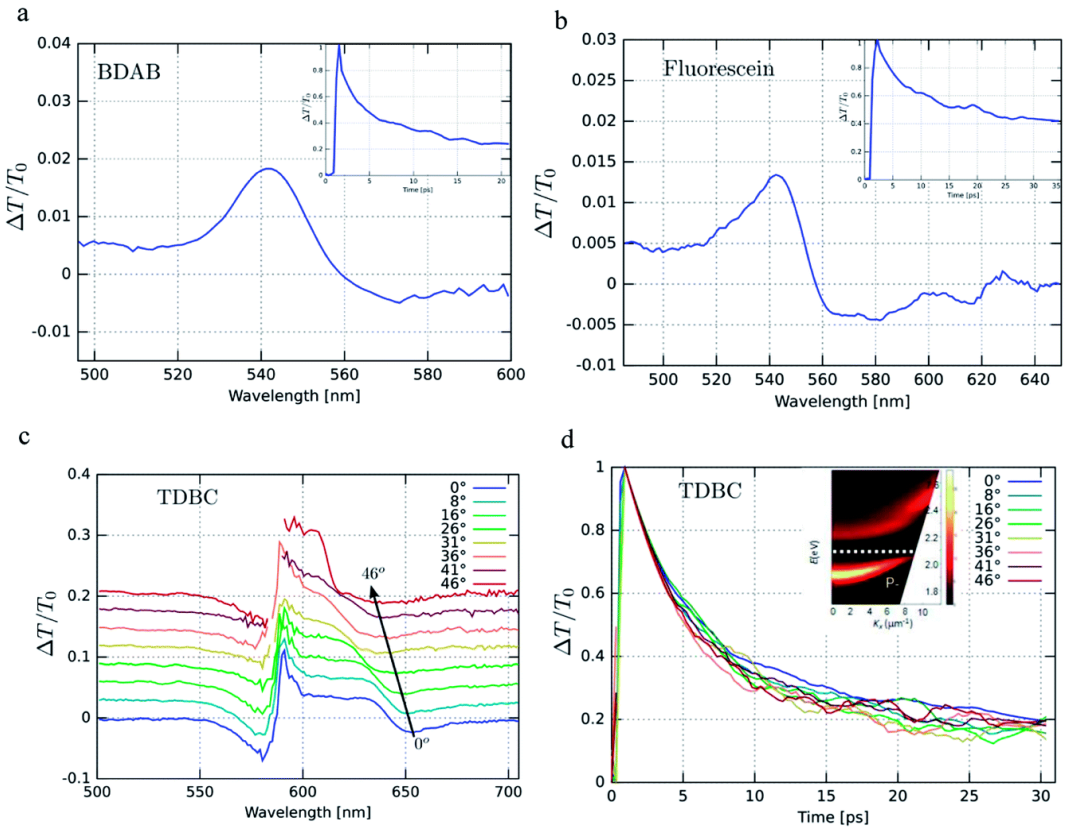

Figure 6.7: (a), (b) and (c) Transient pump–probe spectra with the corresponding decays as inserts for BDAB and fluorescein. In the case of TDBC, the angular dependence of the transient spectra is shown in (c) and the corresponding decays in (d). The insert in (d) shows the dispersion of the static absorption of TDBC in the cavity. BDAB and fluorescein were pumped at 400 nm and TDBC at 585 nm. Figure is from reference.[64]

The transient spectra of the three strongly coupled systems are shown in Fig. 6.7, together with their decay kinetics. The spectra do not evolve over the decay, indicating that they are dominated by a single transient species. The decays are not single exponentials due to the heterogeneities of the samples at the high concentrations that were used to induce strong coupling. The angle dependence of the decay was also measured for TDBC and was found to be invariant, indicating that the lifetime is not dependent on

probed *k*-vector. This indicates that there is no bottle-neck along the P− branch shown in Fig. 6.7d for this sample. Such decay bottle-necks have been seen in other conditions and samples for strongly coupled TDBC.[132]

Table1. Summary of experimental results of different strongly couple molecules

	TDBC	BDAB	Fluorescein
$\tau_{1/2}$ (transient absorption)	4.3 ps	3.5 ps	30 ps
Cavity lifetime (1/linewidth)	2 fs	5 fs	14 fs
Radiative lifetime (predicted value)	0.2 ns (0.4 ns)	1ns (0.1 ns)	3 ns (1.5 ns)
Quantum yield (predicted value)	1×10^{-2} (2×10^{-2})	4×10^{-2} (3.5×10^{-3})	2×10^{-2} (1×10^{-2})

Table 1 below summarizes the dynamical data for the strongly coupled molecules. It first compares the observed half-lives measured by transient absorption with those of the 1/linewidth of the P− resonance and the experimental radiative lifetimes, as well as the predicted ones derived from absorbance peaks of P− using the Bowen and Wokes approximation.[138] It is notable that these two standard methods for estimating lifetimes give such very different values. The measured and calculated quantum yields for TDBC and fluorescein are in very good agreement, considering all the experimental uncertainty, while for BDAB the experimental value is an order of magnitude higher. The latter is not surprising considering the fact that the emission is not from the Franck–Condon transition but due instead to an intra-molecular charge transfer state being at the origin of the large Stoke shift of the bare molecule. Thus, the Bowen and Wokes approximation is not the best model for such a molecule.

6.2.4 Discussions

Conspicuous from the above excitation spectral experiments is the fact that the static absorption peak due to P− (in Figs. 6.4–6.6) does not readily lead to the generation of P− emission or even to the P− transient absorption. We have shown this excitation

behaviour before for TDBC and it has since been confirmed by others.[132] This finding is surprising since one would expect that the static absorption peak of P− would lead directly to populating P− and subsequent emission. This is an important issue since it is a standard assumption that the emission in the spectral region of P− indeed comes from a corresponding state.

One could take a very naïve view to explain the above results from a purely classical interpretation. For instance, the shape of P− emission spectra can be very easily reproduced by taking the emission of the bare molecules filtered by the transmission properties of the cavity (as can be seen in Fig. 6.4). The excitation spectrum would therefore be dominated by the spectral regions where the bare molecule absorbs but enhanced by the modal properties of the cavity (as in Fig. 6.5). This is similar to the treatment of strong coupling by Zhu et al. where it is not necessary to assume the formation of hybrid light–matter states by vacuum Rabi splitting.[87] In this classical vision, the lifetimes of the P− measured by fluorescence or by transient absorption spectroscopy would be those of the bare molecule perturbed by the strong interaction with the confined electromagnetic environment of the cavity.

Nevertheless, the observation of novel and modified properties in strongly coupled systems argues strongly for the quantum interpretation and the existence of hybrid light–matter states. These include coherent emission over large distances,[48] condensation of polaritons,[67, 69] polariton lasing[68] and modification of such properties as chemical rates,[84] work-function[72] and conductivity,[73] amongst others. The significant P– emission quantum yields also argue against a simple cavity filter effect for the fluorescence. Therefore there is a need to understand why the direct excitation of P− is a very inefficient way of populating the state, despite the 50: 50 photonic–exciton mixing for both P+ and P− in our experiments.

One possibility is that the transition probability is very weak despite the strong static absorption. This immediately raises the question of what is at the origin of the static absorption. One unique characteristic of these organic coupled systems is the large inhomogeneous broadening which, coupled to the cavity, could generate dissipation without populating P−. This would leave indirect excitation via higher energy states involving energy transfer and IVR as the most efficient means of then populating the P−

state. However, as we discussed in the previous chapter, the recorded P− emission quantum efficiencies are only compatible with a lifetime in the picosecond regime, as measured for P− both in fluorescence and transient absorption. It is important to note that this is for a most favourable k_r corresponding to a highly allowed transition. If the transition to P− is only weakly allowed, then Φ_f^{P-} should be much smaller, unless the strongly coupled system boosts the emission for an otherwise weakly allowed transition.

6.3 Conclusions

In this chapter, we have shown, through experiments, some of the open questions related to light–matter strong coupling involving molecular materials. Clearly more experiments and theory that can handle such complex materials and the particularities associated with individual molecular structures need to be developed to elucidate these strongly interacting systems. Only then will the full potential of using a confined electromagnetic environment to control material and molecular properties be realized. This chapter also shows clearly that transient absorption spectroscopy has an important role to play in unraveling the complexities of strong light-organic molecule coupling.

7 Phase transition of a perovskite strongly coupled to the vacuum field

Although light-molecule strong coupling is usually associated with splitting of excited states, the ground state energy level also can be pushed down (shown in Fig. 7.3a) due to second order perturbations.[95, 146] This was confirmed by a thermodynamical study of strong coupling of organic molecules.[66] The idea was to consider the strongly coupled cavity as an equilibrium system containing a population of coupled and uncoupled molecules, analogous to a chemical equilibrium. The ratio of the two populations depends on the relative difference in ground state energy of the coupled and uncoupled states. Inspired by these results, in this chapter we report the investigation of whether a ground state phenomenon such as a phase transition of a material can be modified by strong coupling.

7.1 Hysteresis in phase transitions

The phenomenon of hysteresis is found when a system follows one path in going from an initial state A to a final state B, and a different path for the reverse transition from B to A. Hysteresis in phase transitions is widely observed in molecular and solid state systems in chemistry, biology and physics.[147-156] It is studied both for its fundamental features and its technological applications. Most notably, a stable hysteresis in phase-

transition materials, such as polymer gels, spin-crossover complexes, charge-transfer materials and ferroelectrics, form the basis for memory and data storage. [147-156]

Thermodynamically a van der Waals type curve can be used to describe hysteresis associated with phase transitions of cooperative systems with metastabilities.[147] Fig. 7.1 schematically demonstrates such a function for the transition between phase A and B.[148] The two stable and realizable branches (I-C-II and III-E-IV) are connected by an imaginary branch (II-D-IV). In equilibrium phase transitions, the change would follow the path I-C-D-E-III and be reversible. However, during the real scanning of external parameters (e.g. temperature), it is difficult to achieve this equilibrium path since the barrier between the two phases in the transition evolve in time (shown in Fig. 7.2) resulting in a so-called dynamic hysteresis. In other direction, the phase change takes place through metastable regions: metastable state A from C to II and metastable state B from E to IV. Thus the phase changes recycle the hysteresis loop as I→II →III→IV→I.

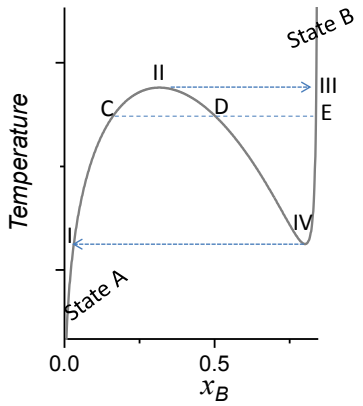

Figure 7.1: Schematic representation of a phase transition between state A and B represented by a van der Waals type curve: the concentration of state B with function of external parameter (temperature).

Based on the concept of metastable states, Eyring et al. developed a thermodynamical model to explain such hysteresis.[148] In the general case of phase transitions, the system is considered to be in a state defined by the lowest point on the Gibbs free energy curve (illustrated by Fig. 7.2). At a low value of an external parameter (here, the temperature), there is a single minimum (I) that represents the system at state A. The second minimum forms as the temperature increases following the direction of the

arrow in Fig. 7.2. The different barriers at transition temperatures (during warming and cooling) results in hysteresis of the phase transition.

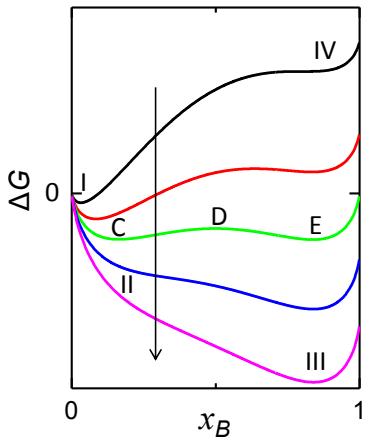

Figure 7.2: The change of Gibbs free energy of the system as a function of concentration of state B when increasing temperature (along the direction of the arrow). The points I, II, III, IV, C, D, and E represent the different phases shown in the hysteresis loop of Fig. 7.1.

Great efforts have been spent to broaden and stabilize such hystereses by chemical modification.[152] Here we show, for the first time, that such hystereses can be also modified and stabilized by strong light-matter interactions. The modifications are attributed to the lowering of the ground states of the two phases by the interaction with the field.

7.2 Phase transition of a strong coupled system

Our previous thermodynamic study under strong coupling demonstrated that the ground state energy shifts with increasing Rabi splitting.[66] An important number is the relative fraction $\hbar\Omega_R^N / \hbar\omega$ since it is an indication of the perturbation of the electronic structure of the material and therefore the relative shift in the ground state energy ΔG_C^Θ as illustrated in Fig. 7.3a.[66] ΔG_C^Θ is the change in the standard Gibbs free energy associated with strong coupling which also determines the fraction of coupled molecules in the

resonant cavity. In the so-called ultra-strong coupling regime $\hbar\Omega_R^N / \hbar\omega$ is typically > 0.1, conditions we will use in this study.[157]

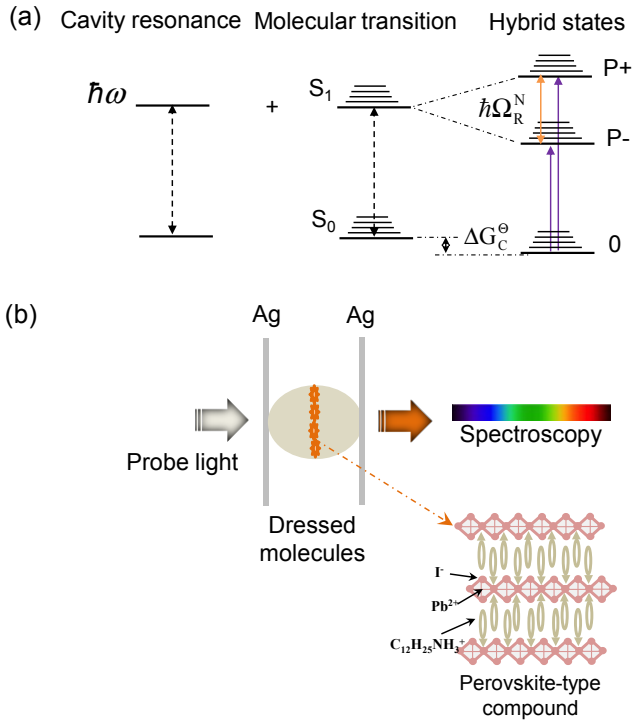

Figure 7.3: (a) The strong coupling between molecules resonant with a cavity mode $\hbar\omega$, generating two new eigen hybrid light-matter states P+ and P- separated by the Rabi-splitting energy $\hbar\Omega_R^N$. The ground-state energy of the coupled or dressed molecules is modified as compare to the bare molecules by the standard Gibbs free energy ΔG_C^Θ. (b) Schematic representation of two-dimensional layered perovskite $[Pb(II)I_4^{2-},(C_{12}H_{25}NH_3^+)_2]$ $(PbI_4(R\text{-}NH_3)_2)$ salt deposited at the anti-node of half-wavelength cavity. Optical spectroscopy was used to analysis $PbI_4(R\text{-}NH_3)_2$'s thermal phase transition property. Figure is from reference.[157]

7.2.1 Experimental methods

Perovskite synthesis: $[Pb(II)I_4^{2-},(C_{12}H_{25}NH_3^+)_2]$ was synthesized by a modified procedure inspired by a literature contribution.[158-160] PbI_2 was dissolved in a 2:1 acetonitrile: methanol solution at 60 °C. To the clear solution thus obtained, HI (57 wt.% in water) was added drop-wise. To the mixture, a stoichiometric amount of dodecylamine $(C_{12}H_{25}NH_2)$ in a 2:1 acetonitrile: methanol was added. The mixture was further stirred at 60 °C for 1 hour. The desired $[Pb(II)I_4^{2-},(C_{12}H_{25}NH_3^+)_2]$ salt precipitated from solution

upon slow evaporation of solvents. No further purification was necessary. All the inorganic, organic salts and solvents were commercially available (Sigma-Aldrich).

Sample preparation: We used a bonding technique (shown in the previous section 5.2.1) for the precise deposition of $[Pb(II)I_4^{2-},(C_{12}H_{25}NH_3^+)_2]$ films in the center of metallic micro-cavities. Briefly, a 30 nm-thick silver film was sputtered on a clean glass substrate, upon which was spin-coated a 40 nm film of poly(methyl methacrylate) (PMMA) (labeled slab A). Slab A was annealed at 70 °C on a hotplate for 15 minutes. A 25 nm thick $[Pb(II)I_4^{2-},(C_{12}H_{25}NH_3^+)_2]$ film was spun onto a separate block of poly(dimethylsiloxane) (PDMS), the surface of which had been rendered hydrophilic by oxygen plasma treatment. The $[Pb(II)I_4^{2-},(C_{12}H_{25}NH_3^+)_2]$film on the PDMS block was kept at 5 °C for 30 minutes. Then the dried film was transferred onto slab A by stamping the PDMS block. Meanwhile, a 30 nm-thick silver film and ~40 nm layer of PMMA were successively deposited on another 1.0 mm thick PDMS substrate by electron evaporation and spin coating (labeled slab B). Slab B was annealed at 70 °C on a hotplate for 15 minutes. Then 0.3% by weight PDMS (poly(dimethylsiloxane), hydroxyl-terminated, MW = 110 000, Aldrich) dissolved in *tert*-butanol was spin cast at 6500 rpm on the slab B, forming a very thin layer (~ 2 nm) to increase adherence in the next step. Finally, the polymer face of slab B was gently pressed onto $[Pb(II)I_4^{2-},(C_{12}H_{25}NH_3^+)_2]$ surface of slab A to form a low Q factor cavity (~10-20). Simultaneously, a non-cavity sample was prepared by the same procedure without 30 nm silver film on slab B. This whole procedure with the two slabs was developed to avoid any possible perturbation of $[Pb(II)I_4^{2},(C_{12}H_{25}NH_3^+)_2]$ and its phase transition properties.

Measurements: Steady-state transmission and absorption spectra were taken on a Shimadzu UV3101 spectrometer throughout the range of 300 – 700 nm. The angular dispersion of transmission spectra were measured with an optical set-up. The temperature was controlled from 5 °C to 66 °C by a precise thermoregulation (Huber). Before recording a spectrum, the temperature setting was kept as long as 5 minutes to ensure thermal equilibrium.

7.2.2 Results and discussion

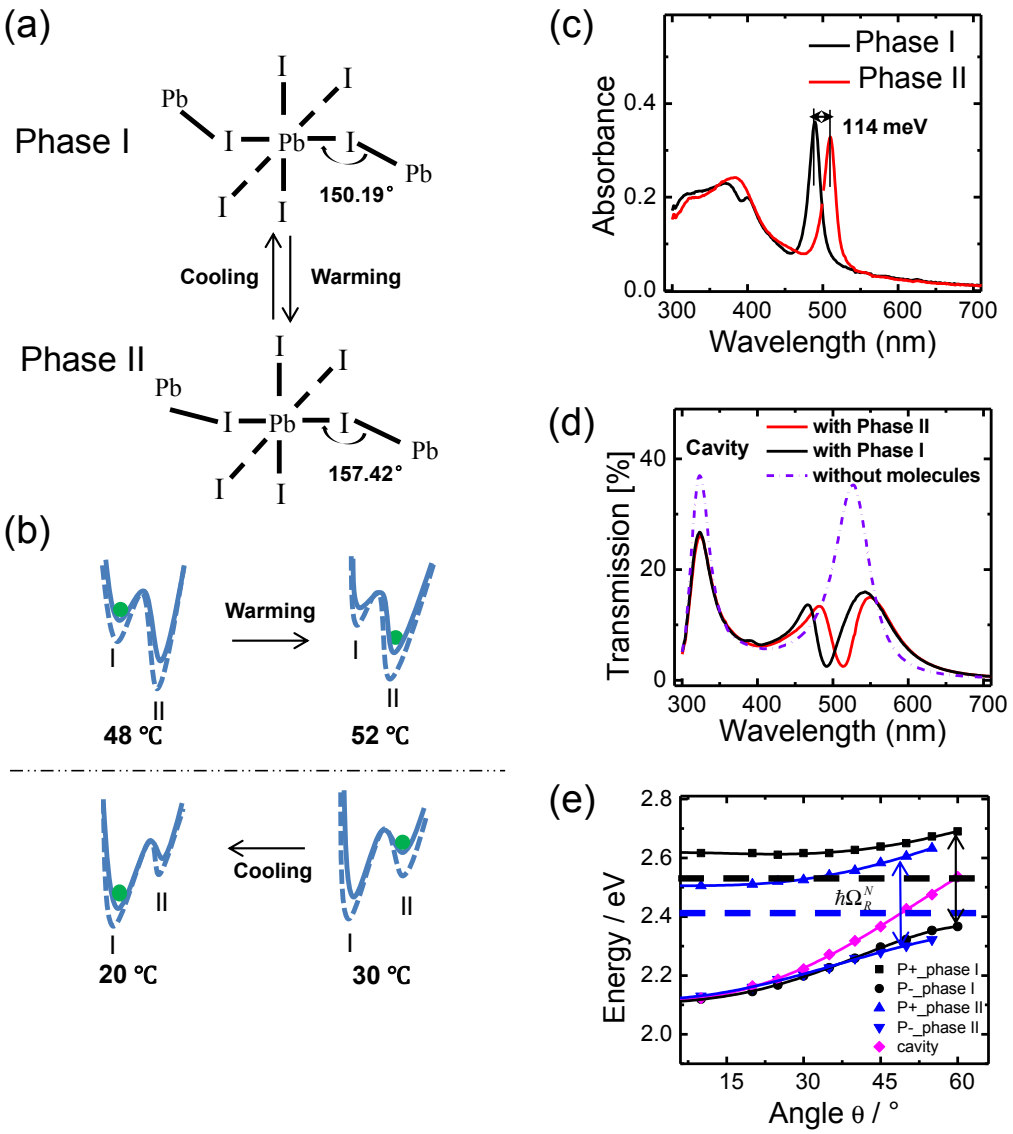

Figure 7.4: (a) $PbI_4(R\text{-}NH_3)_2$ bond angle change during the transition between phase I and II. (b) Diagram of the Gibbs free energy with minima corresponding to states in phase I and II at different temperatures in the hysteresis. The dotted lines indicated ground state shift due to strong coupling. (c) The ground state absorption spectra of bare $PbI_4(R\text{-}NH_3)_2$ film in phase I and II, separated by 21 nm (114 meV). (d) Transmission spectra of cavity alone and with $PbI_4(R\text{-}NH_3)_2$ in phase I and II. (e) Angular dispersion of the cavity with $PbI_4(R\text{-}NH_3)_2$ in phase I (and II), the absorption peak of which is indicated by black (and blue) dashed line. In both cases, $\hbar\Omega_R^N$ is ~ 320 meV. Figure is from reference.[157]

Perovskites such as the hybrid $[Pb(II)I_4^{2-},(C_{12}H_{25}NH_3^+)_2]$ ($PbI_4(R\text{-}NH_3)_2$) salt are known to undergo a phase transition near room temperature involving a bond angle

change[161], as illustrated in Fig. 7.4a and the corresponding spectra of phase I and phase II are given in Fig. 7.4c. The sharp absorption peaks of the two phases are separated by 21 nm or 114 meV. The transition temperatures are ~ 50 °C upon warming and ~ 25 °C upon cooling (Fig. 7.4b) which define the hysteresis loop to which we will return further down.

It has been shown that two dimensional layered perovskites can be strongly coupled to an optical resonance.[31, 162, 163] To maximize $\hbar\Omega_R^N$, and thereby $\hbar\Omega_R^N/\hbar\omega$, for this study, we used the approach developed in Chapter 5, placing a 25 nm film of $PbI_4(R\text{-}NH_3)_2$ at the antinode of λ / 2 metallic FP cavity which is resonant with the absorption transition of the perovskite as schematically shown in Fig. 7.3b. Technically this was achieved by using a multilayer structure (Fig. 7.5a and see sample preparation in 7.2.1). The transmission spectra of the cavity with and without the compound are shown in Fig. 7.4d. Two new peaks, corresponding to P+ and P-, appear for both phases which are separated by an energy greater than the width of the cavity resonance (Q factor ~10-20) and the molecular absorption, indicating that strong coupling is achieved. In other words, phase I and II are both coupled to the same optical resonance at roughly the same strength. The angular optical dispersion shown in Fig. 7.4e for phase I confirms the anti-crossing due to the Rabi splitting. $\hbar\Omega_R^N$ is found to be as large as ~ 320 meV due the location of $PbI_4(R\text{-}NH_3)_2$ at the maximum field amplitude E (in agreement with the findings in section 5.2). As a consequence $\hbar\Omega_R^N/\hbar\omega$ ~ 0.13 and this should be sufficient to perturb the phase transition which was then investigated. Note that the peak in the cavity transmission spectra at 326 nm is due to the bulk plasmon transparency of silver, which overlaps with higher absorption bands of the perovskite (Fig. 7.4d).

Fig. 7.5 shows the hysteresis loops between phase I and II recorded optically as a function of temperature under different conditions. In order to avoid any variance associated with using different samples, the hysteresis loops were always recorded by preparing samples simultaneously in the absence and presence of strong coupling. The mirrors were isolated from the $PbI_4(R\text{-}NH_3)_2$ by a PMMA layer to avoid any chemical interference. The compound was transferred by stamping a PDMS block on the bottom PMMA layer and then the top half of the cavity consisting of PMMA/Ag mirror deposited

on another PDMS block was gently connected to the first half (details in 7.2.1). In the non-cavity case, the top did not have the second Ag mirror as illustrated in Fig. 7.5a.

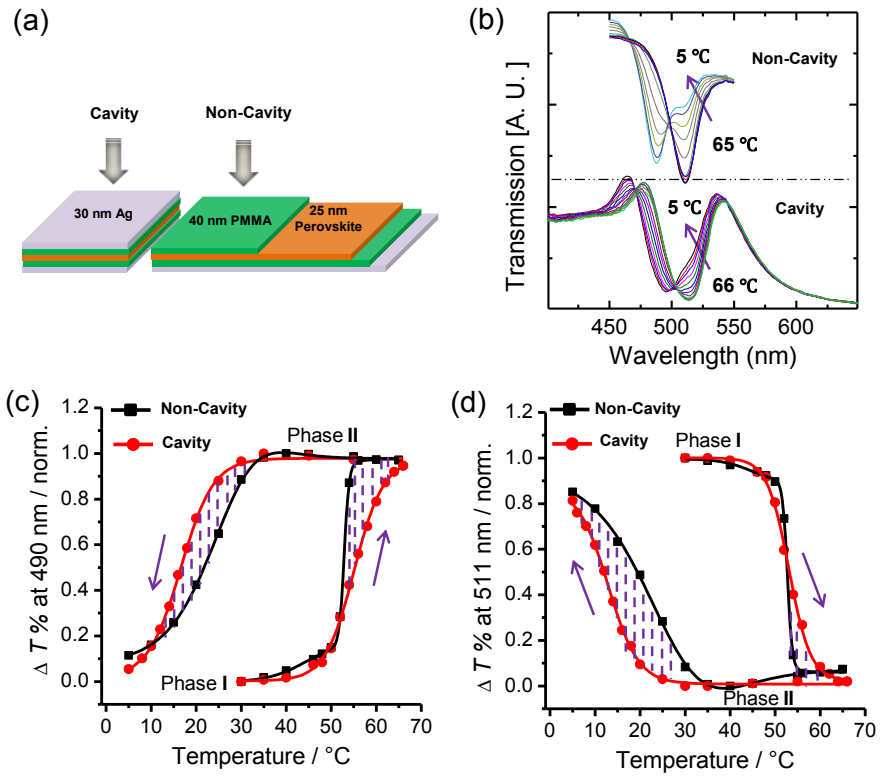

Figure 7.5: (a) The structure of cavity and its reference (non-cavity). Note that the two samples were made simultaneously by the same procedure, the only difference being the presence of the top mirror in the cavity. (b) Examples of the evolution of the transmission spectrum of the cavity and non-cavity as a function of temperature. (c) and (d) Graph of ΔT % (transmission intensity change at 490 nm (c) and 511 nm (d)) versus temperature for $PbI_4(R\text{-}NH_3)_2$ in cavity and non-cavity, the arrows show the direction of the temperature change. The dashed zones mark the enlargement of the hysteresis loop in the coupled system. Figure is from reference.[157]

The change in hysteresis induced by strong coupling can be seen in Figs. 7.5c and d as recorded at 490 nm and 511 nm corresponding respectively to phase I and II. Generally, we have to measure the change of absorbance (ΔA) to estimate the phase I or phase II's concentration evolution as a function of temperature. However, it is difficult to extract the absorbance from the experiment without inducing further errors. For this reason, we used the change of transmission ΔT% normalized by the differential transmission of pure phase I and phase II. The error induced by this approximation is very small because the change in absorbance is less than 0.1. ΔT% change in Fig. 7.5 was

recorded at every point after the temperature was stabilized for 5 min. It is immediately apparent that the hysteresis has broadened by 25% and changed shape. For instance on going from phase II to I the onset temperature moves by 10 °C (from 30 to 20 °C in Fig. 7.5d). Note that we have not observed hysteresis broadening in off-resonance cavity (λ/2 cavity mode at 700 nm). The stabilisation of on-resonance cavity is further confirmed by looking at the time evolution of the hysteresis. The dynamics are significantly slowed as shown in Fig. 7.6 where we compare the kinetics in and out of the cavity. The kinetics are multi-exponential due to the heterogeneity of the $PbI_4(R\text{-}NH_3)_2$ phases, nevertheless it is clear that the phase transition is much slower inside the cavity. The first half-life increases by a factor 3 in the strongly coupled system from Figs. 7.6a and c, for which the phase transition was observed to completion (pure phase II) at 52 °C. We could not observe the end of the kinetics at 30 °C (Figs. 7.6b and d) within reasonable times (2 hours) even though the first half-life was much larger than 3 in the coupled case.

These findings are completely consistent with the lowering of the ground state of the perovskites by strong coupling of its absorption transition to an optical cavity. Here both phases are strongly coupled by the same optical mode however the barrier between them is not coupled since the transient population on the barrier is always negligible. Therefore, only the minima in the potential curves of the phase I and II are lowered as illustrated in Fig. 7.4b and thus the transition barrier increases. A change in barrier height of ~30 meV (2.9 kJ/mole) can be estimated from the ratio in the half-lives upon strong coupling using a simple Arrhenius rate dependence ($1/\tau_{1/2} \approx A\exp(-\Delta E/k_B T)$) and assuming the pre-exponential A-factor to be constant. In other words the ground states of the two perovskite phases are stabilized by this amount. The magnitude of this shift is in agreement with the earlier thermodynamic study[66] and the expectation from second order perturbation theory discussed in Chapter 3.[95]

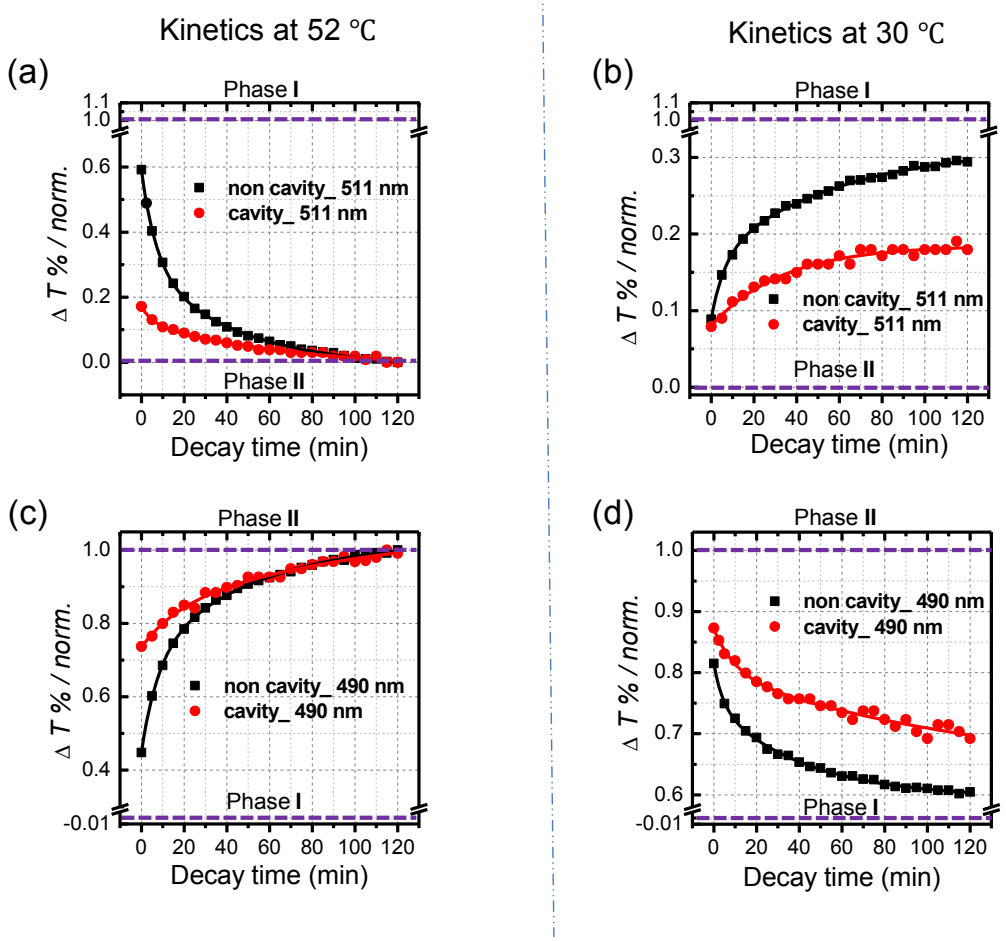

Figure 7.6: Kinetics of the evolution between phase I and II (indicated by violet dashed line) at 52 °C (a) and (c) in the warming cycle and at 30°C (b) and (d) in the cooling cycle, monitored by transmission intensity change at 490 nm for (c) and (d) and at 511 nm for (a) and (b). Figure is from reference.[157]

7.3 Conclusions

Although light-matter strong coupling is associated with splitting excited states, it can also be used to modify the ground state energy landscape such as demonstrated here for the first time in the case of a phase transition. The hysteresis and dynamics of the phase transition of the perovskite $(C_{12}H_{25}NH_3)_2PbI_4$ were significantly modified due to the lowering of the ground states of the two phases by the cavity interaction. Increasing the Rabi splitting will enhance such effects in two ways, first by the direct perturbation of the ground state and secondly by increasing the fraction of coupled oscillators in the cavity.[66] Here the optical resonances were provided by metallic cavities which have the

benefit of having small mode volumes but a variety of other structures are also possible depending on the application, such as propagating[54, 57, 61] and localized surface plasmon resonances[49, 51, 53], and distributed feedback cavities[31]. The possibility of increasing the transition barrier and enlarging the hysteresis loop by strong coupling with the vacuum field demonstrates the potential of using the electromagnetic environment of a material to control its properties.

8 Summary

The whole thesis mainly worked on the optimization of strong coupling strength, understanding fundamental consequences, and application to modifying molecular properties. The main conclusions are given in the context and try to answer the questions raised in **Chapter 2**.

In **Chapter 4** we used a combination of LBL and elastomeric deposition techniques to adsorb a J-aggregate in thin layer directly at the surface of plasmonic arrays to maximize strong coupling. It was shown that hybrid light/matter states with larger Rabi splitting could be achieved when using plasmonic nanostructures of higher symmetry, indicating that SP mode degeneracy is important for efficient coupling. These findings point to new ways for optimizing strong coupling on plasmonic substrates, not only playing on molecular density, but also on photonic mode density, e.g. placing the matter at the "hot-spot" of plasmonic structures as shown in the references.[53, 110] In the last section of this chapter we investigated the strong coupling of a plasmonic dimple arrays with the two transition bands of a cyanine dye by reflection and emission spectroscopy. The two observable emission bands at room temperature are related to the uncoupled molecular and P- polariton bands. The anti-crossing in the dispersion of the polaritonic modes was clear both in reflection and emission.

In **Chapter 5**, the efficiency of light-molecule strong coupling was tuned by precisely varying the spatial position of a thin layer of cyanine dye J-aggregates in FP

micro-cavities. The vacuum Rabi-splitting follows the shape of the field amplitude distribution in the cavities. It tells that the strength of the coupling interaction varies linearly with the vacuum field amplitude defined by the cavity, as expected from the Jaynes-Cummings theory. The measured lifetime of the lowest polaritonic state P- (as long as ps) and the emission quantum yields are mutually consistent. The observation of P- lifetime longer than its constituent states is outside conventional understanding of polariton lifetimes. Moreover, the measured low quantum yield (~ 10^{-2}) demonstrates that the polariton decay is dominated by non-radiative processes in contrast to what might be expected from the small effective mass of the polaritons.

In **Chapter 6**, we showed, through experiments, some of the open questions related to light–matter strong coupling involving molecular materials. It is clear that the line-widths of static absorption spectra associated with P+ and P- represent the coherent lifetime of the strongly coupled system. However in the case of Rabi-splitting much larger than k_BT, the population lifetime of P- is dominated by the dissipation of molecular excited states other than that of cavity mode. Moreover, the direct excitation of P- is low efficient, which raises the question whether the transition selection rules of polaritonic states could be different from the bare molecules. Clearly more experiments and theory that can handle such complex materials and the particularities associated with individual molecular structures need to be developed to elucidate these strongly interacting systems.[164] Only then will the full potential of using a confined electromagnetic environment to control material and molecular properties be realized.

In **Chapter 7**, the phase transition of a perovskite was studied while its absorption transition was strongly coupled to the vacuum field of a micro-cavity. The hysteresis and dynamics of the phase transition were significantly modified due to the lowering of the ground states of the two phases by the cavity interaction. As a consequence, the transition barrier was increased and the hysteresis loop is enlarged, demonstrating the potential of using the electromagnetic environment of a material to control its properties. These findings enrich the energy diagram of strongly coupled system.

More generally, these findings provide a deeper understanding of hybrid light-molecule states and illustrate the implications for the modification of molecular and material properties by strong coupling.

Bibliography

[1] G.R. Fowles, Introduction to modern optics, *Courier Corporation*, **2012**.

[2] J.D. Jackson, Classical electrodynamics, *Wiley New York etc.*, **1962**.

[3] R. Loudon, The quantum theory of light, *Oxford university press*, **2000**.

[4] T. Főrster, 10th Spiers Memorial Lecture. Transfer mechanisms of electronic excitation, *Discuss. Faraday Soc.,* **1959**, *27,* 7-17.

[5] M. Kasha, Energy transfer mechanisms and the molecular exciton model for molecular aggregates, *Radiat. Res.,* **1963**, *20,* 55-70.

[6] S. Haroche, D. Kleppner, Cavity Quantum Electrodynamics, *Phys. Today,* **1989**, *42,* 24-30.

[7] E. Purcell, Spontaneous emission probabilities at radio frequencies, *Springer*, **1995**, 839.

[8] Y. Kaluzny, P. Goy, M. Gross, J.M. Raimond, S. Haroche, Observation of Self-Induced Rabi Oscillations in 2-Level Atoms Excited inside a Resonant Cavity - the Ringing Regime of Super-Radiance, *Phys. Rev. Lett. ,* **1983**, *51,* 1175-1178.

[9] G. Rempe, H. Walther, N. Klein, Observation of quantum collapse and revival in a one-atom maser, *Phys. Rev. Lett. ,* **1987**, *58,* 353-356.

[10] M.G. Raizen, R.J. Thompson, R.J. Brecha, H.J. Kimble, H.J. Carmichael, Normal-Mode Splitting and Linewidth Averaging for 2-State Atoms in an Optical Cavity, *Phys. Rev. Lett. ,* **1989**, *63,* 240-243.

[11] R.J. Thompson, G. Rempe, H.J. Kimble, Observation of normal-mode splitting for an atom in an optical cavity, *Phys. Rev. Lett. ,* **1992**, *68,* 1132-1135.

[12] S. Haroche, Nobel Lecture: Controlling photons in a box and exploring the quantum to classical boundary, *Rev. Mod. Phys.,* **2013**, *85,* 1083-1102.

[13] P. Torma, W.L. Barnes, Strong coupling between surface plasmon polaritons and emitters: a review, *Rep. Prog. Phys.,* **2015**, *78,* 013901.

[14] C. Weisbuch, M. Nishioka, A. Ishikawa, Y. Arakawa, Observation of the Coupled Exciton-Photon Mode Splitting in a Semiconductor Quantum Microcavity, *Phys. Rev. Lett. ,* **1992**, *69,* 3314-3317.

[15] R. Houdre, C. Weisbuch, R.P. Stanley, U. Oesterle, P. Pellandini, M. Ilegems, Measurement of Cavity-Polariton Dispersion Curve from Angle-Resolved Photoluminescence Experiments, *Phys. Rev. Lett. ,* **1994**, *73,* 2043-2046.

[16] R. Houdre, Early stages of continuous wave experiments on cavity-polaritons, *Phys. Stat. Sol. (b),* **2005**, *242,* 2167-2196.

[17] J.J. Baumberg, Spin condensates in semiconductor microcavities, *Springer*, **2002**, 195-219.

[18] M. Saba, C. Ciuti, J. Bloch, V. Thierry-Mieg, R. Andre, L.S. Dang, S. Kundermann, A. Mura, G. Bongiovanni, J.L. Staehli, B. Deveaud, High-temperature ultrafast polariton parametric amplification in semiconductor microcavities, *Nature,* **2001**, *414,* 731-735.

[19] I. Carusotto, C. Ciuti, Quantum fluids of light, *Rev. Mod. Phys.,* **2013**, *85,* 299-366.

[20] W.Y. Liang, Excitons, *Phys. Educ.,* **1970**, *5,* 226.

[21] R.J. Holmes, S.R. Forrest, Strong exciton-photon coupling in organic materials, *Org. Electron.,* **2007**, *8,* 77-93.

[22] G. Khitrova, H.M. Gibbs, M. Kira, S.W. Koch, A. Scherer, Vacuum Rabi splitting in semiconductors, *Nat. Phys. ,* **2006**, *2,* 81-90.

[23] R. Butte, G. Christmann, E. Feltin, J.F. Carlin, M. Mosca, M. Ilegems, N. Grandjean, Room-temperature polariton luminescence from a bulk GaN microcavity, *Phys. Rev. B,* **2006**, *73*.

[24] I.R. Sellers, F. Semond, M. Leroux, J. Massies, A.L. Henneghien, P. Disseix, J. Leymarie, A. Vasson, Strong light-matter coupling in GaN microcavities grown on silicon(111) at room temperature, *Phys. Rev. B,* **2006**, *243,* 1639-1642.

[25] D.E. Gomez, K.C. Vernon, P. Mulvaney, T.J. Davis, Surface Plasmon Mediated Strong Exciton-Photon Coupling in Semiconductor Nanocrystals, *Nano Lett.,* **2010**, *10,* 274-278.

[26] X. Liu, T. Galfsky, Z. Sun, F. Xia, E.-c. Lin, Y.-H. Lee, S. Kéna-Cohen, V.M. Menon, Strong light–matter coupling in two-dimensional atomic crystals, *Nat. Photon.,* **2015**, *9,* 30-34.

[27] J.P. Reithmaier, G. Sek, A. Loffler, C. Hofmann, S. Kuhn, S. Reitzenstein, L.V. Keldysh, V.D. Kulakovskii, T.L. Reinecke, A. Forchel, Strong coupling in a single quantum dot-semiconductor microcavity system, *Nature,* **2004**, *432,* 197-200.

[28] P. Atkins, Physical Chemistry. 6th, in, *Oxford University Press*, **1998**.

[29] I. Pockrand, A. Brillante, D. Mobius, Exciton Surface-Plasmon Coupling - an Experimental Investigation, *J. Chem. Phys.,* **1982**, *77,* 6289-6295.

[30] D.G. Lidzey, D.D.C. Bradley, M.S. Skolnick, T. Virgili, S. Walker, D.M. Whittaker, Strong exciton-photon coupling in an organic semiconductor microcavity, *Nature,* **1998**, *395,* 53-55.

[31] T. Fujita, Y. Sato, T. Kuitani, T. Ishihara, Tunable polariton absorption of distributed feedback microcavities at room temperature, *Phys. Rev. B,* **1998**, *57,* 12428-12434.

[32] P.A. Hobson, W.L. Barnes, D.G. Lidzey, G.A. Gehring, D.M. Whittaker, M.S. Skolnick, S. Walker, Strong exciton-photon coupling in a low-Q all-metal mirror microcavity, *Appl. Phys. Lett.,* **2002**, *81,* 3519-3521.

[33] J.R. Tischler, M.S. Bradley, Q. Zhang, T. Atay, A. Nurmikko, V. Bulovic, Solid state cavity QED: Strong coupling in organic thin films, *Org. Electron.,* **2007**, *8,* 94-113.

[34] P. Vasa, C. Lienau, An Unusual Marriage: Coupling Molecular Excitons to Surface Plasmon Polaritons in Metal Nanostructures, *Angew. Chem. Int. Ed.,* **2010**, *49,* 2476-2477.

[35] A.F.I. Morral, F. Stellacci, Light-matter interactions: Ultrastrong routes to new chemistry, *Nat. Mater.,* **2012**, *11,* 272-273.

[36] P. Lagoudakis, Polariton condensates: Going soft, *Nat. Mater.,* **2014**, *13,* 227-228.

[37] R.J. Holmes, Organic polaritons: Long-distance relationships, *Nat. Mater. ,* **2014**, *13,* 669-670.

[38] P. Michetti, L. Mazza, G.C. La Rocca, Strongly Coupled Organic Microcavities, *Springer*, **2015**, 39-68.

[39] J.P. Lemaistre, Disorder-induced exciton scattering in molecular aggregates, *J. Lumin.,* **1999**, *83-4,* 229-233.

[40] D.G. Lidzey, D.D.C. Bradley, T. Virgili, A. Armitage, M.S. Skolnick, S. Walker, Room temperature polariton emission from strongly coupled organic semiconductor microcavities, *Phys. Rev. Lett. ,* **1999**, *82,* 3316-3319.

[41] A.I. Tartakovskii, M. Emam-Ismail, D.G. Lidzey, M.S. Skolnick, D.D.C. Bradley, S. Walker, V.M. Agranovich, Raman scattering in strongly coupled organic semiconductor microcavities, *Phys. Rev. B,* **2001**, *63,* 121302(R).

[42] V.M. Agranovich, M. Litinskaia, D.G. Lidzey, Cavity polaritons in microcavities containing disordered organic semiconductors, *Phys. Rev. B,* **2003**, *67,* 085311.

[43] R. Gehlhaar, R. Schuppel, M. Koschorreck, T. Fritz, H. Frob, M. Hoffmann, V.G. Lyssenko, K. Leo, L. Connolly, J. Wenus, D.G. Lidzey, Time-resolved and cw photoluminescence from strongly coupled organic microcavities, *J. Lumin.,* **2004**, *110,* 354-358.

[44] P. Schouwink, H.V. Berlepsch, L. Dahne, R.F. Mahrt, Observation of strong exciton-photon coupling in an organic microcavity, *Chem. Phys. Lett.,* **2001**, *344,* 352-356.

[45] P. Schouwink, H. von Berlepsch, L. Dahne, R.F. Mahrt, Observation of strong exciton-photon coupling in an organic microcavity in transmission and photoluminescence, *J. Lumin.,* **2001**, *94,* 821-826.

[46] P. Schouwink, H. von Berlepsch, L. Dahne, R.F. Mahrt, Dependence of Rabi-splitting on the spatial position of the optically active layer in organic microcavities in the strong coupling regime, *Chem. Phys.,* **2002**, *285,* 113-120.

[47] J. Bellessa, C. Bonnand, J.C. Plenet, J. Mugnier, Strong coupling between surface plasmons and excitons in an organic semiconductor, *Phys. Rev. Lett. ,* **2004**, *93,* 036404.

[48] S.A. Guebrou, C. Symonds, E. Homeyer, J.C. Plenet, Y.N. Gartstein, V.M. Agranovich, J. Bellessa, Coherent Emission from a Disordered Organic Semiconductor Induced by Strong Coupling with Surface Plasmons, *Phys. Rev. Lett. ,* **2012**, *108,* 066401.

[49] W.H. Ni, Z. Yang, H.J. Chen, L. Li, J.F. Wang, Coupling between molecular and plasmonic resonances in freestanding dye-gold nanorod hybrid nanostructures, *J. Am. Chem. Soc.,* **2008**, *130,* 6692.

[50] N.T. Fofang, N.K. Grady, Z.Y. Fan, A.O. Govorov, N.J. Halas, Plexciton Dynamics: Exciton-Plasmon Coupling in a J-Aggregate-Au Nanoshell Complex Provides a Mechanism for Nonllinearity, *Nano Lett.,* **2011**, *11,* 1556-1560.

[51] Y.W. Hao, H.Y. Wang, Y. Jiang, Q.D. Chen, K. Ueno, W.Q. Wang, H. Misawa, H.B. Sun, Hybrid-State Dynamics of Gold Nanorods/Dye J-Aggregates under Strong Coupling, *Angew. Chem. Int. Ed.,* **2011**, *50,* 7824-7828.

[52] G. Zengin, G. Johansson, P. Johansson, T.J. Antosiewicz, M. Kall, T. Shegai, Approaching the strong coupling limit in single plasmonic nanorods interacting with J-aggregates, *Sci. Rep.,* **2013**, *3*.

[53] G. Zengin, M. Wersäll, S. Nilsson, T.J. Antosiewicz, M. Käll, T. Shegai, Realizing Strong Light-Matter Interactions between Single-Nanoparticle Plasmons and Molecular Excitons at Ambient Conditions, *Phys. Rev. Lett. ,* **2015**, *114,* 157401.

[54] P. Vasa, R. Pomraenke, G. Cirmi, E. De Re, W. Wang, S. Schwieger, D. Leipold, E. Runge, G. Cerullo, C. Lienau, Ultrafast Manipulation of Strong Coupling in Metal-Molecular Aggregate Hybrid Nanostructures, *Acs Nano,* **2010**, *4,* 7559-7565.

[55] P. Vasa, W. Wang, R. Pomraenke, M. Lammers, M. Maiuri, C. Manzoni, G. Cerullo, C. Lienau, Real-time observation of ultrafast Rabi oscillations between excitons and plasmons in metal nanostructures with J-aggregates, *Nat. Photonics,* **2013**, *7,* 128-132.

[56] W. Wang, P. Vasa, R. Pomraenke, R. Vogelgesang, A. De Sio, E. Sommer, M. Maiuri, C. Manzoni, G. Cerullo, C. Lienau, Interplay between Strong Coupling and Radiative Damping of Excitons and Surface Plasmon Polaritons in Hybrid Nanostructures, *Acs Nano,* **2014**, *8,* 1056-1064.

[57] J. Dintinger, S. Klein, F. Bustos, W.L. Barnes, T.W. Ebbesen, Strong coupling between surface plasmon-polaritons and organic molecules in subwavelength hole arrays, *Phys. Rev. B,* **2005**, *71,* 035424.

[58] A. Salomon, S.J. Wang, J.A. Hutchison, C. Genet, T.W. Ebbesen, Strong Light-Molecule Coupling on Plasmonic Arrays of Different Symmetry, *Chemphyschem,* **2013**, *14,* 1882-1886.

[59] T. Schwartz, J.A. Hutchison, J. Leonard, C. Genet, S. Haacke, T.W. Ebbesen, Polariton Dynamics under Strong Light-Molecule Coupling, *Chemphyschem,* **2013**, *14,* 125-131.

[60] S. Wang, T. Chervy, J. George, J.A. Hutchison, C. Genet, T.W. Ebbesen, Quantum Yield of Polariton Emission from Hybrid Light-Matter States, *J. Phys. Chem. Lett.,* **2014**, *5,* 1433-1439.

[61] T.K. Hakala, J.J. Toppari, A. Kuzyk, M. Pettersson, H. Tikkanen, H. Kunttu, P. Torma, Vacuum Rabi Splitting and Strong-Coupling Dynamics for Surface-Plasmon Polaritons and Rhodamine 6G Molecules, *Phys. Rev. Lett. ,* **2009**, *103,* 053602.

[62] L. Shi, T.K. Hakala, H.T. Rekola, J.P. Martikainen, R.J. Moerland, P. Torma, Spatial Coherence Properties of Organic Molecules Coupled to Plasmonic Surface Lattice

Resonances in the Weak and Strong Coupling Regimes, *Phys. Rev. Lett. ,* **2014**, *112,* 153002.

[63] S. Kena-Cohen, S.A. Maier, D.D.C. Bradley, Ultrastrongly Coupled Exciton-Polaritons in Metal-Clad Organic Semiconductor Microcavities, *Adv. Opt. Mater.,* **2013**, *1,* 827-833.

[64] J. George, S. Wang, T. Chervy, A. Canaguier-Durand, G. Schaeffer, J.M. Lehn, J.A. Hutchison, C. Genet, T.W. Ebbesen, Ultra-strong coupling of molecular materials: spectroscopy and dynamics, *Faraday Discuss. ,* **2015**, *178,* 281-294.

[65] D.M. Coles, Y.S. Yang, Y.Y. Wang, R.T. Grant, R.A. Taylor, S.K. Saikin, A. Aspuru-Guzik, D.G. Lidzey, J.K.H. Tang, J.M. Smith, Strong coupling between chlorosomes of photosynthetic bacteria and a confined optical cavity mode, *Nat. Commun.,* **2014**, *5*.

[66] A. Canaguier-Durand, E. Devaux, J. George, Y.T. Pang, J.A. Hutchison, T. Schwartz, C. Genet, N. Wilhelms, J.M. Lehn, T.W. Ebbesen, Thermodynamics of Molecules Strongly Coupled to the Vacuum Field, *Angew. Chem. Int. Ed.,* **2013**, *52,* 10533-10536.

[67] K.S. Daskalakis, S.A. Maier, R. Murray, S. Kena-Cohen, Nonlinear interactions in an organic polariton condensate, *Nat. Mater.,* **2014**, *13,* 272-279.

[68] S. Kena-Cohen, S.R. Forrest, Room-temperature polariton lasing in an organic single-crystal microcavity, *Nat. Photonics,* **2010**, *4,* 371-375.

[69] J.D. Plumhof, T. Stoferle, L.J. Mai, U. Scherf, R.F. Mahrt, Room-temperature Bose-Einstein condensation of cavity exciton-polaritons in a polymer, *Nat. Mater.,* **2014**, *13,* 248-253.

[70] C.R. Gubbin, S.A. Maier, S. Kena-Cohen, Low-voltage polariton electroluminescence from an ultrastrongly coupled organic light-emitting diode, *Appl. Phys. Lett.,* **2014**, *104,* 233302.

[71] T. Schwartz, J.A. Hutchison, C. Genet, T.W. Ebbesen, Reversible Switching of Ultrastrong Light-Molecule Coupling, *Phys. Rev. Lett. ,* **2011**, *106,* 196405.

[72] J.A. Hutchison, A. Liscio, T. Schwartz, A. Canaguier-Durand, C. Genet, V. Palermo, P. Samori, T.W. Ebbesen, Tuning the Work-Function Via Strong Coupling, *Adv. Mater. ,* **2013**, *25,* 2481-2485.

[73] E. Orgiu, J. George, J. Hutchison, E. Devaux, J.-F. Dayen, B. Doudin, F. Stellacci, C. Genet, P. Samori, T. Ebbesen, Conductivity in organic semiconductors mediated by polaritonic states, *arXiv preprint arXiv:1409.1900,* **2014**.

[74] A. Shalabney, J. George, H. Hiura, J.A. Hutchison, C. Genet, P. Hellwig, T.W. Ebbesen, Enhanced Raman Scattering from Vibro-Polariton Hybrid States, *Angew. Chem. Int. Ed.,* **2015**.

[75] A.I. Vakevainen, R.J. Moerland, H.T. Rekola, A.P. Eskelinen, J.P. Martikainen, D.H. Kim, P. Torma, Plasmonic Surface Lattice Resonances at the Strong Coupling Regime, *Nano Lett.,* **2014**, *14,* 1721-1727.

[76] C. Symonds, G. Lheureux, J.P. Hugonin, J.J. Greffet, J. Laverdant, G. Brucoli, A. Lemaitre, P. Senellart, J. Bellessa, Confined Tamm Plasmon Lasers, *Nano Lett.,* **2013**, *13,* 3179-3184.

[77] A. Canaguier-Durand, C. Genet, A. Lambrecht, T.W. Ebbesen, S. Reynaud, Non-Markovian polariton dynamics in organic strong coupling, *Eur. Phys. J. D,* **2015**, *69,* 24.

[78] J.H. Song, Y. He, A.V. Nurmikko, J. Tischler, V. Bulovic, Exciton-polariton dynamics in a transparent organic semiconductor microcavity, *Phys. Rev. B,* **2004**, *69,* 235330.

[79] G.P. Wiederrecht, J.E. Hall, A. Bouhelier, Control of molecular energy redistribution pathways via surface plasmon gating, *Phys. Rev. Lett. ,* **2007**, *98,* 083001.

[80] A. Salomon, C. Genet, T.W. Ebbesen, Molecule-Light Complex: Dynamics of Hybrid Molecule-Surface Plasmon States, *Angew. Chem. Int. Ed.,* **2009**, *48,* 8748-8751.

[81] D.E. Gómez, S.S. Lo, T.J. Davis, G.V. Hartland, Picosecond Kinetics of Strongly Coupled Excitons and Surface Plasmon Polaritons, *J. Phys. Chem. B* **2013**, *117,* 4340-4346.

[82] D.M. Coles, N. Somaschi, P. Michetti, C. Clark, P.G. Lagoudakis, P.G. Savvidis, D.G. Lidzey, Polariton-mediated energy transfer between organic dyes in a strongly coupled optical microcavity, *Nat. Mater.,* **2014**, *13,* 712-719.

[83] J.R. Tischler, M.S. Bradley, V. Bulovic, J.H. Song, A. Nurmikko, Strong coupling in a microcavity LED, *Phys. Rev. Lett. ,* **2005**, *95,* 036401.

[84] J.A. Hutchison, T. Schwartz, C. Genet, E. Devaux, T.W. Ebbesen, Modifying Chemical Landscapes by Coupling to Vacuum Fields, *Angew. Chem. Int. Ed.,* **2012**, *51,* 1592-1596.

[85] A. Shalabney, J. George, J. Hutchison, G. Pupillo, C. Genet, T.W. Ebbesen, Coherent coupling of molecular resonators with a microcavity mode, *Nat.Commun.,* **2015**, *6,* 5981.

[86] J. George, A. Shalabney, J.A. Hutchison, C. Genet, T.W. Ebbesen, Liquid-Phase Vibrational Strong Coupling, *J. Phys. Chem. Lett.,* **2015**, *6,* 1027-1031.

[87] Y.F. Zhu, D.J. Gauthier, S.E. Morin, Q.L. Wu, H.J. Carmichael, T.W. Mossberg, Vacuum Rabi Splitting as a Feature of Linear-Dispersion Theory - Analysis and Experimental-Observations, *Phys. Rev. Lett. ,* **1990**, *64,* 2499-2502.

[88] K. Oughstun, N. Cartwright, On the Lorentz-Lorenz formula and the Lorentz model of dielectric dispersion, *Opt. Express,* **2003**, *11,* 1541-1546.

[89] J.J. Greffet, R. Carminati, K. Joulain, J.P. Mulet, S.P. Mainguy, Y. Chen, Coherent emission of light by thermal sources, *Nature,* **2002**, *416,* 61-64.

[90] F. Marquier, K. Joulain, J.P. Mulet, R. Carminati, J.J. Greffet, Y. Chen, Coherent spontaneous emission of light by thermal sources, *Phys. Rev. B,* **2004**, *69,* 155412.

[91] M.J. Gentile, S. Núñez-Sánchez, W.L. Barnes, Optical Field-Enhancement and Subwavelength Field-Confinement Using Excitonic Nanostructures, *Nano Lett.,* **2014**, *14,* 2339-2344.

[92] J.-M. Raimond, S. Haroche, Exploring the quantum, *Oxford University Press*, **2006**.

[93] E.T. Jaynes, F.W. Cummings, Comparison of quantum and semiclassical radiation theories with application to the beam maser, *Proc. IEEE,* **1963**, *51,* 89-109.

[94] K.J. Vahala, Optical microcavities, *Nature,* **2003**, *424,* 839-846.

[95] C. Ciuti, G. Bastard, I. Carusotto, Quantum vacuum properties of the intersubband cavity polariton field, *Phys. Rev. B,* **2005**, *72,* 115303.

[96] R.H. Dicke, Coherence in Spontaneous Radiation Processes, *Phys. Rev.,* **1954**, *93,* 99-110.

[97] M. Tavis, F.W. Cummings, Exact Solution for an *N*-Molecule-Radiation Field Hamiltonian, *Phys. Rev.,* **1968**, *170,* 379-384.

[98] B.M. Garraway, The Dicke model in quantum optics: Dicke model revisited, *Phil. Trans. R. Soc. A* **2011**, *369,* 1137-1155.

[99] W.L. Barnes, A. Dereux, T.W. Ebbesen, Surface plasmon subwavelength optics, *Nature,* **2003**, *424,* 824-830.

[100] T.W. Ebbesen, C. Genet, S.I. Bozhevolnyi, Surface-plasmon circuitry, *Phys. Today,* **2008**, *61,* 44.

[101] H. Raether, Surface plasmons on smooth surfaces, *Springer*, **1988**.

[102] S. Babar, J.H. Weaver, Optical constants of Cu, Ag, and Au revisited, *Appl. Opt.,* **2015**, *54,* 477-481.

[103] A. Otto, Excitation of nonradiative surface plasma waves in silver by the method of frustrated total reflection, *Z. Physik,* **1968**, *216,* 398-410.

[104] E. Kretschmann, H. Raether, Radiative decay of non-radiative surface plasmons excited by light, *Z. Naturforsch. a,* **1968**, *23,* 2135-2136.

[105] H.J. Simon, J.K. Guha, Directional surface plasmon scattering from silver films, *Opt. Commun.,* **1976**, *18,* 391-394.

[106] B. Stein, J.-Y. Laluet, E. Devaux, C. Genet, T.W. Ebbesen, Surface Plasmon Mode Steering and Negative Refraction, *Phys. Rev. Lett. ,* **2010**, *105,* 266804.

[107] C. Genet, T.W. Ebbesen, Light in tiny holes, *Nature,* **2007**, *445,* 39-46.

[108] J.Y. Laluet, A. Drezet, C. Genet, T.W. Ebbesen, Generation of surface plasmons at single subwavelength slits: from slit to ridge plasmon, *New J. Phys.,* **2008**, *10,* 105014.

[109] J.M. Yi, A. Cuche, F. de León-Pérez, A. Degiron, E. Laux, E. Devaux, C. Genet, J. Alegret, L. Martín-Moreno, T.W. Ebbesen, Diffraction Regimes of Single Holes, *Phys. Rev. Lett. ,* **2012**, *109,* 023901.

[110] S.J.P. Kress, P. Richner, S.V. Jayanti, P. Galliker, D.K. Kim, D. Poulikakos, D.J. Norris, Near-Field Light Design with Colloidal Quantum Dots for Photonics and Plasmonics, *Nano Lett.,* **2014**, *14,* 5827-5833.

[111] R.H. Ritchie, E.T. Arakawa, J.J. Cowan, R.N. Hamm, Surface-Plasmon Resonance Effect in Grating Diffraction, *Phys. Rev. Lett. ,* **1968**, *21,* 1530-1533.

[112] T.W. Ebbesen, H.J. Lezec, H.F. Ghaemi, T. Thio, P.A. Wolff, Extraordinary optical transmission through sub-wavelength hole arrays, *Nature,* **1998**, *391,* 667-669.

[113] C. Genet, M.P. van Exter, J.P. Woerdman, Fano-type interpretation of red shifts and red tails in hole array transmission spectra, *Opt. Commun.,* **2003**, *225,* 331-336.

[114] RadisavljevicB, RadenovicA, BrivioJ, GiacomettiV, KisA, Single-layer MoS2 transistors, *Nat. Nano,* **2011**, *6,* 147-150.

[115] N.C. Lindquist, P. Nagpal, K.M. McPeak, D.J. Norris, S.H. Oh, Engineering metallic nanostructures for plasmonics and nanophotonics, *Rep. Prog. Phys.,* **2012**, *75*.

[116] A. Krishnan, T. Thio, T.J. Kim, H.J. Lezec, T.W. Ebbesen, P.A. Wolff, J. Pendry, L. Martin-Moreno, F.J. Garcia-Vidal, Evanescently coupled resonance in surface plasmon enhanced transmission, *Opt. Commun.,* **2001**, *200,* 1-7.

[117] H.J. Lezec, A. Degiron, E. Devaux, R.A. Linke, L. Martin-Moreno, F.J. Garcia-Vidal, T.W. Ebbesen, Beaming Light from a Subwavelength Aperture, *Science,* **2002**, *297,* 820-822.

[118] O. Mahboub, S.C. Palacios, C. Genet, F.J. Garcia-Vidal, S.G. Rodrigo, L. Martin-Moreno, T.W. Ebbesen, Optimization of bull's eye structures for transmission enhancement, *Opt. Express* **2010**, *18,* 11292-11299.

[119] J.-M. Yi, A. Cuche, E. Devaux, C. Genet, T.W. Ebbesen, Beaming Visible Light with a Plasmonic Aperture Antenna, *Acs Photonics,* **2014**, *1,* 365-370.

[120] O. Mahboub, S.C. Palacios, C. Genet, F.J. Garcia-Vidal, S.G. Rodrigo, L. Martin-Moreno, T.W. Ebbesen, Optimization of bulls' eye structures for transmission enhancement, *Opt. Express,* **2010**, *18,* 11292-11299.

[121] S. Carretero-Palacios, O. Mahboub, F.J. Garcia-Vidal, L. Martin-Moreno, S.G. Rodrigo, C. Genet, T.W. Ebbesen, Mechanisms for extraordinary optical transmission through bull's eye structures, *Opt. Express,* **2011**, *19,* 10429-10442.

[122] F.J. García-Vidal, H.J. Lezec, T.W. Ebbesen, L. Martín-Moreno, Multiple Paths to Enhance Optical Transmission through a Single Subwavelength Slit, *Phys. Rev. Lett. ,* **2003**, *90,* 213901.

[123] A.D. Schwab, D.E. Smith, C.S. Rich, E.R. Young, W.F. Smith, J.C. de Paula, Porphyrin nanorods, *J Phys Chem B,* **2003**, *107,* 11339-11345.

[124] G. Decher, Fuzzy Nanoassemblies: Toward Layered Polymeric Multicomposites, *Science,* **1997**, *277,* 1232-1237.

[125] P.G. Van Patten, A.P. Shreve, R.J. Donohoe, Structural and photophysical properties of a water-soluble porphyrin associated with polycations in solution and electrostatically-assembled ultrathin films, *J. Phys. Chem. B,* **2000**, *104,* 5986-5992.

[126] K. Ariga, Y. Lvov, T. Kunitake, Assembling alternate dye-polyion molecular films by electrostatic layer-by-layer adsorption, *J. Am. Chem. Soc.,* **1997**, *119,* 2224-2231.

[127] A. Salomon, R.J. Gordon, Y. Prior, T. Seideman, M. Sukharev, Strong Coupling between Molecular Excited States and Surface Plasmon Modes of a Slit Array in a Thin Metal Film, *Phys. Rev. Lett. ,* **2012**, *109,* 073002.

[128] J.A. Hutchison, D.M. O'Carroll, T. Schwartz, C. Genet, T.W. Ebbesen, Absorption-induced transparency, *Angew. Chem. Int. Ed.,* **2011**, *50,* 2085-2089.

[129] E. Laux, C. Genet, T.W. Ebbesen, Enhanced optical transmission at the cutoff transition, *Opt. Express,* **2009**, *17,* 6920-6930.

[130] R.B. Mujumdar, L.A. Ernst, S.R. Mujumdar, C.J. Lewis, A.S. Waggoner, Cyanine dye labeling reagents: Sulfoindocyanine succinimidyl esters, *Bioconjugate Chem.,* **1993**, *4,* 105-111.

[131] M.S. Bradley, J.R. Tischler, V. Bulovic, Layer-by-layer J-aggregate thin films with a peak absorption constant of 10(6) cm(-1), *Adv. Mater. ,* **2005**, *17,* 2147-2147.

[132] D.M. Coles, R.T. Grant, D.G. Lidzey, C. Clark, P.G. Lagoudakis, Imaging the polariton relaxation bottleneck in strongly coupled organic semiconductor microcavities, *Phys. Rev. B,* **2013**, *88,* 121303(R).

[133] T. Schwartz, J.A. Hutchison, J. Leonard, C. Genet, S. Haacke, T.W. Ebbesen, Polariton dynamics under strong light-molecule coupling, *Chemphyschem,* **2013**, *14,* 125-131.

[134] C. Wurth, M. Grabolle, J. Pauli, M. Spieles, U. Resch-Genger, Relative and absolute determination of fluorescence quantum yields of transparent samples, *Nat. Protoc.,* **2013**, *8,* 1535-1550.

[135] A.A. Muenter, D.V. Brumbaugh, J. Apolito, L.A. Horn, F.C. Spano, S. Mukamel, Size Dependence of Excited-State Dynamics for J-Aggregates at Agbr Interfaces, *J. Phys. Chem.,* **1992**, *96,* 2783-2790.

[136] P.J. Reid, D.A. Higgins, P.F. Barbara, Environment-dependent photophysics of polymer-bound J aggregates determined by time-resolved fluorescence spectroscopy and time-resolved near-field scanning optical microscopy, *J. Phys. Chem. ,* **1996**, *100,* 3892-3899.

[137] T. Virgili, D. Coles, A.M. Adawi, C. Clark, P. Michetti, S.K. Rajendran, D. Brida, D. Polli, G. Cerullo, D.G. Lidzey, Ultrafast polariton relaxation dynamics in an organic semiconductor microcavity, *Phys. Rev. B,* **2011**, *83,* 245309.

[138] G. v. Bünau, Photophysics of Aromatic Molecules, *Wiley-VCH*, **1970**.

[139] S.J. Strickler, R.A. Berg, Relationship between Absorption Intensity and Fluorescence Lifetime of Molecules, *J. Chem. Phys.,* **1962**, *37,* 814-822.

[140] S. Makio, N. Kanamaru, J. Tanaka, The J-Aggregate 5,5',6,6'-Tetrachloro-1,1'-Diethyl-3,3'-Bis(4-Sulfobutylbenzimidazolocarbocyanine Sodium-Salt in Aqueous-Solution, *Bull. Chem. Soc. Jpn. ,* **1980**, *53,* 3120-3124.

[141] G. Andric, J.F. Boas, A.M. Bond, G.D. Fallon, K.P. Ghiggino, C.F. Hogan, J.A. Hutchison, M.A.P. Lee, S.J. Langford, J.R. Pilbrow, G.J. Troup, C.P. Woodward, Spectroscopy of naphthalene diimides and their anion radicals, *Aust. J. Chem.,* **2004**, *57,* 1011-1019.

[142] R. Berera, R. van Grondelle, J.T.M. Kennis, Ultrafast transient absorption spectroscopy: principles and application to photosynthetic systems, *Photosynth Res,* **2009**, *101,* 105-118.

[143] M.A. Koponen, U. Hohenester, T.K. Hakala, J.J. Toppari, Absence of mutual polariton scattering for strongly coupled surface plasmon polaritons and dye molecules with a large Stokes shift, *Phys. Rev. B,* **2013**, *88,* 085425.

[144] R. Houdre, R.P. Stanley, M. Ilegems, Vacuum-field Rabi splitting in the presence of inhomogeneous broadening: Resolution of a homogeneous linewidth in an inhomogeneously broadened system, *Phys. Rev. A,* **1996**, *53,* 2711-2715.

[145] P. Michetti, G.C. La Rocca, Polariton states in disordered organic microcavities, *Phys. Rev. B,* **2005**, *71,* 115320.

[146] P. Forn-Díaz, J. Lisenfeld, D. Marcos, J.J. García-Ripoll, E. Solano, C.J.P.M. Harmans, J.E. Mooij, Observation of the Bloch-Siegert Shift in a Qubit-Oscillator System in the Ultrastrong Coupling Regime, *Phys. Rev. Lett. ,* **2010**, *105,* 237001.

[147] T.L. Hill, Statistical Mechanics of Adsorption. V. Thermodynamics and Heat of Adsorption, *J. Chem. Phys.,* **1949**, *17,* 520-535.

[148] D.R. Knittel, S.P. Pack, S.H. Lin, L. Eyring, Thermodynamic Model of Hysteresis in Phase-Transitions and Its Application to Rare-Earth Oxide Systems, *J. Chem. Phys.,* **1977**, *67,* 134-142.

[149] A. Suzuki, T. Tanaka, Phase-Transition in Polymer Gels Induced by Visible-Light, *Nature,* **1990**, *346,* 345-347.

[150] O. Kahn, C.J. Martinez, Spin-transition polymers: From molecular materials toward memory devices, *Science,* **1998**, *279,* 44-48.

[151] R. Lopez, L.A. Boatner, T.E. Haynes, R.F. Haglund, L.C. Feldman, Enhanced hysteresis in the semiconductor-to-metal phase transition of VO2 precipitates formed in SiO2 by ion implantation, *Appl. Phys. Lett.,* **2001**, *79,* 3161-3163.

[152] O. Sato, J. Tao, Y.Z. Zhang, Control of magnetic properties through external stimuli, *Angew. Chem. Int. Ed.,* **2007**, *46,* 2152-2187.

[153] T. Driscoll, H.T. Kim, B.G. Chae, M. Di Ventra, D.N. Basov, Phase-transition driven memristive system, *Appl. Phys. Lett.,* **2009**, *95,* 043503.

[154] T. Mahfoud, G. Molnar, S. Bonhommeau, S. Cobo, L. Salmon, P. Demont, H. Tokoro, S.I. Ohkoshi, K. Boukheddaden, A. Bousseksou, Electric-Field-Induced Charge-Transfer Phase Transition: A Promising Approach Toward Electrically Switchable Devices, *J. Am. Chem. Soc.,* **2009**, *131,* 15049-15054.

[155] S. Ohkoshi, Y. Tsunobuchi, T. Matsuda, K. Hashimoto, A. Namai, F. Hakoe, H. Tokoro, Synthesis of a metal oxide with a room-temperature photoreversible phase transition, *Nat. Chem.,* **2010**, *2,* 539-545.

[156] F. Kagawa, S. Horiuchi, N. Minami, S. Ishibashi, K. Kobayashi, R. Kumai, Y. Murakami, Y. Tokura, Polarization Switching Ability Dependent on Multidomain Topology in a Uniaxial Organic Ferroelectric, *Nano Lett.,* **2014**, *14,* 239-243.

[157] S.J. Wang, A. Mika, J.A. Hutchison, C. Genet, A. Jouaiti, M.W. Hosseini, T.W. Ebbesen, Phase transition of a perovskite strongly coupled to the vacuum field, *Nanoscale,* **2014**, *6,* 7243-7248.

[158] D.B. Mitzi, Synthesis, structure, and properties of organic-inorganic perovskites and related materials, *Prog. Inorg. Chem. ,* **1999**, *48,* 1-121.

[159] J.L. Knutson, J.D. Martin, D.B. Mitzi, Tuning the band gap in hybrid tin iodide perovskite semiconductors using structural templating, *Inorg. Chem.,* **2005**, *44,* 4699-4705.

[160] D.G. Billing, A. Lemmerer, Synthesis, characterization and phase transitions of the inorganic-organic layered perovskite-type hybrids [(CnH2n+1NH3)(2)PbI4] (n=12, 14, 16 and 18), *New J. Chem.,* **2008**, *32,* 1736-1746.

[161] K. Pradeesh, J.J. Baumberg, G.V. Prakash, Exciton switching and Peierls transitions in hybrid inorganic-organic self-assembled quantum wells, *Appl. Phys. Lett.,* **2009**, *95,* 173305.

[162] G. Lanty, A. Brehier, R. Parashkov, J.S. Lauret, E. Deleporte, Strong exciton-photon coupling at room temperature in microcavities containing two-dimensional layered perovskite compounds, *New J. Phys.,* **2008**, *10,* 065007.

[163] K. Pradeesh, J.J. Baumberg, G.V. Prakash, Strong exciton-photon coupling in inorganic-organic multiple quantum wells embedded low-Q microcavity, *Opt. Express,* **2009**, *17,* 22171-22178.

[164] J. Galego, F.J. Garcia-Vidal, J. Feist, Cavity-induced modifications of molecular structure in the strong coupling regime, *arXiv preprint arXiv:1506.03331,* **2015**.

Publications

Work covered in this thesis

A. Salomon, **S.Wang**, J.A. Hutchison, C. Genet, T.W. Ebbesen, Strong Light-Molecule Coupling on Plasmonic Arrays of Different Symmetry, *Chemphyschem,* **2013**, *14,* 1882-1886.

S. Wang, T. Chervy, J. George, J.A. Hutchison, C. Genet, T.W. Ebbesen, Quantum Yield of Polariton Emission from Hybrid Light-Matter States, *J. Phys. Chem. Lett.,* **2014**, *5,* 1433-1439.

S. Wang, A. Mika, J.A. Hutchison, C. Genet, A. Jouaiti, M.W. Hosseini, T.W. Ebbesen, Phase transition of a perovskite strongly coupled to the vacuum field, *Nanoscale,* **2014**, *6,* 7243-7248.

J. George, **S. Wang**, T. Chervy, A. Canaguier-Durand, G. Schaeffer, J.M. Lehn, J.A. Hutchison, C. Genet, T.W. Ebbesen, Ultra-strong coupling of molecular materials: spectroscopy and dynamics, *Faraday Discuss. ,* **2015**, *178,* 281-294.

Conference presentations

Wang, S.; Hutchison, J. A.; Genet, C. and Ebbesen, T. W.; a *poster* "Strong Coupling between Degenerate Surface Plasmon Modes and J-aggregate Excitons in Nano-hole Array", presented at OP1-5, **E-MRS 2012 Spring Meeting**, Strasbourg, France, (14/05/**2012**)

Wang, S.; George, J.; Hutchison, J. A.; Genet, C. and Ebbesen, T. W.; a *poster* "Tuning Strong Light-Molecule Coupling and Modification of a Phase Transition", presented at N8.08, **MRS 2013 Fall Meeting**, Boston, USA, (04/12/**2013**)

Wang, S.; Chervy, T.; Hutchison, J. A.; Genet, C. and Ebbesen, T. W.; a *talk* "Strong Light-Molecule Coupling: Routes to New Hybrid Materials ", presented at NR30, **International Conference of Small Science**, Hongkong, China, (10/12/**2014**)

Wang, S.; Chervy, T.; George, J.; Hutchison, J. A.; Genet, C. and Ebbesen, T. W.; a *lightning poster presentation* "Tuning Strong Light-Molecule Coupling and Modification of a Phase Transition", presented at **Faraday Discussions on Nanoplasmonics**, London, UK, (16/02/**2015**)